FABRICATION, PERFORMANCE AND PROCESS OPTIMIZATION OF SOLID ELECTROLYTE CELLS FOR ELECTROCHEMICAL REFINING OF COPPER

by

SHI YUAN

B.S., Zhejiang University
Hangzhou, P.R.China
1990

Submitted to the Department of Materials Science and Engineering
in Partial Fulfillment of the Requirements for the
Degree of

DOCTOR OF PHILOSOPHY

at the

Massachusetts Institute of technology

June 1995

Signature of Author...
Department of Materials Science and Engineering
May 5, 1995

Certified by...
Professor Uday B. Pal
Thesis Supervisor

Accepted by...
Carl V. Thompson II
Professor of Electronic Materials
Chair, Departmental Committee on Graduate Students

1a

FABRICATION, PERFORMANCE AND PROCESS OPTIMIZATION OF SOLID ELECTROLYTE CELLS FOR ELECTROCHEMICAL REFINING OF COPPER

by

SHI YUAN

Submitted to the Department of Materials Science and Engineering on May 5, 1995 in partial fulfillment of the requirements for the degree of Doctor of Philosophy

ABSTRACT

Inclusion free deoxidation of copper melts was performed by short-circuiting a solid electrolyte cell. The solid electrolyte cell consisted of a yttria stabilized zirconia tube closed at one end. The tube interior was flushed with a reducing gas and the tube was immersed in the copper melt. A layer of porous $Ni-ZrO_2$ cermet deposited on the inner wall of the tube served as the anode while the copper melt as the cathode. The deoxidation experiments were conducted by varying the following experimental parameters: temperature, flow rate of the reducing gas, type of the reducing gas, and stirring intensity in molten copper.

A two-step process was employed to deposit the porous $Ni-ZrO_2$ cermet anode over the yttria-stabilized zirconia tube. The technique consisted of nickel slurry coating, pressure infiltrating zirconia suspension, and sintering. The electrode was characterized by porosity measurement, sheet resistance measurement, and high temperature stability test. It was shown that the infiltration step improved the long term stability of the cermet.

To provide a general understanding of the deoxidation process, each step in the process was analyzed in detail. The transport of oxygen ions in the stabilized zirconia was modeled by taking into account both external load and electronic conductivity. The deoxidation process was modeled as a function of temperature, short circuit resistance, flow rate of the reducing gases, electronic and ionic conductivity of the electrolyte, and mass transfer coefficient of oxygen in the molten copper. The deoxidation model was also solved numerically to provide a more accurate picture of the process.

The deoxidation model was used to discuss process optimization and scale-up. It was shown that the most critical parameters controlling the deoxidation process were mass transfer coefficient of oxygen in molten copper, interfacial area of the electrodes, and the short circuit resistance. A scale-up structure was proposed which would maximize the interfacial area of electrodes and minimize the short circuit resistance.

Thesis Supervisor: Uday B. Pal
Title: John Chipman Assistant Professor of Chemical Processing of Materials

TABLE OF CONTENTS

LIST OF TABLES

LIST OF FIGURES

6

LIST OF TERMS

α:	m/s	mass transfer coefficient
δ:	m	thickness of diffusion boundary layer
η:	J/mol-m	electrochemical potential of electrons in the electrolyte
Φ:	V/m	electrical potential in the electrolyte
$\mu_{O^{2-}}$	J/mol-m	chemical potential of oxygen ions in the electrolyte
μ_e	J/mol-m	chemical potential of electrons in the electrolyte
σ_{ion}:	S/m	ionic conductivity of electrolyte
σ_e^0:	S/m	ionic conductivity of electrolyte
ρ_{melt}:	kg/m^3	density of the copper melt
A:	m^2	effective area of electrode/electrolyte interfacial area
d:	m	thickness of electrolyte
C_i:	ppm	oxygen concentration at the interface between electrolyte and melt
C_b:	ppm	bulk oxygen concentration in melt
C_o:	ppm	initial oxygen concentration in melt
C_f:	ppm	final oxygen concentration in melt
C_r:	ppm	oxygen concentration in melt in equilibrium with reducing gas
D:	m^2/s	diffusivity of oxygen in melt
F:	col./equi.	Faraday constant (96485)
I_{ion}:	A	ionic current through electrolyte
I_e:	A	electronic current through electrolyte
I_{ex}:	A	external short circuit current
$J_{O^{2-}}$:	equi./m^2-s	the flux of oxygen ions in the electrolyte
J_e:	equi./m^2-s	the flux of electrons in the electrolyte
M_{melt}:	kg	total mass of the melt
M_O:	kg/mol	molar mass of oxygen atom (0.016)
k_s:	atm$^{-1/2}$	Sieverts' law constant

7

k_p:	$atm^{-1/2}$	equilibrium constant for the reaction between reducing gas and oxygen
$Po_2^{\;i}$:	atm	oxygen partial pressure at the interface between melt and electrolyte
$Po_2^{\;r}$:	atm	oxygen partial pressure in the reducing gas
R:	J/K-mol	gas constant (8.314)
R_{ex}:	Ω	external resistance of the electrolyte cell
R_{ion}:	Ω	ionic resistance of the electrolyte
R_e:	Ω	average electronic resistance of the electrolyte
V:	l/min	flow rate of the reducing gases

ACKNOWLEDGMENTS

I. INTRODUCTION

The demand for metals with extra low concentrations of undesirable elements like oxygen (O), hydrogen (H) and sulfur (S) has increased as a result of the search for materials with better physical and mechanical properties. Present-day molten metal refining techniques include vacuum degassing and additions of reagent metals. The principle of the former technique is to create a vacuum over the surface of the molten metal and allow the impurity elements to evaporate out of the melt. This technique is capital intensive and is limited by the vacuum pressure that can be created over the molten metal. Vacuum degassing can also lead to the loss of other elements, and this can change alloy composition and properties. In the later technique reagent metals added into the melt form more stable compounds with the impurity elements and those compounds are subsequently removed. However, if these compounds are not completely removed, they remain in the melt as inclusions and have a detrimental effect on metal properties. Moreover, some of the reagent metals can also be very expensive. The reagent metals also go into solution in the metal being treated which can be undesirable.

Compared with the traditional techniques, the electrochemical deoxidation of the melt using an oxygen ion conducting electrolyte is a promising method for overcoming the problems mentioned above. In this technique oxygen diffuses through the electrolyte out of the melt either due to a chemical potential gradient or an external EMF or both. This will neither produce inclusions nor change the composition of the molten metal. There are many oxygen ion conducting electrolytes, and among them, zirconia based electrolytes are the most popular due to its excellent chemical stability in both oxidizing and reducing atmospheres.

After Kiukkola and Wagner's work [1], stabilized zirconia has been used in various types of electrochemical cells which have found many important laboratory and industrial applications, such as oxygen sensors for melts and gases, oxygen pumps, high-temperature fuel cells and steam electrolyzers. Overall the application of zirconia in electrochemical

cells can be divided into two categories: thermodynamic and kinetic. In thermodynamic studies, the open-circuit voltage under equilibrium conditions is measured and related to the chemical potential gradient across the electrolyte. This method has been used to measure the Gibbs free energy of numerous compounds. The application of oxygen sensors also falls in this category. In kinetic applications, electrolyte cells operate in either electrolytic or galvanic mode. Here, the current which passes through the electrolyte cell gives a measure of the rate of oxygen transport through the electrolyte. Solid oxide fuel cells (SOFCs) operate as galvanic cells, while oxygen pumps [2,3] operate as electrolytic cells.

Electrochemical deoxidation of molten metals can be divided into two categories: galvanic and electrolytic. In the electrolytic process, oxygen is pumped through the electrolyte by an external EMF. This process has been studied by several authors[4,5] employing Pt as electrodes. In the galvanic process, one side of the electrolyte is exposed to a reducing gas and the other side to molten metal, and oxygen ions migrate across the zirconia membrane due to the electrochemical potential gradient.

It is the intention of this study to carry out an in-depth investigation of the galvanic deoxidation process. Nickel cermet, fabricated using a new technique, is characterized and used as anodes in electrolyte cells. The deoxidation processes is modeled by taking into account all rate controlling steps at the same time, and the effect of the process parameters on the deoxidation kinetics is studied. Based on this work, a scale-up structure is proposed for a pilot-plant deoxidation trial.

As a guide to the readers, the contents of each chapter is described briefly here. Chapter II provides a survey of previous studies on electrochemical deoxidation, solid electrolytes and the copper-oxygen system. After a review of the previous work on electrochemical deoxidation, the work on electrolytes, especially on stabilized zirconia, is reviewed. The properties of zirconia based electrolytes, including phase stability, defect chemistry, and ionic and electronic properties, are discussed. Since the process pursued in

11

this study is closely related to the Solid Oxide Fuel Cell (SOFC) technology, which is gaining much momentum recently, the current status of SOFC technology with its limitations and promises is also discussed. Finally, the studies on the copper-oxygen system are reviewed.

In chapter III, an extensive survey of the state-of-art anode fabrication techniques is presented. Then a new fabrication technique consisting of slurry coating and infiltration that was used in this investigation is reported. Anodes made by this new technique are characterized with respect to their porosity, sheet resistance and long-term stability. Different from traditional methods, the porosity of the electrodes is accurately measured by a new technique.

Chapter IV focuses on the experimental procedure. In this chapter, detailed information on the experimental set-up and procedures is provided. To evaluate the effect of the mass transport of oxygen in molten copper on the deoxidation process, experiments were conducted under two different conditions: gas stirring in a resistance furnace and induction stirring in an induction furnace. The experimental parameters under these two stirring conditions are provided. The details concerning the measurement of the temperature gradient in the molten copper and across the electrolyte, the thermoelectric power between different metal wires, the oxygen partial pressure in gases, and the correction of voltage reading due to the induction heating are also discussed.

Chapter V is intended to provide a background for the readers to understand the deoxidation process. In this chapter, a typical deoxidation process is divided into five elementary steps and the possible rate-controlling steps are identified. Mass transfer in the molten metal is first discussed. Then the two electrode reactions, cathodic reaction at the interface between the electrolyte and molten metal and the anodic reaction at the interface between the electrolyte and Ni cermet electrode, are discussed. Finally, a discussion about gas diffusion in porous electrodes is provided. The transport of oxygen through the electrolyte is discussed in detail in chapter VI.

In chapter VI, the ionic transport in electrolytes as a function of external load and electronic conductivity is analyzed. The analysis begins with irreversible thermodynamics. Utilizing available information of the defect chemistry of stabilized zirconia, a general equation is obtained to describe the ionic transport. Finally this equation is simplified to obtain many previously reported results. The implications of those simplified results are also discussed.

Based on the analysis provided in chapter V and VI, the deoxidation process is modeled in chapter VII. The analysis begins with a general description of the deoxidation process. Then a simpler version of the problem, where forming gas ($N_2+5\%H_2$) is used, is discussed and equations are derived to model the deoxidation process. Based on the modeling results, a technique for measuring mass transport coefficients of oxygen in molten metals is developed. By using this technique, the mass transport coefficient of oxygen in molten copper has been measured as a function of process parameters, such as stirring intensity and process temperature. Digital simulation is also conducted to provide a more accurate picture of the deoxidation process.

In chapter VII, a scale-up structure is provided for conducting a possible pilot-plant trial. The deoxidation capability of the proposed scale-up structure is presented. Potential problems are identified.

II. LITERATURE SURVEY

In this chapter, the following three areas are surveyed: 1) previous studies on the electrochemical deoxidation using solid electrolytes; 2) solid electrolytes; 3) the copper-oxygen system. A review on anode fabrication techniques is provided in chapter III, which also includes device fabrication and characterization. Other three related fields, mass transport in fluid, mass transport of gas in porous media and electrode reactions are discussed in chapter V.

II.A. Deoxidaton Experiments

II.A.1. Deoxidation Using Electrolytic Cells

Since Kiukkola and Wagner's paper [6] on stabilized zirconia, many workers have tried to use electrolytic cells to refine melts. Korousic and Marincek [7] and Fisher and Janke [8] first did some work in this field. Korousic charged copper in a zirconia tube and dipped this tube inside a copper melt. The copper melts (inside and outside the tube) were used as electrodes and external voltage was applied to pump oxygen from one melt to the other. In Fisher's work, Pt paste was used instead of the copper melt (inside the tube). Once again, an external EMF was used to deoxidize the melt. In 1970's, Oberg et. al. [9] used zirconia crucible to contain the copper melt and applied Pt paste on the outer surface of the crucible. The outer surface of the crucible was kept in contact with air and the porous Pt paste served as the anode while the copper melt was employed as the cathode. Here also external voltage was applied to deoxidize the melt. Later Odel [10] used the same setup to study the interfacial concentration and current efficiency.

In all these work, external EMF was used to pump oxygen across the electrolyte from the copper melt (at low oxygen potential) into air (at high oxygen potential). To achieve commercial use, current efficiency and cost are of crucial importance. But if this method is used at a higher temperature, e.g. deoxidizing steel melts, the electronic conductivity in stabilized zirconia electrolyte would appreciably decrease the current

14

efficiency; for calcia stabilized zirconia (CSZ) this decrease is reported to be around 30 percent when oxygen concentration in the melt is below 300ppm [11]. Also, in the electrolytic process, the choice of Pt as an electrode would make the commercialization of this technique all but impossible. It is also worth noting that, in this method, the interfacial oxygen concentration at the electrode/electrolyte interface can decrease to a very low value and start decomposing the electrolyte. In view of this problem, Oberg et. al [12] proposed a programmed decrease in the applied voltage so that the electrolyte would not undergo a decomposition at the electrode/electrolyte interface. In order to circumvent all these difficulties, it is desirable to devise a galvanic method for deoxidizing the melts.

II.A.2. Deoxidation by Semipermeability

For most zirconia-based solid electrolytes, high ionic conductivity is an essential requirement for various applications. However, these materials also exhibit an additional electronic conductivity. This has two main consequences in galvanic cells. One is that the measured voltage will be lower than the theoretical value. The other is that a flux of free electrons or holes will stream continuously through the electrolyte and will be electrically compensated by a counter migration of oxide ions. The net effect is a flux of oxygen through the materials. The phenomenon is called oxygen electrochemical semipermeability. In 1980's, Iwase et. al. [13] made use of this phenomenon to deoxidize molten steel. They inserted a one-end-closed calcia stabilized zirconia (CSZ) tube into the molten steel and passed a CO/CO_2 gas mixture through the tube. In their experiment, molten steel served as a cathode and the electrolyte at the electrolyte/reducing gas interface as an anode.

Iwase's method is galvanic in nature. However, since metallic anode was not used in his experiment, the electrode reaction was impeded. Besides, this method totally relied on the residual electronic conductivity of the fast ion conductor to maintain electroneutrality during the deoxidation process and therefore the deoxidation process was

slow. At lower temperature (for copper melts), Iwase's method will not be suitable for deoxidation since the semipermeability of the electrolyte would be negligible.

II.B. Solid Electrolyte

II.B.1. Solid Electrolyte

According to Tuller[14], solid electrolytes, which are also referred as fast ion conductors, can be divided into two categories according to their conducting mechanism. One category includes materials which are intrinsically disordered, such as α-AgI, δ-Bi_2O_3 and β-Al_2O_3. The other includes materials which are highly defective, such as doped ZrO_2 and doped CeO_2. Since there have been numerous papers and books on electrolytes, here only the zirconia system is briefly reviewed.

Zirconia is a system which has been under intensive investigation. It is well documented that zirconia undergoes the following transformations as the temperature changes[15]:

$$\text{monoclinic} \xleftarrow{\ 1170^\circ C\ } \text{tetragonal} \xleftarrow{\ 2370^\circ C\ } \text{cubic} \xleftarrow{\ 2680^\circ C\ } \text{liquid}$$

The cubic structure of zirconia is a fluorite structure, where the cations occupy the corners and face centers of a unit cell and anions sit in the centers of tetrahedrons formed by cations. The arrangement of ions in the tetragonal structure and the monoclinic structure is similar to that in the cubic structure but with a lower symmetry.

Among the phase transformations listed above, the phase transformation from tetragonal to monoclinic has been intensely studied using a variety of techniques due to the theoretical as well as practical interests[16,17,18]. This transformation is characterized by the abrupt change in lattice constant which leads to a large volume change (3% to 5%). However, the addition of CaO, MgO, Y_2O_3, and some other rare earth oxides lowers the two transition temperatures (monoclinic-tetragonal and tetragonal-cubic). The phase diagrams of the binary oxide systems have been reviewed by Stubican[19]. It shows that when the dopant is present in a concentration larger than a certain value, zirconia can be

16

fully stabilized, i.e., the cubic fluorite structure of ZrO_2 can be stabilized to room temperature. There have been many papers [20,21] about this structure and its stability. When the dopant concentration is less than that needed for a complete stabilization, a partially stabilized zirconia, i.e., a mixture of cubic and monoclinic (or tetragonal) zirconia, is obtained.

II.B.2. Electrical Properties of Stabilized Zirconia

The addition of di- or trivalent oxides not only stabilizes zirconia, but also creates a larger concentration of oxygen vacancies. According to defect chemistry (Kröger-Vink notations), for Y_2O_3 stabilized zirconia,

$$Y_2O_3 \xrightarrow{ZrO_2} 2Y_{Zr}^{'} + V_O^{\cdot\cdot} + 3O_O^{\times}$$
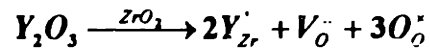
The large concentration of oxygen vacancies facilitates the diffusion of oxygen ions in the stabilized zirconia since oxygen-ion conduction takes place by the movement of oxygen ions via vacancies. Electrical properties of yttria-stabilized zirconia have been studied by many authors[22,23,24,25,26,27,28].

In reducing atmospheres, the stabilized zirconia behave as an n-type conductor and the electron concentration is determined by the following reaction:

$$O_O^{\times} = V_O^{\cdot\cdot} + 2e^{'} + \frac{1}{2}O_2(g)$$
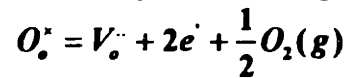
$$K_1 = P_{O_2}^{1/2} * n^2 * C_{V_O^{\cdot\cdot}}$$

where $C_{V_O^{\cdot\cdot}}$ and n are the concentrations of oxygen vacancies and electrons, respectively. K_1 is the reaction constant.

It has been reported that, over a wide range of temperature, the ionic conductivity of stabilized zirconia is independent of oxygen partial pressure over several orders of magnitude[29,30]. Accordingly, $C_{V_O^{\cdot\cdot}}$ remains constant, and σ_e can be expressed as

$$\sigma_e = \sigma_e^o * P_{O_2}^{-1/4}$$

This equation has been accurately verified[31,32,33].

In the literature, electrical properties of the stabilized zirconia are usually reported in terms of the ionic conductivity σ_{ion} and P_θ. P_θ is defined as the oxygen partial pressure when $\sigma_{ion} = \sigma_e$, i.e.,

$$\sigma_{ion} = \sigma_e^o * P_\theta^{-1/4}$$

As shown in Fig. II-1, when yttria concentration is lower than 8 mol%, both σ_{ion} and σ_e^o of the yttria stabilized zirconia (YSZ) decrease with the decrease of the yttria concentration. At 1473K, σ_e^o of YSZ with 5.8 mol% yttria is reported to be 1.1×10^{-7}-1.3 $\times10^{-7}$ S-atm$^{1/4}$/cm and σ_{ion} around 0.2 S/cm[34]. Some studies report smaller σ_e^o , e.g., 1.1×10^{-7} S-atm$^{1/4}$/cm for YSZ with 9mol% yttria at 1473K[35], or larger σ_{ion} , e.g., 0.31S/cm for YSZ with 3mol% yttria at 1473K[36]. Other reports also give similar results[37]. Based on the literature, for YSZ with 4.5mol% yttria, which is used in this study, σ_{ion} should be in the range from 0.1-0.5S/cm. It will be demonstrated in chapter VII that, as long as σ_{ion} varies within this range, the error caused by the variation of σ_{ion} is less than 2%. Similarly, σ_e^o is expected to be around 10^{-7} S-atm$^{1/4}$/cm. It will be shown in chapter VII that, the value of σ_e^o obtained from curve fitting is consistent with the reported results.

II.B.3. Applications in Batteries and Fuel Cells

Among the many applications of solid electrolytes, the most important applications are for energy storage and conversion systems, i.e., used in galvanic cells. Compared with liquid electrolyte, solid electrolyte has the distinctive advantage of stability. Usually liquid electrolyte is corrosive and the corrosion of electrodes limits the time during which the system can be stored. Another problem associated with liquid systems is the leakage problem. Compared with liquid electrolytes, solid electrolytes are free from these problems and therefore have found many applications in energy systems. For example, β-Al_2O_3 has been used in Na-S batteries; α-AgI in silver batteries.

The application of the stabilized zirconia in energy conversion systems is in solid oxide fuel cell(SOFC). Since the technology reported in this study is closely related to the

SOFC technology, i.e., the devices used in this study actually operate as a SOFC, the SOFC technology is surveyed in the following part.

Since early 1980's, the research on solid oxide fuel cell(SOFC) has gained much momentum due to the increasing demand for clean environment and the breakthrough of tubular SOFC technology. Detailed description of SOFC system has been provided by Minh[38]. State-of-art solid oxide fuel cells (SOFCs) use yttria doped zirconia as electrolyte, strontium doped lanthanum manganite as cathode, $Ni-ZrO_2$ as anode and lanthanum chromite as interconnect materials. Fuel gas (natural gas) and air are used on anode and cathode side, respectively. In the present technology, electrolyte is dense stabilized zirconia with a thickness of 5 to 100μm, anode is 20-40% porous $Ni-ZrO_2$ cermet about 100μm in thickness, cathode is doped (A-site) $LaMnO_3$ with a porosity of 30% and a thickness of 100μm and the interconnect materials is dense doped (A/B site) $LaCrO_3$ 30 to 1000μm thick or metal alloys based on the Fe-Cr-Ni-Co system.

There are three main designs of SOFCs: tubular, planar and monolithic. Compared with the tubular configuration, planar and monolithic structure can potentially have higher current densities and better system efficiency. The key problem of the planar design is its sealing, while that of the monolithic structure is the mismatch of thermal expansion between different components.

Currently SOFCs are operated at about 1000°C. At this temperature, there are following problems:

1). Interdiffusion and interaction between cell components

2). Lack of chemical stability of individual components

3). Densification of porous electrodes

4). Delamination of cell components due to thermal expansion mis-match

5). Lack of availability of proper sealing materials for planar configuration

Furthermore, high operating temperature also increases operating costs. If the operating temperature of SOFCs can be lowered to about 800°C, the problems mentioned

can be either solved or greatly alleviated. However, before that can be achieved, the following problems need to be solved:

1). At lower temperature, electrode kinetics are expected to be much slower. Therefore we need to find new materials which have higher electrochemical activity.

2). Another problem associated with lower operating temperature is the IR drop from components. Currently, the main contribution of IR drop is from cathode and electrolyte. The activation energy of ionic conduction in yttria-stabilized zirconia is relatively high (about 8.4ev). Therefore the lowering of operating temperature will increase the electrolyte resistance by an order of magnitude. This means that the IR drop due to the electrolyte will also increase by an order of magnitude. This will significantly decrease the efficiency of the fuel cell. One solution to this problem is to decrease the thickness of the electrolyte. Currently the thickness of the electrolyte is around 100μm. The thickness could be decreased by two to four folds. However, thinner electrolytes will have less mechanical strength and therefore decrease cell life. Another option is to use electrolytes with higher ionic conductivity. At present, no such electrolyte which is stable in both oxidizing and reducing conditions is available and is therefore the subject of numerous current investigation.

II.C. Cu-O system

The Cu-O system has been studied by many authors [39,40,41,42,43,44,45,46]. The study has shown that the solubility of oxygen in copper melts at around 1400K is well above one thousand ppm by weight. The equilibrium between oxygen and gas phase can be described by the reaction

$$\frac{1}{2}O_2(g) \rightarrow \underline{O}\,(melt)$$
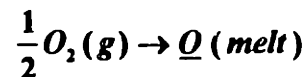
and its equilibrium constant k_s can be calculated as

$$k_s = \frac{a_O}{(P_{O_2})^{\frac{1}{2}}}$$

$$= \exp(-\frac{\Delta G^o}{RT})$$

where ΔG^O is the Gibbs free energy for the above reaction. The activity of oxygen is related to the concentration of copper by the activity coefficient γ, which is defined as

$$\gamma = \frac{a_O}{[\underline{O}]}$$

Activity coefficient γ_i of element i is a function of the concentration of other alloy elements existing in liquid copper. The effect of solute elements on γ_i can be expressed by free energy interaction coefficients introduced by Wagner [47] and later used by Chipman[48], Lupis and Elliott[49,50,51,52,53]. Briefly, in this theory, the activity coefficient γ_i of element i can be expressed as:

$$\log_{10}\gamma_i = \sum_{j=2}^{n} e_i^j [wt.\%_j] + \sum_{j=2}^{n} r_i^j [wt.\%_j]^2 + \sum_{j=2}^{n}\sum_{\substack{k=2\\j<k}}^{n} r_i^{j,k}[wt.\%_j][wt.\%_k] + O(\%^3)$$

where $[wt.\%_j]$ is the concentration of element j and the solvent has been designated as component 1 in the n-component system. e_i^j, r_i^j and $r_i^{j,k}$ are the first, second and cross product second term interaction coefficients of element i, respectively, which are defined as

$$e_i^j = \frac{\partial \ln \gamma_i}{\partial [wt.\%_j]}\bigg|_{T,P,X_1\to 1}$$

$$r_i^j = \frac{\partial^2 \ln \gamma_i}{\partial [wt.\%_j]^2}\bigg|_{T,P,X_1\to 1}$$

and

$$r_i^{j,k} = \frac{\partial^2 \ln \gamma_i}{\partial [wt.\%_j]\partial [wt.\%_k]}\bigg|_{T,P,X_1\to 1}$$

Generally $r_i^{j,k}$ is neglected. e_i^j and r_i^j have been measured experimentally in many systems. An excellent survey of interaction coefficients in molten copper has been

21

provided by Elliott[54]. A table of interaction coefficient in molten copper is listed in Table II-1.

Table II-1   Interaction Coefficients in Liquid Copper

Element j	e_o^j	r_o^j	T (°C)
Ag	0	0	1100-1200
Au	0.015	0	1200-1550
Co	0.32	0.023	1200
Fe	-20,000/T+10.8	(0.01)	1200-1350
Ni	-169/T+0.079	(0)	1200-1300
P	6,230/T+3.43	0	1150-1300
Pb	-0.007	-0.0001	1100
Pt	0.057	0	1200
S	-0.164	0	1206
Si	(-62)	0	1250
Sn	-0.009	-0.0001	1100

Based on the chemical analysis of copper, which is listed in Appendix II, it is found that the effects of other elements on the oxygen activity are relatively small, and the activity coefficient of oxygen in molten copper can be taken as unity.

The diffusivity of oxygen in molten copper has also been studied by several authors. A general survey on the techniques of the oxygen diffusivity measurement can be found in [55]. It has been proposed that the diffusion of oxygen can be regarded as an activated process, and the relationship between diffusivity and temperature can be expressed as

$$D = D^o \exp(-E_o / RT)$$

22

where D is the diffusivity of oxygen, D^O is the pre-exponential term and E_O is the activation energy for oxygen diffusion in molten copper. The previous results are summarized in Table II-2.

Table II-2 Comparison of Diffusion Results

$$D = D^o \exp(-E_o / RT)$$

Shurygin and Kryuk[56]	$D = 1.55 \times 10^{-4} \exp(-34,853 / RT)$
Osterwald and Schwarzlose[57]	$D = 2.63 \times 10^{-3} \exp(-39,204 / RT)$
Rickert and El-Miligy[58]	$D = 1.22 \times 10^{-2} \exp(-60,250 / RT)$
El-naggar and Parlee[59]	$D = 7.25 \times 10^{-3} \exp(-65,781 / RT)$
Oberg et al.[60]	$D = 6.9 \times 10^{-3} \exp(-53,974 / RT)$
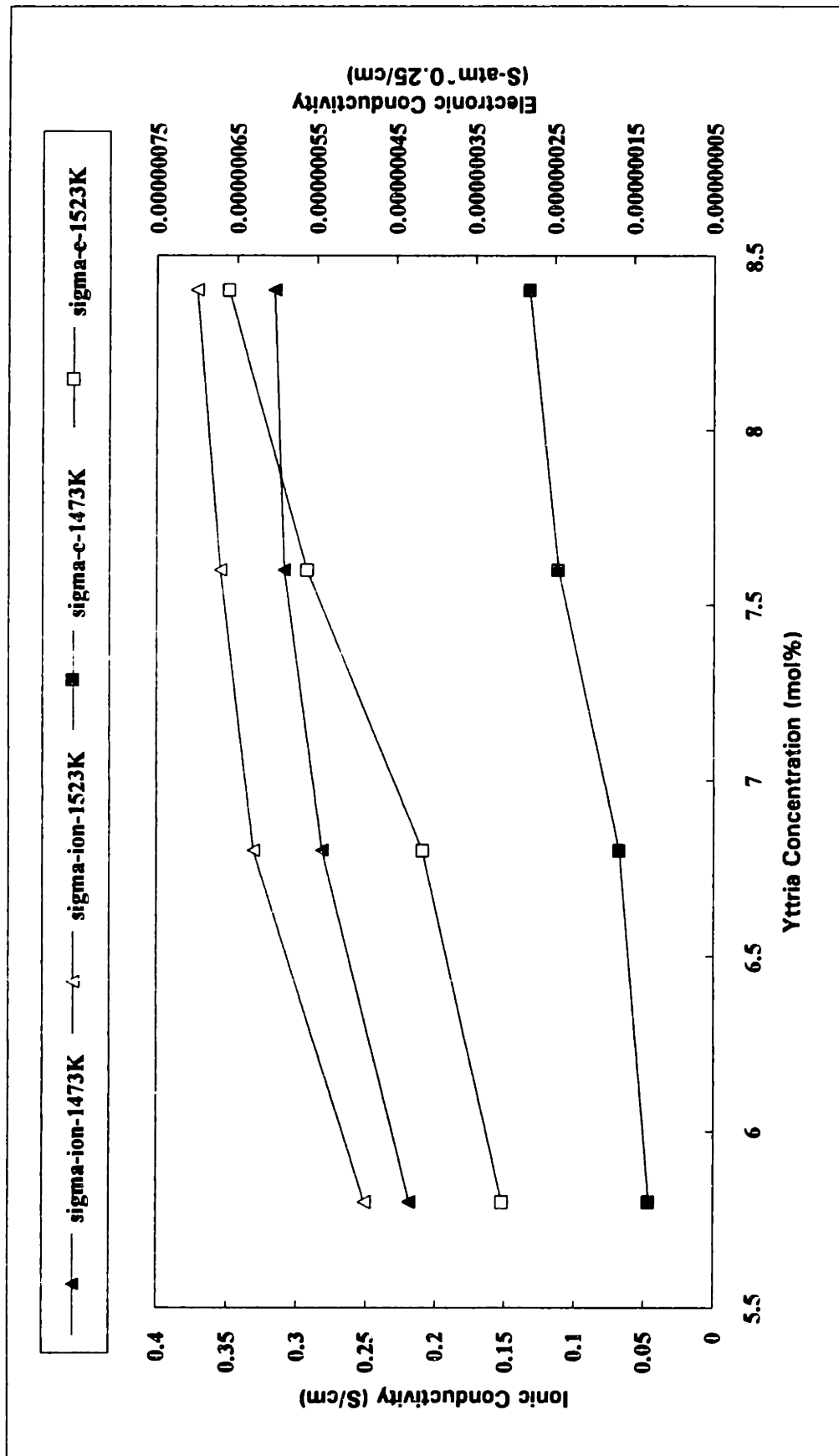
Figure II-1   Ionic and Electronic Conductivity of YSZ as a Function of Yttria Concentration [34]

III. ANODE FABRICATION AND CHARACTERIZATION

III.A. Introduction

As discussed in chapter II, Pt has been used as an electrode material in previous studies on electrochemical deoxidation. Since Pt loses its electrochemical activity in a reducing atmosphere, especially when hydrogen is present, it is not suitable for use as an anode material in a galvanic deoxidation process. Moreover, the high cost of Pt makes the electrolytic deoxidation process too expensive for commercialization. For successful commercialization the electrode materials and the deposition technique must be affordable. The chapter addresses these issues.

With the development of the Solid Oxide Fuel Cell (SOFC) technology, Ni-Zirconia cermet has proved to be a promising candidate for use as an electrode material in reducing atmosphere. The use of Ni as the electronic component of the electrode material is mainly due to the following reasons:

1. Stable in reducing atmosphere containing H_2, CO, CH_4, etc.

2. High catalytic activity for steam reforming of hydrocarbons

3. Ni is relatively inexpensive, compared to cobalt and other noble metals.

High temperature operation has put many constraints on the electrode materials. For a cell to perform efficiently, the electrodes must have matching thermal expansion coefficients to adhere well to the electrolyte during operation and under thermal cycle. In addition, the electrodes must have the lowest possible electrical resistance and remain porous during operation, i.e., not sinter, in order to allow easy gas phase diffusion to and from the electrolyte interface for effective charge transfer reaction. Hence, a good electrode is one which is adhering, has high stable porosity and low sheet resistance. Westinghouse has solved this problem by employing the electrochemical process(EVD) [61,62,63,64], which involves Ni slurry coating and a skeletal embedding growth of yttria stabilized zirconia. As shown in Fig. III-1, after the stabilized zirconia is coated with nickel slurry, one side of it is exposed to oxygen (high oxygen partial pressure side) while the

other side to a mixture of argon, hydrogen and chlorides of zirconium and yttrium (low oxygen partial pressure side). Due to the oxygen partial pressure difference, oxygen ions migrate to the chloride side and electrons to the oxygen side to maintain electroneutrality. As indicated in Fig. III-1, oxygen ions react with the chlorides to form yttria stabilized zirconia, which deposits at the interface between the nickel cermet and the stabilized zirconia substrate. This skeletal growth of zirconia and yttria extends from the electrolyte/anode interface into the nickel cermet, forming a composite structure. Though anodes produced by this technique have high electrochemical activity and long-term stability, this technology is quite labor-intensive and expensive.

There are also other processes [65,66,67] which involve less expensive techniques, such as screen printing or tape casting a layer of NiO and stabilized zirconia over the electrolyte followed by reduction of the NiO to metallic nickel[68]. There are also some reports about the properties of the cermet fabricated using these techniques[69,70]. These processes are sensitive to the particle size of the NiO because the contact area between the particles changes during the course of the reduction process. Furthermore, the reduced Ni particles often have a core of NiO when the size of NiO particle is larger than $3\mu m$[71]. As a result, these electrodes have higher sheet resistance.

The process used in this study is a modified version of an earlier reported process [72]. Its objective is to produce cermet with a microstructure somewhat similar to that obtained by utilizing EVD. Briefly, it consists of slurry coating and sintering a layer of nickel and zirconia followed by pressure infiltrating zirconia and re-sintering. The infiltration of zirconia suspension is intended to achieve the following:

1) The infiltration will produce a layer of zirconia extending from the electrode/electrolyte interface to the outer surface of the electrode. After the second sintering this layer of zirconia will make the electrode adhere well to the electrolyte substrate.

2) It has been postulated[73] that electrode reactions occur at the triple phase boundary of the gas, electrolyte and the metal electrode. Several authors[74] have proposed techniques

26

to deposit a thin film of yttria-stabilized-zirconia on tne surface of the nickel cermet. It is expected that the infiltration of zirconia suspension will deposit a thin film of YSZ which will increase the triple phase boundary.

3) It has been speculated that the long-term stability of the Ni cermet deposited by utilizing EVD process is due to the growth of a thin film of YSZ on part of the nickel metal surface. It is thought that this thin film of zirconia prevents the cermet from sintering during long term operation. The infiltration process is also expected to produce a similar cermet structure.

A detailed description of the cermet fabrication process and its characterization is described below.

III.B. Fabrication of Ni-ZrO$_2$ Cermet Electrodes

The flow chart for depositing the cermet electrode is shown in Fig. III-2. The porous Ni-ZrO$_2$ cermet was deposited over the inner walls of a one-end-closed yttria-stabilized zirconia tube (8 wt% yttria, ZIRCOA, Inc.) which had an internal diameter of 9.5 mm and was 2 mm thick. Some deposition experiments were also conducted wherein the cermet was deposited over the outer walls of the tube.

The electrode is deposited by a slurry coating process. The slurry is prepared as follows: PVA powder(fully hydrolyzed polyvinyl alcohol, grade 75-15, Dupont Elvanol) is dissolved in water at around 80°C. Then ZrO$_2$ powder containing 13.16 wt% Y$_2$O$_3$ (TZ-8Y, TOSOH Corporation) is added into the PVA solution water while stirring. Finally Ni powder (type 287, NOVAMET) is added into the same solution. The composition of the Ni powder can be found in the Appendix of the thesis. (Its specific surface area (BET) and particle size are 0.58-0.68M^2/g and around 2.2 μm, respectively, provided by NOVAMET Co.). The overall composition of the slurry is listed in Table III-1.

Table III-1 Overall Composition of Slurry

Composition	Ni	PVA solution (6wt% PVA)	YSZ powder (13.16%wt Y_2O_3)
wt%	40	60	5-15% of Ni content

The particle size of YSZ powder was measured to be around 0.5μm by using the centrifugal particle size analyzer (Horiba model CAPA-500). Before measurement is conducted, zirconia powder is dispersed using an ultrasonic liquid processor and a cell disruptor (Sonicator™ Model W-20F). Zirconia tubes are washed using acetone and deionized water prior to the coating process. The coating process consists of dipping (or filling) the zirconia tube (closed at one end) at room temperature with the pre-made slurry. The tube is then inverted and the slurry is allowed to run out leaving a layer of the slurry adhering to the outer (inner) wall of the tube. The tube is then turned horizontally and it is slowly rotated at a steady speed during the drying process to get a uniform layer of the slurry. After the slurry has dried the tube is sintered at 1373K for 17 hours under an atmosphere of nitrogen with 2% water vapor followed by natural cooling under an atmosphere of nitrogen with 5% hydrogen. The slightly oxidizing atmosphere during sintering oxidizes the surface of nickel particles and improves its adherence to the electrolyte, while the reducing atmosphere during cooling reduces the NiO formed during sintering. It is found that changing to the reducing atmosphere before cooling is crucial to the performance of the electrodes, otherwise the sheet resistance of the electrodes significantly increases. At the end of this sintering step, a porous layer of nickel adhering to the outer (inner) walls of the zirconia tube is obtained. The zirconia tube is then introduced into a vacuum infiltration chamber shown in Figure III-3. The vacuum chamber is maintained at a pressure of 667 Pa (5 torr) and a zirconia suspension containing 30 vol.% ZrO_2, 70 vol.% water and nitric acid (to keep the pH value of the suspension

around 3.0) is introduced into the chamber in order to completely immerse the zirconia tube in the slurry. Then the vacuum chamber is opened to the atmosphere and the zirconia slurry partially infiltrates the pores of the nickel layer that is present on the outer (inner) walls of the zirconia tube. Following this infiltration step the zirconia tube is sintered for the second time at 1473K for 7 hours under an atmosphere of nitrogen with 5% hydrogen. The final product is a zirconia tube with a layer of nickel-zirconia cermet adhering to the outer (inner) walls of the tube. It may be noted that it was not possible to physically remove the cermet from the zirconia tube without fracturing the electrode. This demonstrated that the cermet adhered well to the zirconia substrate.

The procedure outlined above is ideally suited for depositing the Ni-ZrO_2 cermet on either the outer or the inner walls of the electrolyte in tubular solid oxide fuel cells. However, the process can also be used to deposit the cermet (anode) on planar cells if the cathodic on the other side of the electrolyte can be successfully kept isolated from the reducing processing environment of the cermet.

III.C. Characterization of Electrodes

III.C.1. Porosity Measurement

In industry the porosity of cermet is usually estimated from micrograghs. In this study an Archimedean method was used to measure the porosity of cermets.

The Ni-ZrO_2 cermet consists of a three phase structure which includes the Ni particles, the ZrO_2 particles and the pores (gas phase). The porosity (η) of the cermet is defined as:

$$\eta = \frac{V_P}{V_P + V_N + V_Z} * 100 \qquad [III-1]$$

where $V_P, V_N,$ and V_Z are the volumes occupied by the pore, nickel and the zirconia particles, respectively in the cermet.

The method used for measuring the porosity, while depositing the Ni-ZrO$_2$ cermet over the zirconia tube, is outlined below:

(1). The zirconia tube to be coated with the cermet is weighed (W_o^s) and its volume (V_{tube}) is equal to $W_o^s / (\rho^T - \rho^s)$, where ρ^T and ρ^s are the densities of the zirconia tube and air respectively.

(2). The weight fraction of nickel in the nickel-zirconia slurry (ξ) that is used for coating the tube, is noted.

(3). The slurry coated tube is sintered and weighed (W_1^s)

(4). The tube is weighed again at the end of the zirconia infiltration and the second sintering step (W_2^s)

(5). Next, petroleum jelly is heated to around 333K and the tube with the cermet is dipped into the liquid petroleum jelly. After dipping, the tube is immediately removed, forced air cooled and weighed (W_3^s)

penetrating into the pores. The volume of the jelly coating (V_{jelly}) is equal to $(W_3^s - W_2^s) / (\rho^j - \rho^s)$, where ρ^j is the density of the jelly.

(6). The same cermet tube coated with the petroleum jelly is weighed again in liquid water W_3^l

The volume of the tube with the jelly coating (V_{total}) is equal to $(W_3^s - W_3^l) / (\rho^l - \rho^s)$, where ρ^l is the density of liquid water.

It should be noted that, in step (5), instead of petroleum jelly one could use any other material having a low melting point. However, it is important that the material in its liquid state must have a high surface tension. This way the material will cover the exterior (outer surface) of the cermet.

From these measurements, the volumes of the nickel (V_N) and zirconia particles (V_Z) and the pores (V_P) can be calculated as follows:

$$V_N = \frac{(W_1^s - W_o^s)\xi}{(\rho^N - \rho^s)}$$

[III-2]

$$V_Z = \frac{(W_1^s - W_o^s)(1 - \xi) + (W_2^s - W_1^s)}{(\rho^Z - \rho^s)}$$

[III-3]

where ρ^Z is the density of the zirconia particles.

$$
\begin{aligned}
V_P &= V_{total} - V_{tube} - V_{jelly} - V_Z - V_N \\
&= \frac{(W_3^s - W_3^l)}{(\rho^l - \rho^s)} - \frac{W_o^s}{(\rho^T - \rho^s)} - \frac{(W_3^s - W_2^s)}{(\rho^J - \rho^s)} \\
&\quad - \frac{(W_1^s - W_o^s)(1 - \xi) + (W_2^s - W_1^s)}{(\rho^Z - \rho^s)} - \frac{(W_1^s - W_o^s)\xi}{(\rho^N - \rho^s)}
\end{aligned}
$$

[III-4]

Expressions for V_N, V_Z and V_P from the above equations can be substituted in equation [III-1] and the porosity can be expressed as:

$$
\eta = \frac{\frac{(W_3^s - W_3^l)}{(\rho^l - \rho^s)} - \frac{W_o^s}{(\rho^T - \rho^s)} - \frac{(W_3^s - W_2^s)}{(\rho^J - \rho^s)} - \frac{(W_1^s - W_o^s)(1 - \xi) + (W_2^s - W_o^s)}{(\rho^Z - \rho^s)} - \frac{(W_1^s - W_o^s)\xi}{(\rho^N - \rho^s)}}{\frac{(W_3^s - W_3^l)}{(\rho^l - \rho^s)} - \frac{W_o^s}{(\rho^T - \rho^s)} - \frac{(W_3^s - W_2^s)}{(\rho^l - \rho^s)}} \bullet 100
$$

[III-5]

The measurement described above gives us a much more accurate quantitative description of the actual average porosity of the cermet than that obtained from microscopic evaluation. However, this type of measurement does not give information about the tortuousity in the cermet.

Ni-ZrO$_2$ cermet electrodes were deposited as described earlier and the porosity measurements conducted on three of these electrodes are tabulated in Table III-II. These three porosity measurements typically represent the average (33.7%), the lowest (30.4%) and the highest (36.6%) porosity values. These measurements indicate that the process

31

described can consistently deposit cermet electrodes having porosity within a narrow range (30% to 37%). The optical micrograph picture of the sectioned cermet electrode used in porosity measurement #1 is shown in Fig. VII-4. This micrograph shows the typical structure of the cermet in terms of the distribution of the nickel and zirconia particles, and the pores.

III.C.2. Sheet-Resistance Measurement

Four-terminal technique was used to measure the sheet resistance (or the spreading resistance) of the Ni-ZrO_2 cermet electrodes. A schematic of the set up is shown in Figure III-5. The two end terminals are 3 to 7 cm apart and are connected to a power supply (KEPCO MSK 10-10M) in series with an amperemeter. The two inner terminals are 1.7 to 3 cm apart and are connected to a voltmeter. The four terminals are constructed by tightly wrapping 0.5 mm diameter nickel wires around the cermet that is deposited over the yttria-stabilized zirconia tube. The high temperature measurements were all made in a 5% H_2-N_2 environment in order to prevent the oxidation of the nickel. The sheet resistance (spreading resistance) of the Ni-ZrO_2 cermet (S_R) in such an arrangement can be expressed as:

$$S_R = \frac{\rho}{\delta} = \frac{V}{I} \cdot \frac{C}{L}$$

[III-6]

where ρ is the resistivity of the cermet

δ is the thickness of the cermet layer

V is the voltmeter reading

I is the amperemeter reading

C is the circumference of the tube and

L is the spacing between the two inner terminals.

The thickness of the deposited cermet electrodes varied from 150 microns to 30 microns. The room temperature sheet resistance of these electrodes varied from 0.0064 Ω/ $\square$ to 0.019 Ω/$\square$.

III.C.3. High-Temperature Stability

As stated in the discussion of solid oxide fuel cell (SOFC) technology in chapter II, the densification of the Ni cermet is one of the factors which limits the life of the SOFC. Nickel has a lower melting point (1,726K), which lowers the sintering resistance of Ni-YSZ cermet. There is very little information available on the sintering behavior of Ni-cermet electrodes[75]. It is shown that YSZ particle size and the ratio of YSZ/Ni-YSZ have a remarkable influence on the dimensional stability of the Ni cermet, which is also closely related to the interfacial resistance of the electrode reactions. It is reported that the Ni-zirconia cermet with 10wt% YSZ and YSZ particle size 0.5μm undergoes a significant dimensional change.

In order to evaluate the long term stability of these electrodes, the sheet resistance of these electrodes were measured as a function of time at 1273K, 1373K and 1473K. These measurements are plotted in Fig. III-6. It can be seen from Fig. VII-6 that the sheet resistance of the cermet, between 1273K and 1473K, did not decrease with holding time. This indicated that the electrodes did not undergo any major sintering at these temperatures. However, interestingly we do see a very slight initial increase in the value of the sheet resistance of these electrodes. For instance, when the cermet electrodes are held at 1473K, 1373K and 1273K the corresponding increases in the value of the sheet resistance during the first 30 hours of annealing are 9.1%, 5.6% and 2.2% respectively. But, after 30 hours, the sheet resistances of these electrodes do not continue to increase and they become quite stable. This observation suggests that, during the first 30 hours of annealing, the nickel particles may be undergoing some slight shrinkage which interrupts their connectivity. For example, before annealing some nickel particles may touch each other loosely but is not connected. During annealing those fibrous particles tend to

become spherical and this lead to the interruption of their contact. Optical micrographs of the cermet electrode before and after the 100 hour annealing treatment at 1373K is shown in Fig. III-7. From these micrographs it is evident that the cermet electrodes do not undergo any noticeable structural changes during annealing. Furthermore, since the overall increase in sheet resistance is very small in 100 hours, it is also not possible to distinctly identify the micro-structural changes associated with this increase.

The cermet fabricated by the technique described above has been used in studying the galvanic deoxidation process. It is observed that the total resistance of electrolyte cell is quite stable over about one week. This observation is consistent with the long term stability test reported above.

From eq.[III-6] it is apparent that by increasing the thickness of the cermet electrode one can decrease the spreading resistance of the electrode. However, by increasing the thickness and depending on the porosity of the cermet one would also increase the resistance to gas phase diffusion which could in turn result in higher polarization losses. Therefore, there is an optimum cermet thickness beyond which the polarization losses begin to dominate. The best cell performance was obtained when these electrodes had thickness between 50 and 150 microns.

oxygen

$$ZrCl_4(g) + 2O^{2-} = ZrO_2(s) + 2Cl_2(g) + 4e^-$$

Anode $\qquad ZrCl_4(g) + 2O^{2-} = ZrO_2(s) + 2Cl_2(g) + 4e^- \qquad$ and

$$2YCl_3(g) + 3O^{2-} = Y_2O_3(s) + 3Cl_2(g) + 6e^=$$

Cathode $\qquad O_2(g) + 2e^- = O^{2-}$
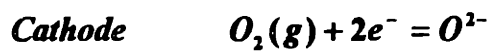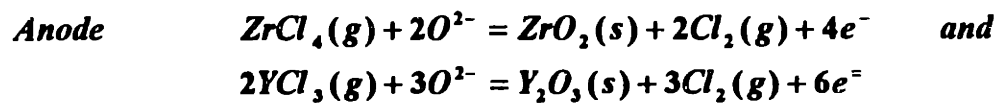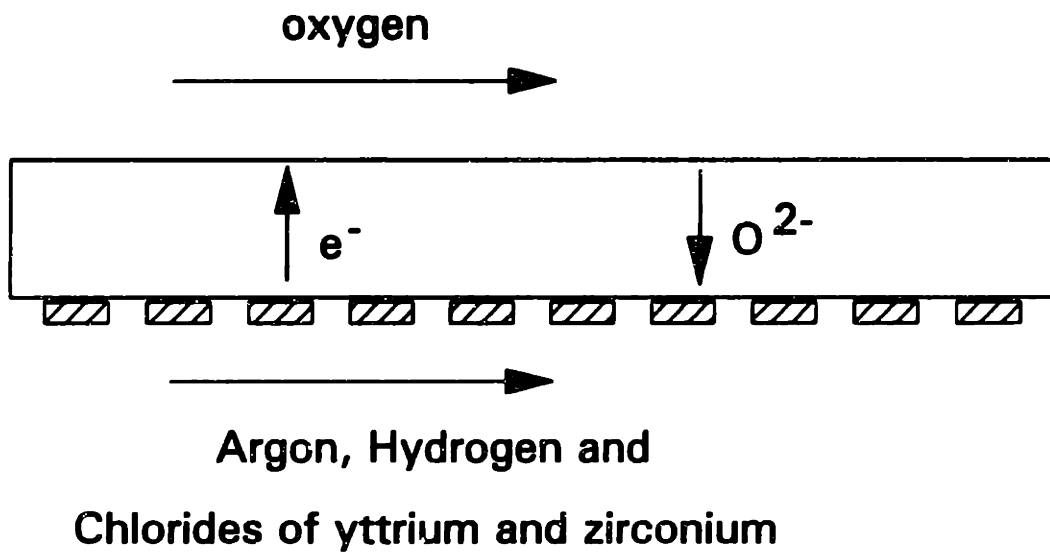
Figure III-1   Principle of EVD Process

35
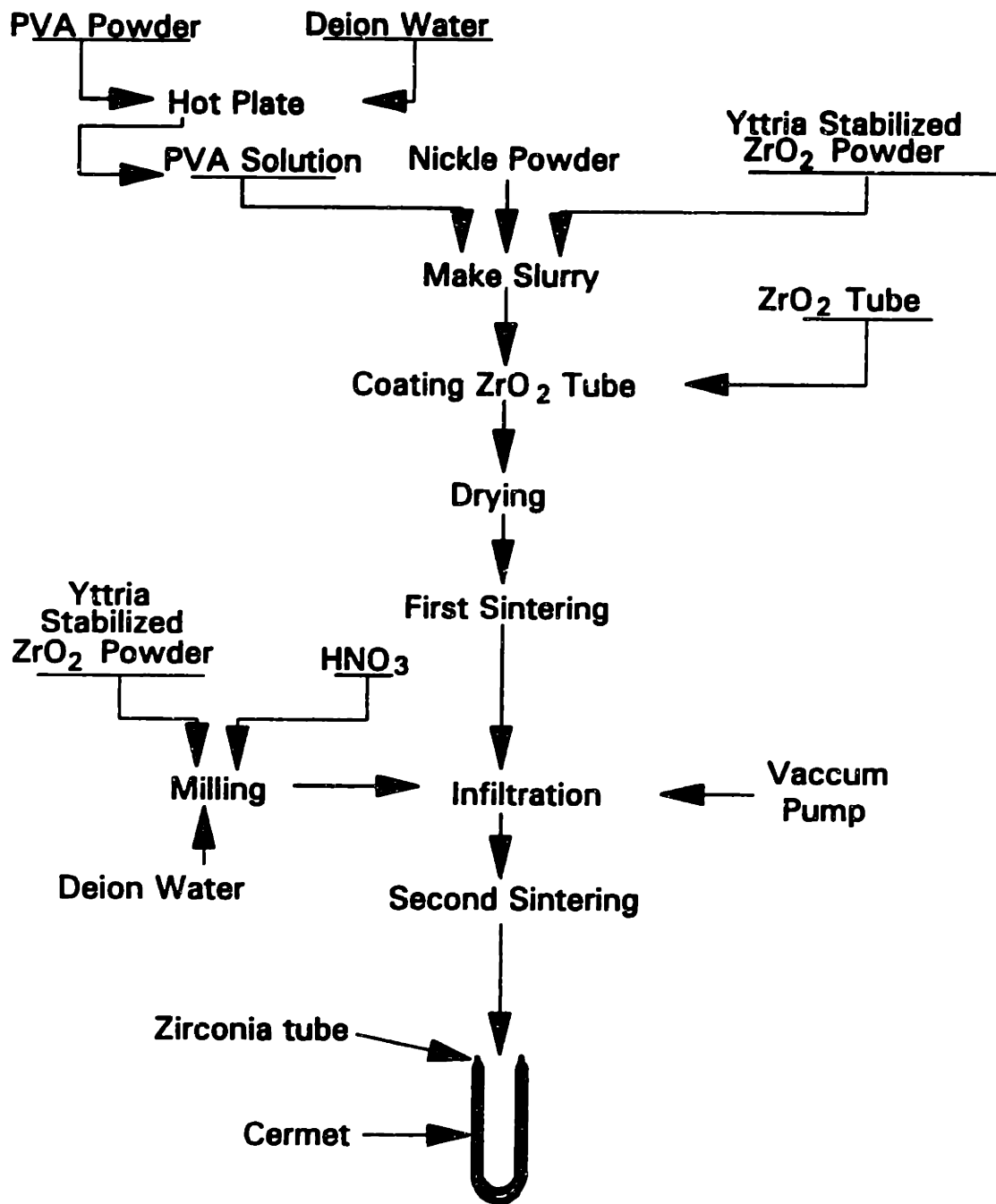
Figure III-2 Flow Chart for the Fabrication of the Ni-ZrO$_2$ Cermet
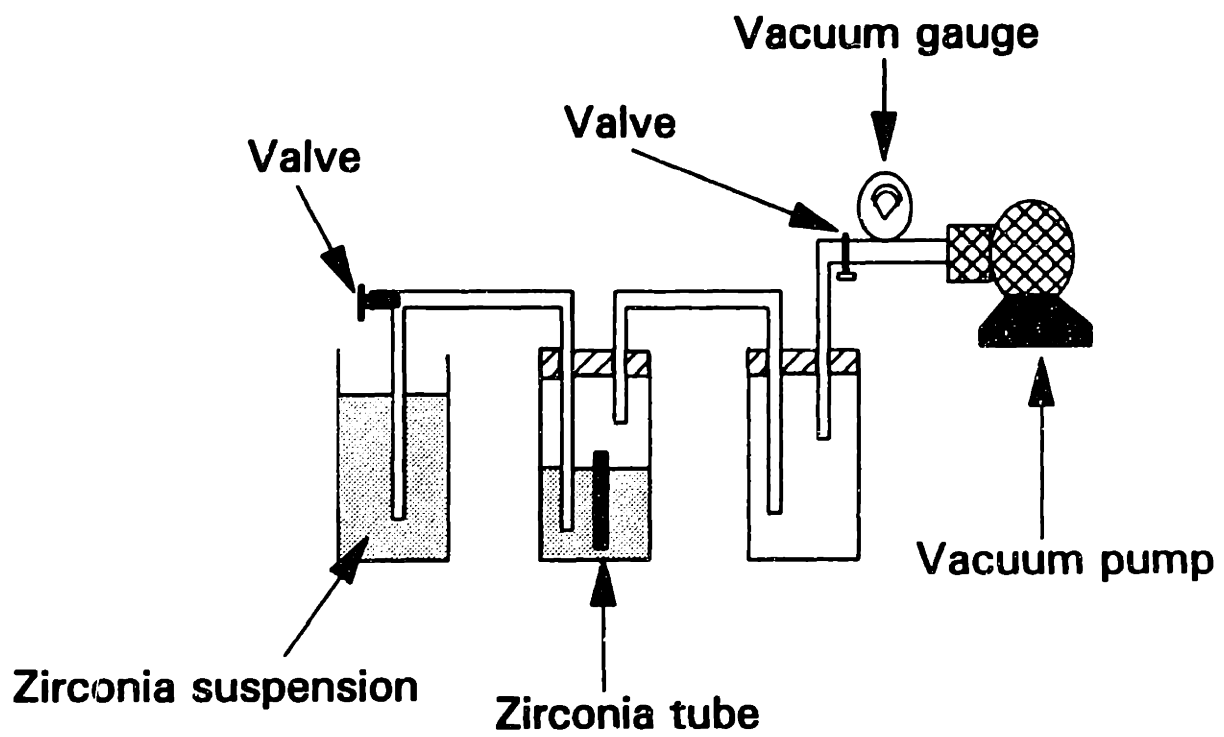
Figure III-3   Schematic of the Set-up for Infiltrating Zirconia Suspension
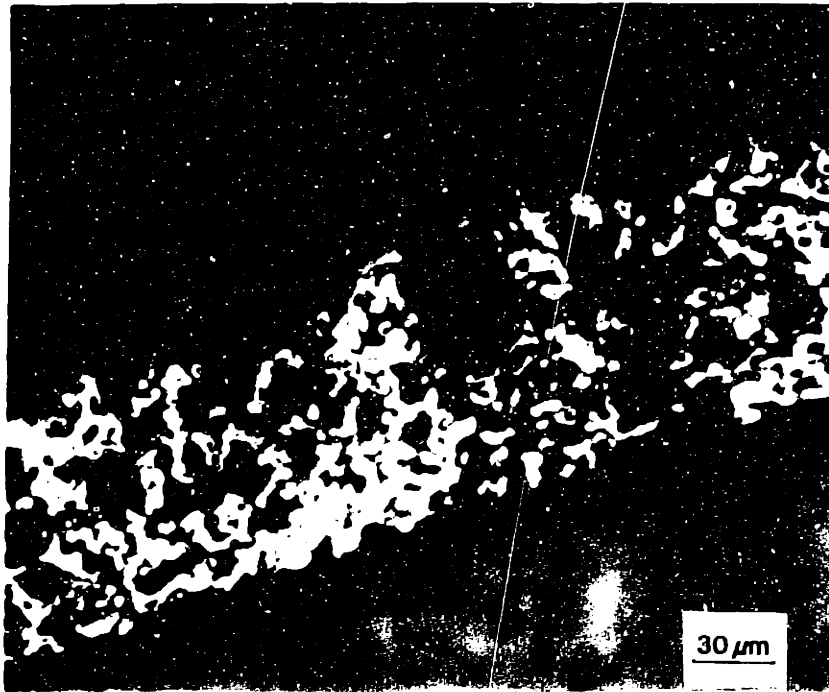
Figure III-4 Optical Micrograph of a Cermet with a Porosity of 36.6%

(The white, gray and dark areas represent the nickel, zirconia and the pore, respectively.)
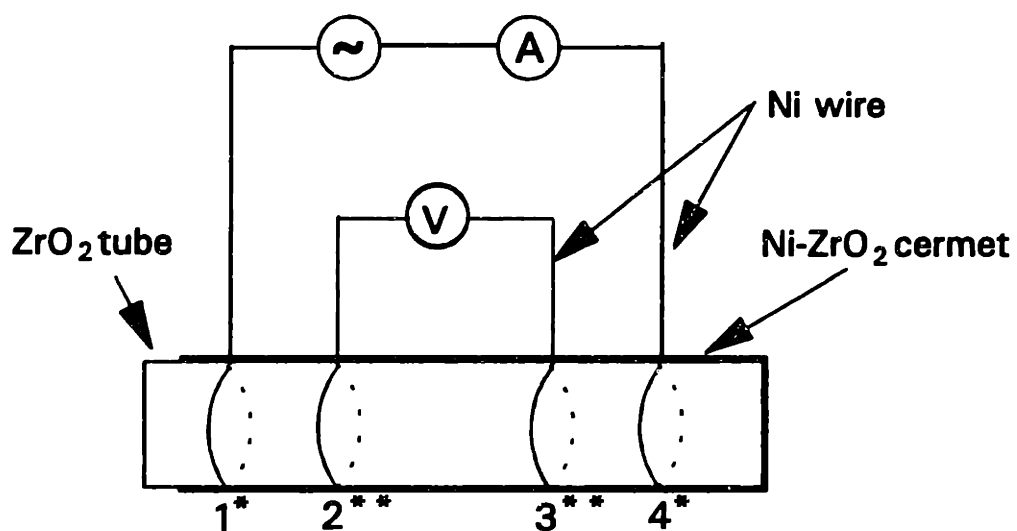
* 1 and 4 are outer terminals connected in series with a power
  supply and an amperemeter
** 2 and 3 are inner terminals connected to a voltmeter

Figure III-5 Schematic of Set-up for Cermet Electrode Sheet Resistance Measurement
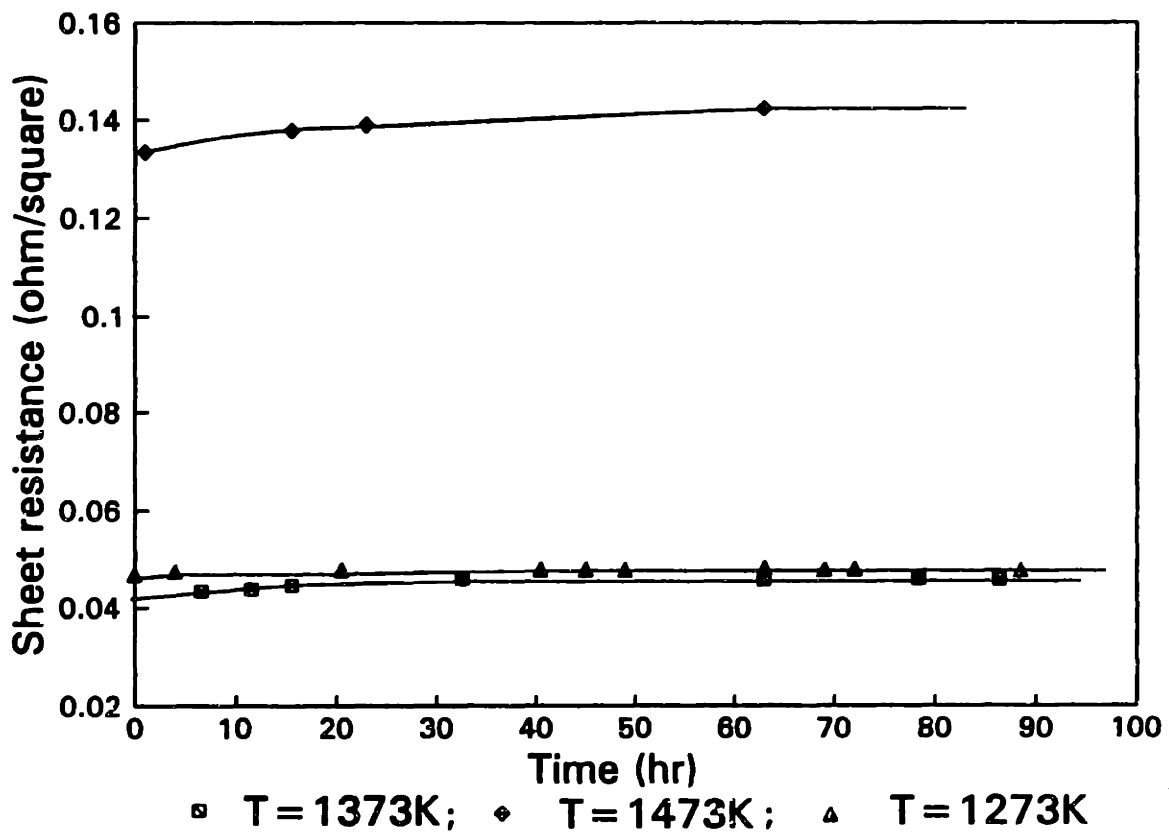
Figure III-6 Variation of Sheet Resistance as a Function of Holding Time

at Different Temperature
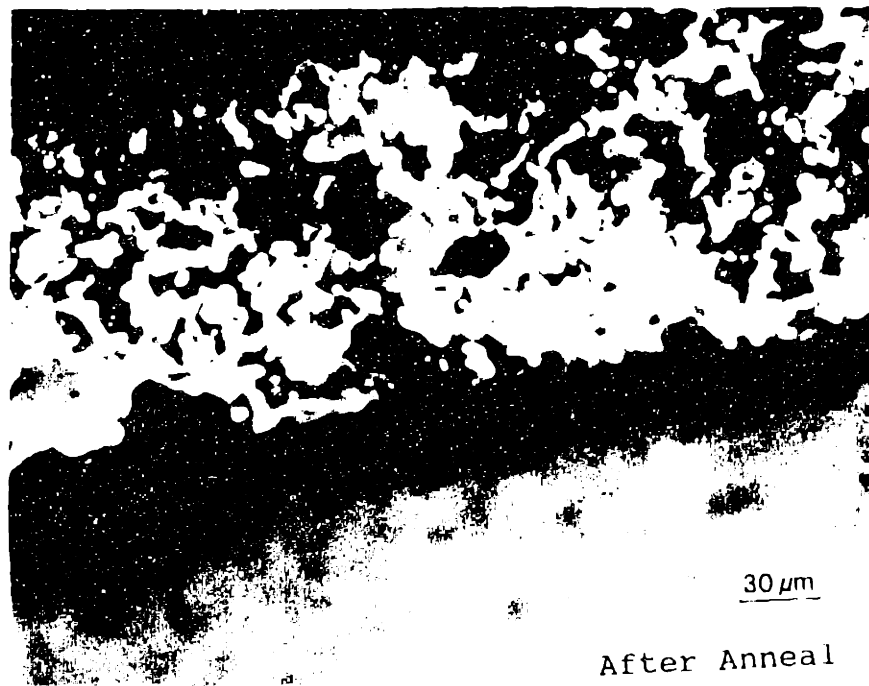
Figure III-7   Optical Micrographs of Cermet Electrode before and after

100 hour anneal at 1373K (The white, gray and the dark areas

represent the nickel, zirconia and the pore, respectively.)

Table III-2   Typical Data on Porosity Measurement

Variables	#1	#2	#3
$W_0^g(g)$	14.0765	11.5322	11.1410
$W_1^g(g)$	14.8085	12.0897	11.5971
$W_2^g(g)$	15.0150	12.1683	11.6707
$W_3^g(g)$	15.3190	12.4874	12.2916
$W_3^l(g)$	12.4010	10.0535	9.5942
Porosity η	36.6%	33.7%	30.4%

* ρ^T = 5.937 g/cm^3 (measured) ρ^Z = 5.600 g/cm^3 (measured)

ρ^J = 0.855 g/cm^3 (measured) ρ^N = 8.910 g/cm^3 (measured)

ρ^L = 1.000 g/cm^3 (measured) ξ = 0.950   (fixed)

IV. EXPERIMENTAL SET-UP AND PROCEDURES

IV.A. Experimental Setup

A schematic of the experimental apparatus is shown in Fig IV-1. Deoxidation experiments were conducted in both SiC heating furnace and induction furnace. For experiments conducted in SiC heating furnace, gas bubbling was used to provide stirring in molten copper, while the induction furnace provided induction stirring. An alumina or quartz crucible containing 0.4-0.7kg of copper (Johnson Matthey) was placed in an alumina furnace tube. The furnace tube was sealed using a water cooled copper plate. The openings on the copper plates were used for argon inlet, argon outlet, electrode lead wire, thermocouple (type S, Pt-10%Rh vs. Pt) positioned in a one end closed alumina tube, Ni/NiO oxygen probe (Leeds and Northrup Corporation), sampling, and the refining device, respectively. The refining devices was fabricated using a one end closed yttria stabilized zirconia tube (1.28cm OD, 0.95cm ID and 8.3 cm long). A porous layer of Ni-ZrO_2 cermet (50-150 μm thick with 30-40% porosity) was deposited along the inner wall of the zirconia tube by a process described in chapter III. Then the yttria stabilized zirconia tube was sealed to an alumina tube with a ceramic adhesive (Ultra-Temp 516, Aremco Products, Inc.). The sealing process involved applying the adhesive, air drying for one or two days, heating for 2.5 hr at 95°C, reapplying the adhesive, and heating for 2.5hr at 95°C and for 1hr at 260°C. A special cement (X-9 Plaster from Crucible Refractory Co.) was also applied to increase the strength of the sealing. Gas tightness of the entire device was examined by using a vacuum pump (Nalgene®, Neward Enterprises). A chromel wire was sintered to the nickel-zirconia cermet and it extended out of the alumina tube to be connected to one of the terminals of a bipolar switch. The other terminal of the switch was connected to another chromel wire which dipped into the copper melt through the argon outlet tube. The bipolar switch was operated either in a short circuit or an open circuit mode. In the short circuit mode, the copper melt was deoxidized and a digital amperemeter was used to record the short-circuit current. In the

open circuit mode a digital voltmeter and DT2811 data acquisition system (Data Translation, Inc.) were used to obtain the equilibrium voltage and the instantaneous open circuit voltage after short-circuiting for a period of time. An oxygen probe (based on Ni/NiO reference with yttria stabilized zirconia electrolyte) was used to check the oxygen concentration in the copper melt. The refining device was flushed inside with either forming gas (95%N_2+5%H_2) or H_2 (AIRCO, Grade 5.0) and dipped in the copper melt. The reducing gas was also passed through an oxygen sensor (ZIRCOA®, type AACC) in order to determine the oxygen partial pressure in the reducing gas. For experiments conducted in SiC heating furnace, the copper melt was homogenized and protected from oxidation by bubbling argon through the melt at a rate of 50ml/min.; the bubbling was conducted either through one or two alumina tubes. For experiments conducted in the induction furnace, argon was blown over the surface of the molten copper.

IV.B. Furnace

SiC heating furnace was a three-zone resistance heating furnace (Lindberg, Model 54459-V). To avoid thermal shock, during experiment, the heating rate was controlled at 3°C/min. The induction furnace used in the experiments was Model W53/10-50 (AJAX Magnethermic Corp.). The cooling system used consisted of a pump and cooling fluid which was a mixture of ethylene glycol and distilled water having a ratio of 2 to 3. Heating Frequency was fixed at 7.4KHz. Because the minimum power output of the furnace was large, the heating rate of copper was quite high, usually 30°C/min in the initial stages of heating. Since alumina crucibles could not endure this thermal shock, quartz crucibles were used. The composition of the quartz crucibles can be found in Appendix II.

Copper shots with 1-10mm diameter were used in the deoxidation experiments. During induction heating, copper shots on the top tended to bridge and stick to the walls of the crucibles. Therefore, around 200g of copper was pre-melted and placed on the top of the copper shots prior to induction heating.

IV.C. Voltage Measurement

Due to the electromagnetic wave that was generated during induction heating, the voltage readings of both the electrolyte cell and thermocouples were affected. Generally, the electrical measurements were recorded by turning the power off. The time during which the power was turned off was short and the fluctuation in the melt temperature was also small. On an average, the difference between voltage readings caused by induction heating was around 0.8mV for the electrolyte cell, and 0.01mV for the thermocouples.

Since a typical electrolyte cell voltage was around 400mV, the voltage change induced by the induction heating was less than 0.5%. Correspondingly the deviation of current readings is also below 0.5%, which was well within the system error and was neglected in the modeling.

The wire used for short circuiting was chromel while the lead of the Ni/NiO probe was molybdenum. When both wires were dipped into molten copper, the thermoelectric power between them was measured to be around 0.0063V at T=1423K, the molybdenum wire being positive. The change of the thermopotential in the experimental temperature range is negligible. The voltage reading of the Ni/NiO probe were corrected accordingly.

IV.D. Temperature Gradient Measurement

Temperature gradient across the electrolyte was measured using the setup shown in Figure IV-2. The results indicate that with a flow rate of 120 ml/min, the temperature difference between Ni-Zirconia cermet and the bulk melt (molten metal) is 2.5-4°C. It is obvious that the temperature difference across the electrolyte will be even smaller than this value.

It is reported that the thermoelectric power, i.e., Seebeck effect, is around 0.02mV/$^\circ$C for $(ZrO_2)_{0.91}(Y_2O_3)_{0.09}$ [76,77]. Given the thermal gradient mentioned above, the effect of thermoelectric power can thus be neglected. .

45

The temperature gradient inside the molten metal was measured for gas bubbling and induction stirring experiments, respectively. In resistance heating furnace, the temperature difference from the bottom to the surface is relatively small, ranging from 2-5°C. In the induction furnace, because only the molten copper is heated, the temperature gradient is much larger, about 5°C/cm. Generally the temperature used in modeling was the average temperature, i.e., the temperature in the middle of the molten copper.

In induction furnace, the temperature gradient above the surface of the molten copper is about 50°C/cm. This temperature gradient has caused zirconia tubes to break. In this study, a stainless steel sheet was used as a cover over the crucible. Holes are drilled on the cover to allow devices and tubes to pass through. This arrangement decreased the temperature gradient above the melt and prevented the device from cracking.

IV.E. Oxygen Concentration Measurement and Atmosphere Control

IV.F.1. Oxygen Partial Pressure Under Open Circuit Condition

Oxygen partial pressure in reducing gas under open circuit condition $-- Po_2{}'(O.C.)$

Oxygen concentration in Cu melt in equilibrium with reducing gas under open circuit condition$-- C_r(O.C.)$

According to Sieverts' law: $\qquad C_r(O.C.) = k_s * \{Po_2{}'(O.C.)\}^{\frac{1}{2}}$

Values of $Po_2{}'(O.C.)$ or $C_r(O.C.)$ were determined using the following three different techniques:

a) An oxygen analysis was conducted on samples taken from the molten copper using fused silica tubes(1/4 inch in diameter, Friedrich & Dimmock) and a vacuum suction technique. Samples, whose weight was between 4g-10g, were analyzed by LECO Corporation using a combustion method. The open circuit voltage were recorded during sampling. The oxygen concentration in the molten copper samples is related to C_r according to the Nernst equation,

$$C_{sample} = C_r \exp(\frac{2E_oF}{RT})$$

where E_0 is the open circuit voltage of the device during sampling.

b) Oxygen partial pressure in the reducing gas is determined by an oxygen sensor at T=1178K, with air as the reference gas. Using the available free energy data as a function of temperature for the reaction:

$$H_2(g) + \frac{1}{2}O_2(g) = H_2O(g)$$
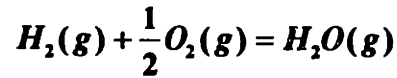
we can calculate the equilibrium constant K_p[78], which is defined as

$$K_p = \frac{P_{H_2O}}{P_{H_2}P_{O_2}^{\frac{1}{2}}}$$

With the knowledge of the hydrogen partial pressure, the partial pressure of water vapor can be calculated as

$$P_{H_2O} = K_p P_{H_2} P_{O_2}^{\frac{1}{2}}$$

This value is around 1% for forming gas (95%N_2+5%H_2) and 0.5% for pure hydrogen. By calculating the shift of chemical equilibrium at experimental temperatures, the oxygen partial pressure $Po_2^r(O.C.)$ can be estimated.

c.) Oxygen probe with Ni/NiO as a reference was also used to monitor the oxygen potential in the copper melt. According to Nernst equation, we have

$$E_{probe} = \frac{RT}{4F} \ln \frac{Po_2(melt)}{Po_2(Ni/NiO)}$$

and

$$E_{device} = \frac{RT}{4F} \ln \frac{Po_2(melt)}{Po_2^r(O.C.)}$$

where $Po_2(Ni/NiO)$ is the equilibrium oxygen partial pressure for the reaction

$$Ni(s) + \frac{1}{2}O_2(g) = NiO(s)$$
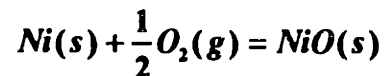
and it can be calculated from the free energy change involved in the reaction[79]. From the readings of the device (E_{device}) and the probe (E_{probe}), $Po_2^r(O.C.)$ can be determined.

The results of these measurements are stated below:

i) When H_2 was used as the reducing gas

$Po_2'(O.C.)$--10^{-17} atm

$C_r(O.C.)$--0.0037ppm @1406K and 0.0052ppm @1442K

ii) When N_2-5%H_2 was as the reducing gas

$Po_2'(O.C.)$--10^{-14} atm

$C_r(O.C.)$--0.14ppm @1406K and 0.2ppm @1442K

A typical worksheet for the calculation of the oxygen partial pressure in reducing gases is shown in Appendix III. As discussed in chapter II, Sieverts' constant k_S which relates $Po_2'(O.C.)$ to $C_r(O.C.)$ can be calculated from the free energy change involved in the reaction[II-3]. This reaction has been studied by many authors[80,81,82,83,84,85,86,87]. In this study, $Po_2'(O.C.)$ and $C_r(O.C.)$ have been measured independently. As shown in the worksheet in Appendix II, the Sieverts' constant k_S estimated from this study is very close to the results reported by Oberg[88].

The oxygen partial pressure in reducing gases sometimes varies, and generally speaking, the variation of the oxygen partial pressure in forming gas(N_2-5%H_2) is much smaller than that in hydrogen. This is probably related to the partial pressure of water vapor in the environment. Because the oxygen partial pressure in hydrogen is much smaller than that in forming gas, it is therefore more sensitive to the environment.

IV.F.2. Gas Flow

The flowrate of gases was controlled by a gas flow meter. Two types of gas flow meters were used. One is mass flow meter/controller (sensor Model FMA-769 and controller model FMA-78P4, calibrated at inlet gas pressure 20 Psi and outlet gas pressure 0 Psi) and the other is rotameter #602(Matheson).

Argon was used to protect the melt from reoxidation. Ar (5.0 grade) was used and its composition is shown in appendix II. A gas train, as shown in Fig. VI-3, was also used to purify the argon. The gas train included a Mg trap (Fisher Scientific) for removing residual oxygen and a glass tube containing Drierite (W.A.Hammond Drierite Co.) for the removal of water vapor.

The oxygen partial in argon was measured by an oxygen sensor to be 9.43×10^{-13} atm at T=1058K. By assuming the water vapor partial pressure to be 10^{-6} atm, the oxygen partial pressure at T=1442K is calculated to be 7×10^{-7} atm. Most of deoxidation experiments were conducted with the oxygen concentration in molten copper to be lower than 300 ppm which corresponds to 10^{-9} atm. Therefore the oxygen introduced into the molten copper by argon is negligible.

Oxygen Sensor

inlet
(H$_2$ or N$_2$-5%H$_2$)

Ampere meter

Alumina tube

Oxygen probe
Thermocouple

Argon inlet

Voltage meter

Water cooling cover

Argon outlet

Furnace tube

Furnace heating bar

ZrO$_2$ electrolyte

Argon bubble

Molten Metal

Crucible

Electrode lead wire
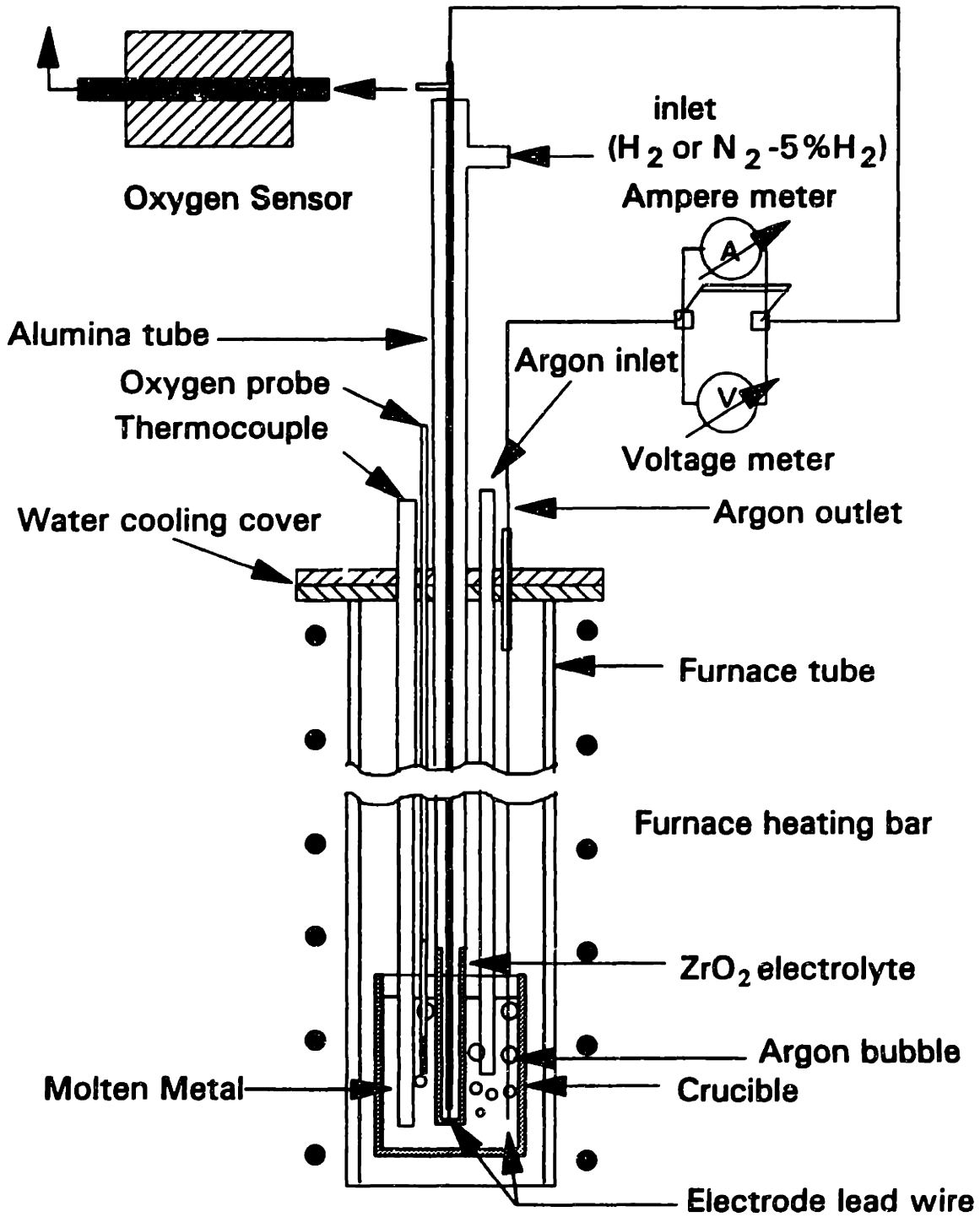
Figure IV-1   Schematic of Experimental Apparatus

Holes for thermocouple wire

outlet

inlet
$(5\%H_2+N_2)$

Holes for outlet gas

Argon inlet

Thermocouple

Water cooling cover

Argon outlet

Furnace heating bar

ZrO_2 electrolyte

Argon bubble

Ni cermet

Thermocouple wire
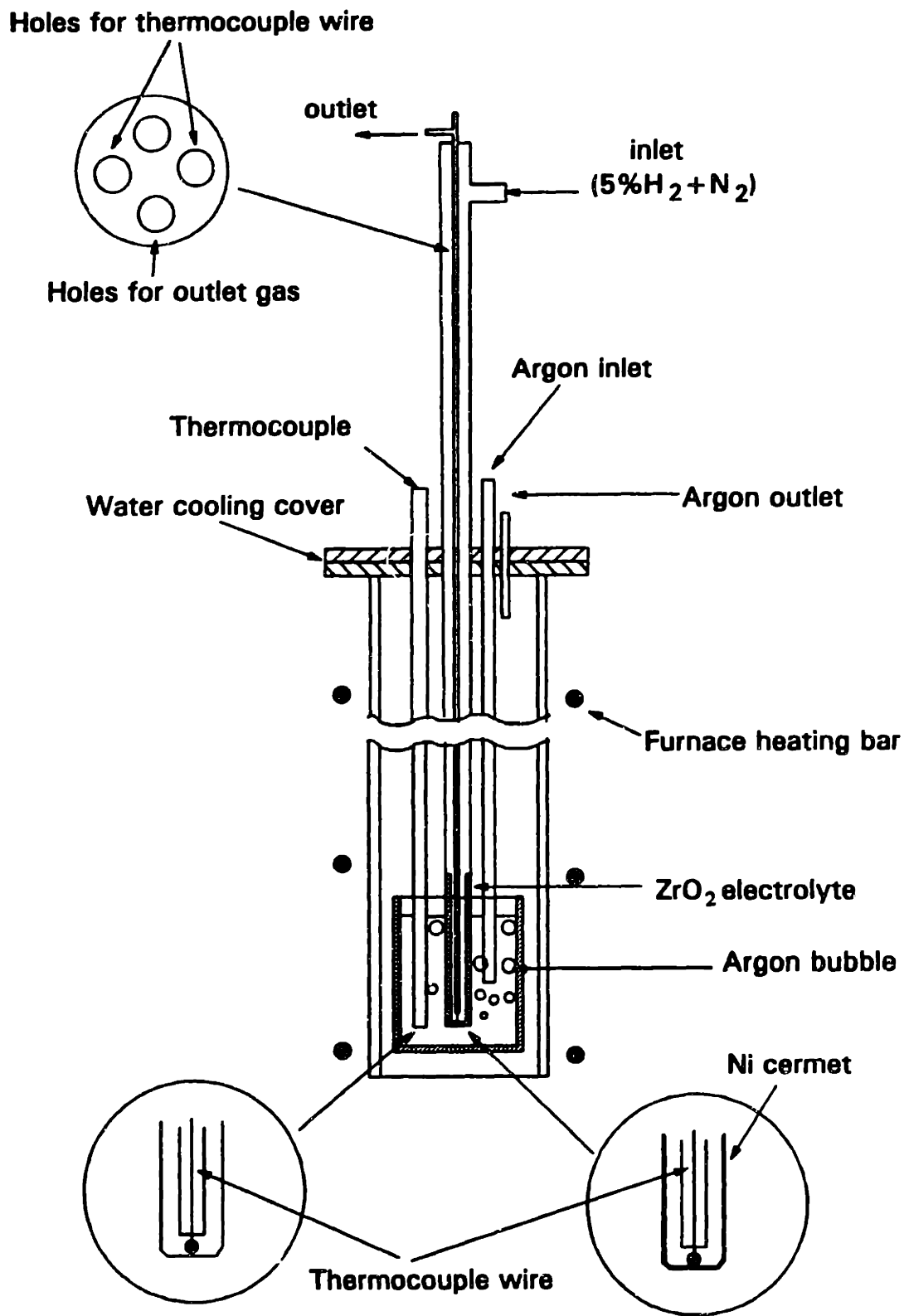
Figure IV-2   Schematic of Set-up for Temperature Gradient Measurement

51
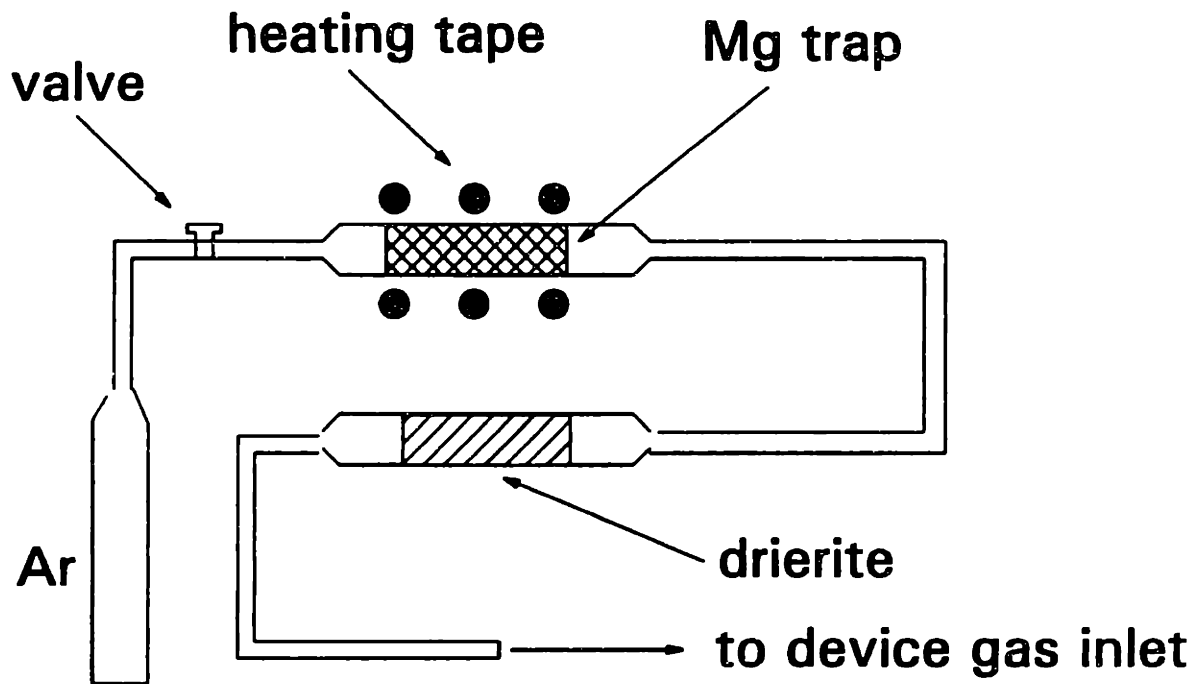
Figure IV-3   Schematic of Gas Train

V. PROCESS OVERVIEW

V.A. Introduction

As shown in Fig. V-1, the steps involved in the deoxidation process include:

1) diffusion of oxygen atoms from the bulk to the melt/electrolyte interface

2) electrode reaction at the melt/electrolyte interface: $\underline{O}(melt) + 2e^- \rightarrow O^{2-}$

3) diffusion of oxygen ions through electrolyte to the electrolyte/reducing gas interface

4) electrode reaction at the electrolyte/reducing gas interface: $O^{2-} \rightarrow 2e^- + \frac{1}{2}O_2(g)$

5) diffusion of oxygen molecules through the porous electrode into the bulk of the reducing gas.

The scheme listed above is just a simplified picture of oxygen transport in the deoxidation process. To provide the readers with a more detailed picture of the deoxidation process, step #1, #2, #4 and #5 are examined in the following part and step #3 is discussed in chapter VI.

V.B. Transport in Molten Copper

Mass transport in liquids includes migration, diffusion and convection: the migration flux involves the transport of charged species through phase under the influence of an electrical field; the diffusion flux is the transport of one species within a phase from one region of higher concentration to another region of lower concentration; the convective flux of the species is produced by macroscopic streams of fluid which carry species toward the transfer plane.

Since the electronic conductivity of molten copper is very high, the electrical field between the short circuit wire and the interface between the electrolyte and the molten copper is negligible. Therefore the migration flux of oxygen is negligible and only diffusion and convective fluxes need to be considered here.

The diffusion process can be described by Fick's first and second laws, i.e.,

$$J_B = -D\nabla_B C \text{ and } \frac{\partial C}{\partial t} = D\nabla_B^2 C$$

where J_B and D_B is the flux and diffusivity of the species B, respectively. The diffusion coefficient of oxygen in molten copper has been surveyed in chapter II.

The convective flux N_B can be expressed as

$$N_B = VC_B$$

where V is the fluid velocity; N_B and C_B are the flux and concentration of species B, respectively. Since the fluid velocity is unknown in most cases, this formula is only used in well defined system. Generally a system undergoing convectiv mass transfer is described using the concept of diffusion layer[89], which was first brought into the realm of process metallurgy by Herty [90] and later revived by Wagner [91]. The key idea is to divide the solution into two parts: a thin layer, called diffusion layer or boundary layer, near the electrode with no convection, and the bulk solution where the stirring ensures an uniform concentration. If the thickness of the diffusion layer is δ, Fick's first law can be expressed as

$$J = -D\frac{\partial C}{\partial x} = -\alpha \cdot \Delta C$$

where α is called mass transfer coefficient. In this study, this expression is used since forced convection has been provided by gas bubbling or induction stirring in molten metals, and therefore the assumption stated above is believed to be satisfied.

V.C. Electrode Kinetics

Both step #2 and #4 involve electron transfer reactions. The reactions stated in those steps are just phenomenological descriptions. It is believed that those electrode reactions actually consist of many steps. For example, step 2 is believed to include at least the following two reactions:

a) the adsorption of dissolved oxygen in molten metals on the surface of electrolytes

$$\underline{O} \rightarrow O_{ads}$$
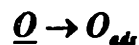
and an electrochemical reduction

$$O_{ads} + 2e^- + V_O^{\cdot\cdot} \rightarrow O_O^x$$
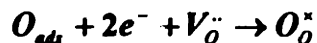
Similarly, it is believed that step #4 also includes an electrochemical oxidation reaction and a desorption process. Though there have been many reports on the study of electrode kinetics on solid electrolytes[92,93,94,95], most of them are phenomenological and the exact mechanism remains unknown. Most of those studies focus on electrode reactions at the interface between gases and electrolytes, whereas only a few describe electrode reactions at the interface between molten metals and electrolytes. Detailed discussion about this topic can be found in [96]

$$i = i_o [e^{-\alpha n f \eta} - e^{(1-\alpha)n f \eta}]$$

where i is the current density through the electrode, i_0 is the exchange current density, η =$E-E_{eq}$, f=F/RT, and α is electron transfer coefficient.

For large values of η (either negative or positive), one of the two terms in the above equation becomes negligible. For example, at large negative η, the above equation becomes

$$i = i_o e^{-\alpha n f \eta}$$

This is generally referred to as the Tafel equation. It has been reported that hydrogen oxidation reaction at the Ni/zirconia electrode satisfies this equation[97,98], and the exchange current density has a strong dependency on oxygen partial pressure in the reducing gases, ranging from 17.8mA/cm^2 to 118mA/cm^2. The current density i in this study is around 20mA/cm^2. Therefore it is reasonable to consider the overpotential at these electrodes to be negligible.

V.D. Diffusion in Gases

As described before, in a typical deoxidation experiment, a reducing gas is flushed into a yttria stabilized zirconia tube. As shown in Fig. IV-1, the reducing gas is preheated as it flows through the alumina tube and reaches the Ni-zirconia cermet which has been deposited on the inner wall of the zirconia tube. Under short circuit condition, hydrogen is consumed and water vapor is formed. Therefore, it is expected that there will be both

temperature and concentration gradients in the device, and therefore four types of fluxes can be envisaged: 1) mass flux due to concentration gradient (ordinary diffusion), 2) energy flux due to the temperature gradient (thermal diffusion), 3) mass flux due to the temperature gradient (thermal diffusion known as the Soret effect), and 4) energy flux due to the concentration gradient (known as the Dufour effect). These effects can be described by irreversible thermodynamics founded by Onsager[99,100,101]. Here only ordinary diffusion will be discussed. The other three types of diffusion is expected to be much smaller than the flux of the ordinary diffusion.

According to the relative magnitude of the mean free path and the size of pore, gas diffusion in a porous media can be divided into two types, i.e., knudsen diffusion and molecular diffusion. When the pore size is much larger than that of the mean free path of molecules, it is molecular diffusion and diffusion occurs via collision between the molecules. When the pore size is close to that of the mean free path of molecules, the molecules collide with the pore wall much more frequently than with each other and it is knudsen diffusion. For molecular diffusion, the diffusivity is inversely proportional to pressure while Knudsen diffusivity is independent of pressure. Therefore, in any porous medium, Knudsen diffusion predominates at low pressures where the mean free path is much larger than the dimension of the pores.

Transport properties of gases can be calculated utilizing kinetic theory of gases, known as the Chapman-Enskog theory[102,10?]. In discussing capillary or pore diffusion, it is more convenient to adopt a simpler form of the kinetic theory of gases, which is based on the assumptions that (i) the molecules are non-reacting rigid spheres, (ii) all the spheres move at the same speed, and (iii) equal number of molecules travel parallel to each of the three coordinates. From this theory, the self-diffusivity is given by [104]

$$D = \frac{1}{3}\bar{v}l$$

where D is the diffusivity of gases, $\bar{v}$ is the mean thermal molecular velocity, equal to $\dfrac{8kT}{(\pi m)^{\frac{1}{2}}}$, and l is the mean free path of molecules which can be calculated as

$$l = \frac{1}{\sqrt{2}\,n\pi\delta^2}$$

where n is the number of molecules per unit volume and δ is the diameter of the rigid spheres.

For Knudsen diffusion, Knudsen[105] has shown that the flux involving collision of molecules and reflection from the surface of the capillary wall is represented by the equation

$$J = -\frac{2}{3}\bar{v}r\frac{dc}{dz}$$

where r is the radius of the capillary tube and dc/dz is the concentration gradient along the capillary. The coefficient known as the Knudsen diffusivity is

$$D_K = \frac{2}{3}\bar{v}r = 9.7 \times 10^3\, r(\frac{T}{M})^{\frac{1}{2}}$$

where r is in units of centimeters and D_K is in square centimeters per second.

It has been reported[106] that δ is 2.968Å for H_2 and 3.433Å for O_2. Based on the previous discussion, it can be calculated that, at 1400K and one atmosphere, the mean free path l is around 0.5μm. This is much smaller than the dimension of macro pores, whose size is estimated to be around 10μm from micrographs. Therefore diffusion in cermet will predominentely be molecular diffusion instead of Knudsen diffusion, though in some small pores, the diffusion can be mixed control. Based on this consideration, it can be calculated that the concentration gradient of water vapor pressure is very small when the current density is around 20mA/cm^2. Because the ratio of H_2/H_2O fixes the oxygen partial pressure in the reducing gas, this small gradient also means that the concentration polarization at the anode will be small.

V.E. Effect of Capacitance at Electrodes and Other Factors

The capacitance at the interface between the electrolyte and electrodes has been studied by many authors. The value of the capacitance is a function of the electrode deposition process parameters and ranges from 10 to 100 $\mu F/cm^2$[107,108,109,110,111]. Theoretical estimation gives a value of 10 to 30 $\mu F/cm^2$[112,113]. The deoxidation process is mainly Faradic in nature since the discharge time of the capacitor is on the order of RC. Therefore the effect of non-Faraday process on the overall deoxidation process is negligible.

V.F. Rate-Controlling Steps

Based on the previous discussion, it can be concluded that step #2 and #5 will be not be rate limiting. This is also consistent with the report on SOFC performance[114], where the electrode reactions and gas phase diffusion in solid oxide fuel cells (SOFCs) operating at 1273K are observed to be very rapid and the overpotential due to them is very small. Though the exchange current density data for the step #3 is currently unavailable, it has been reported[115] to be very fast. Under our experimental conditions, the operating temperature is higher than that of SOFCs and the current density is relatively small (0.5-25 mA/cm^2). Therefore it is reasonable to consider oxygen ion diffusion in the electrolyte (step #3) and oxygen atom diffusion in the melt (step #2) to be much slower than the other steps and are therefore rate-controlling.

electrode   boundary layer

R_{ex} e^-

reducing gas

melt Q

① Q

e

② $Q = O^{2-} - 2e^-$

③ O^{2-}

④ $O^{2-} = 1/2 O_2 (g) + 2e^-$

⑤

$O_2 (g)$

forced convection

YSZ

C_r C_i C_b
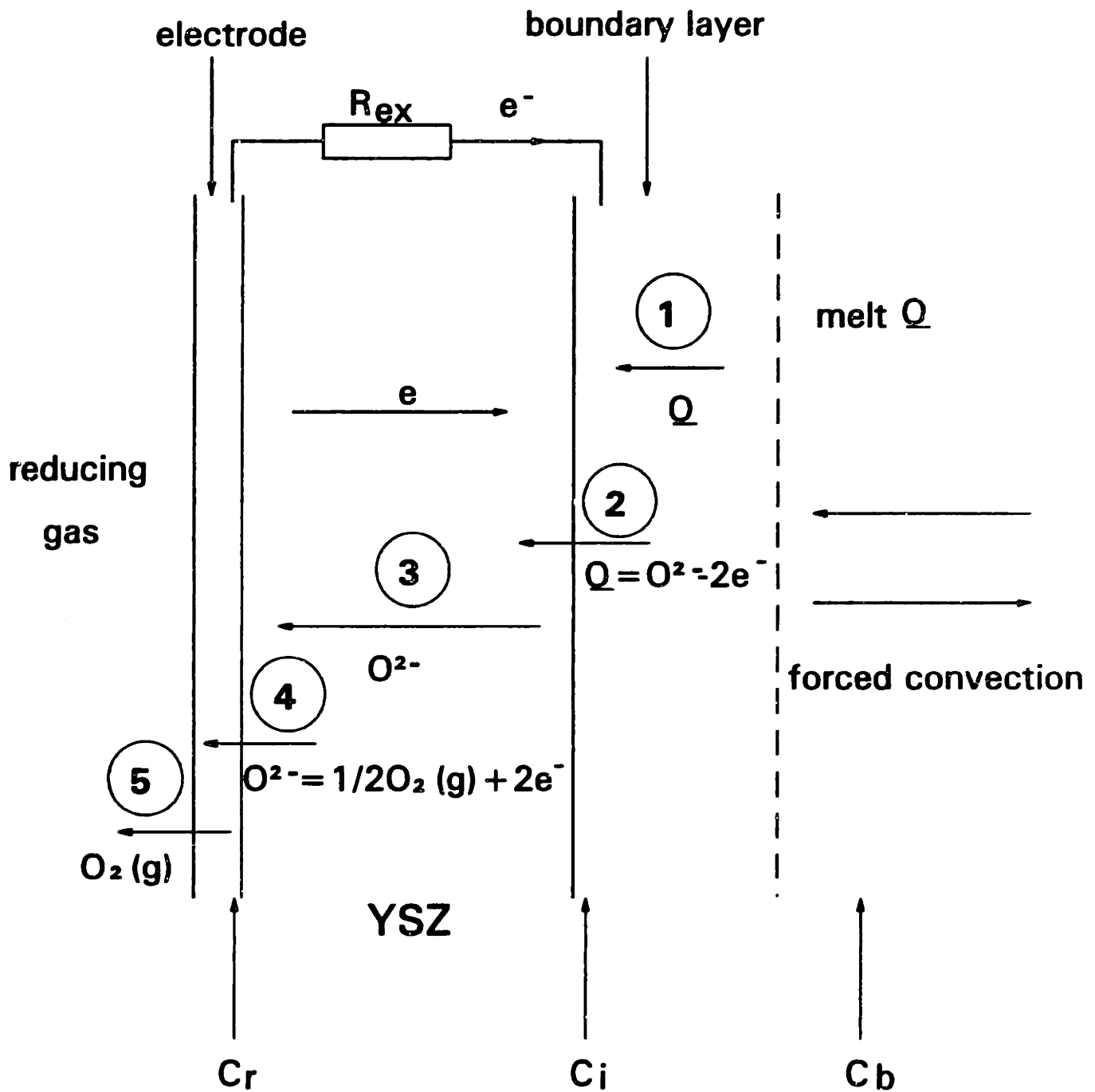
Figure V-1 Illustration of Steps Involved in the Deoxidation Process

VI. TRANSPORT THEORY OF SOLID OXIDE ELECTROLYTE

VI.A. Introduction

The transport of ions in solid matter, especially in metal oxides and sulfides, plays an important role in determining the kinetics of many reactions at elevated temperatures, such as the oxidation and sulfidation of metals, the sintering of ceramics, spinel formation, etc. Since C. Wagner's work in 1933 [116], there have been many papers on the transport of ions in electrolytes due to chemical gradient[117], stress field[118] and a combination of chemical gradient and electrical field[119]. A comprehensive treatment of this topic can be found in the literature[120]. However, these studies have been pursued from the viewpoint of metal oxidation and sulfidation, e.g., one of most studied topic is the tarnishing of metals. Therefore, these investigations considered the transport phenomena in electrolytes without an external load. With the increasing use of solid electrolytes in batteries and fuel cells, the transport of ions in electrolytes with external load needs to be analyzed in detail. Several papers have tried to discuss this issue, and in their analysis [121,122,123,124,125] an equivalent circuit as shown in Fig. VI-1 has been used. The idea of the equivalent circuit can be traced back to Jost[126] and Hoar[127]. A description of this equivalent circuit was presented in a systematic survey provided by Schmalzeried [128] in 1982. In that paper limiting cases of the equivalent circuit were also discussed to show its main characteristics. Similar transport analysis without the use of the equivalent circuit was carried out by Tannhauser[129]. Without obtaining an explicit expression of the ionic current, he discussed the current efficiency of electrolyte cells and compared the results with that obtained from the equivalent circuit.

In the following part, a general formula is obtained for the ionic current in electrolytes under an external load. Based on this general formula, the effectiveness of the equivalent circuit is discussed and equations derived without considering external load is

60

obtained as the limiting cases of the general formula. This general formula will also be simplified to analyze our deoxidation process in chapter VII.

VI.B. Transport Theory

The transport theory of electrolytes is based on irreversible thermodynamics[130,131] and defect chemistry[132]. Before the derivation, it is worth reviewing some basic transport equations. The Nernst-Einstein equation[133] relates the diffusion coefficient of conducting species i to its mobility via

$$D_i = B_i kT \qquad \text{[VI-1]}$$

where D_i is the diffusion coefficient of species i; B_i is the absolute mobility of species i and is defined as

$$-B_i = \frac{velocity}{force} \qquad \text{[VI-2]}$$

Electrical conductivity of species i, σ_i, is related to D_i by

$$\sigma_i = \frac{(Z_i e)^2 C_i D_i}{kT} \qquad \text{[VI-3]}$$

where Z_i and C_i are the charge and the concentration of the species i, respectively. e, k and T have their ordinary meanings.

According to irreversible thermodynamics[134,135], fluxes have a linear relationship with driving forces and this relationship can be expressed as

$$\bar{J}_i = \sum_{k=1}^{n} L_{ik} \nabla \Gamma_k$$

where $\bar{J}_i$ is the flux of species i; $\nabla \Gamma_k$ is the kth driving force. It has been proven by Onsager that the transport coefficient matrix L is symmetric, i.e., for all i≠j, cross coefficient $L_{ij}=L_{ji}$.

For a system with an unidirectional diffusion of two species, the above formula can be written as

$$\begin{pmatrix} \bar{J}_1 \\ \bar{J}_2 \end{pmatrix} = \begin{pmatrix} L_{11} & L_{12} \\ L_{21} & L_{22} \end{pmatrix} \begin{pmatrix} \dfrac{\partial \eta_1}{\partial x} \\ \dfrac{\partial \eta_2}{\partial x} \end{pmatrix}$$

and

$$\eta_i = \mu_i + Z_i F \varphi \qquad \text{[VI-4]}$$

where η_i is the electrochemical potential of species i,

μ_i is the chemical potential of species i,

Z_i is the valence charge of species i,

F is Faraday constant, and

φ is electrical potential in the system, and

$L_{21} = L_{12}$.

Here the flux of ions due to thermal gradient is neglected and only the driving force from electrical field and chemical potential gradient are considered.

Generally, in solid electrolyte transport theory, cross coefficients L_{12} and L_{21} are assumed to be zero. It is worth mentioning that many important transport-related theories and relationships rely on the assumption that $L_{12} = L_{21}$. For example, by using this condition implicitly, Wagner [136] derived the following equation in 1933.

$$E_{mea} = \frac{1}{4F} \int_{\mu'_{O_2}}^{\mu''_{O_2}} t_{ion} d\mu_{O_2}$$

where E_{mea} is the voltage measured across the electrolyte. Though there have been a few papers [137,138] reporting the values of cross coefficients, research on this topic is limited. In 1975, Wagner [139] discussed the situations in which the cross coefficients ought to be taken into account when treating transport problems in oxide systems. In that paper, he pointed out that, in compounds with prevailing ionic conduction, $L_{12} << L_{22}$, L_{11}. Therefore it is acceptable to assume $L_{21} = L_{12} = 0$.

Based on the preceding discussion, we have

$$\bar{J}_i = L_{ii} \frac{\partial \eta_i}{\partial x}$$

$$= L_{ii} \left(\frac{\partial \mu_i}{\partial x} + z_i F \frac{\partial \Phi}{\partial x} \right) \qquad \text{[VI-5]}$$

When $\dfrac{\partial \mu_i}{\partial x} = 0$, we have

$$\bar{J}_i = L_{ii} z_i F \frac{\partial \Phi}{\partial x}$$ [VI-6]

Compared with Ohm Law,

$$\bar{J}_i = -\frac{\sigma_i}{z_i F} \frac{\partial \Phi}{\partial x}$$ [VI-7]

where $\bar{J}_i$ is mol/cm^2-s. Combining eq.[VI-6] and [VI-7] gives

$$L_{ii} = -\frac{\sigma_i}{z_i^2 F^2}$$ [VI-8]

Therefore eq.[VI-5] becomes

$$\bar{J}_i = -\frac{\sigma_i}{z_i^2 F^2} \frac{\partial \mu_i}{\partial x} - \frac{\sigma_i}{\dfrac{z_i^2}{z_i} F} \frac{\partial \Phi}{\partial x}$$ [VI-9]

If the flux is expressed in equi./cm^2-s,

$$J_i = -\frac{\sigma_i}{\dfrac{z_i^2}{|z_j|} F^2} \frac{\partial \mu_j}{\partial x} - \frac{\sigma_i}{\dfrac{z_i^2}{z_i|z_j|} F} \frac{\partial \Phi}{\partial x}$$ [VI-10]

For oxygen ion conductor, such as zirconia and ceria, only the fluxes of oxygen ions and electrons need to be considered, as shown in Fig. VI-2. Since $z_{O^{2-}} = -2$ and $z_e = -1$, we have

$$J_{O^{2-}} = -\frac{\sigma_{O^{2-}}}{2F^2} \frac{\partial \mu_{O^{2-}}}{\partial x} + \frac{\sigma_{O^{2-}}}{F} \frac{\partial \varphi}{\partial x}$$ [VI-11]

$$J_e = -\frac{\sigma_e}{F^2} \frac{\partial \mu_e}{\partial x} + \frac{\sigma_e}{F} \frac{\partial \varphi}{\partial x}$$ [VI-12]

where $J_{O^{2-}}$ and J_e are the flux of oxygen ions and electrons in the electrolyte, respectively. The directions of the fluxes in the Fig. VI-2 are assigned according to the sign of the fluxes in the above equations, not necessarily their real directions. φ is the electrical potential in the electrolyte. $\mu_{O^{2-}}$ and μ_e are the chemical potential of oxygen ions and electrons, and $\sigma_{O^{2-}}$ and σ_e are the ionic and electronic conductivities of the electrolyte, respectively.

The charge conservation demands

63

$$J_e + J_{O^{2-}} = \frac{I_{ex}}{FA} \qquad \text{[VI-13]}$$

Here I_{ex} is the external current; F is the faraday constant; A is the area of the electrolyte through which the flux flows.

Generally it can be assumed that electrodes on the surface of electrolytes are reversible and the electrons in both the electrolyte and the electrodes are in equilibrium. Therefore

$$\mu(e)'_{electrode} - F\varphi(e)'_{electrode} = \mu(e)'_{electrolyte} - F\varphi(e)'_{electrolyte} = \eta' \qquad \text{[VI-14]}$$

$$\mu(e)''_{electrode} - F\varphi(e)''_{electrode} = \mu(e)''_{electrolyte} - F\varphi(e)''_{electrolyte} = \eta'' \qquad \text{[VI-15]}$$

A detailed discussion about reversible and non-reversible electrodes can be found in the literature[140,141].

Since $\mu(e)'_{electrode} = \mu(e)''_{electrode}$, subtracting eq.[VI-14] from eq.[VI-15] gives

$$E_e = \varphi'_{electrode} - \varphi''_{electrode}$$

$$= \frac{\eta'' - \eta'}{F}$$

and

$$I_{ex} = \frac{E_e}{R_{ex}}$$

$$= \frac{\eta'' - \eta'}{FR_{ex}} \qquad \text{[VI-16]}$$

Because

$$O^{2-} = O + 2e \qquad \text{[VI-17]}$$

correspondingly we have

$$\mu_{O^{2-}} = \mu_O + 2\mu_e \qquad \text{[VI-18]}$$

where μ_O is the chemical potential of oxygen atoms in the electrolyte.

Combining eqs. [VI-11], [VI-14] and [VI-18] to eliminate μ_e and φ gives

$$J_{O^{2-}} = -\frac{\sigma_{O^{2-}}}{2F^2}\frac{\partial\mu_O}{\partial x} - \frac{\sigma_{O^{2-}}}{F^2}\frac{\partial\eta}{\partial x} \qquad \text{[VI-19]}$$

while combining eqs. [VI-12] and [VI-14] gives

$$J_e = -\frac{\sigma_e}{F^2}\frac{\partial \eta}{\partial x}$$ [VI-20]

Since

$$O = \frac{1}{2}O_2(g)$$ [VI-21]

we have

$$\mu_O = \frac{1}{2}\mu_{O_2} = \frac{1}{2}(\mu_{O_2}^o + RT \ln P_{O_2})$$ [VI-22]

The integration of eq.[VI-19] gives

$$J_{O^{2-}} d = \frac{RT\sigma_{O^{2-}}}{4F^2}\ln\frac{P_{O_2}^I}{P_{O_2}^{II}} - \frac{\sigma_{O^{2-}}}{F^2}(\eta^{II} - \eta^I)$$ [VI-23]

where $P_{O_2}^I$ and $P_{O_2}^{II}$ are the oxygen partial pressure of gases in contact with each side of the electrolyte, as shown in Fig. VI-2.

From eqs. [VI-19] and [VI-20], we have

$$\frac{J_{O^{2-}}}{\sigma_{O^{2-}}} - \frac{J_e}{\sigma_e} = -\frac{1}{2F^2}\frac{\partial \mu_O}{\partial x}$$ [VI-24]

Combining eqs. [VI-13], [VI-16], and [VI-24] gives

$$J_{O^{2-}} = \frac{(\eta^{II} - \eta^I)\sigma_{O^{2-}}}{F^2 AR_\alpha(\sigma_{O^{2-}} + \sigma_e)} - \frac{1}{2F^2}\frac{\sigma_e\sigma_{O^{2-}}}{\sigma_{O^{2-}} + \sigma_e}\frac{\partial \mu_O}{\partial x}$$ [VI-25]

Combining eqs. [VI-23] and [VI-25] by eliminating η, we have

$$J_{O^{2-}} = \frac{1}{\{1 + \frac{d}{R_\alpha A(\sigma_{O^{2-}} + \sigma_e)}\}}\{\frac{\sigma_{O^{2-}}}{4F^2 R_\alpha A(\sigma_{O^{2-}} + \sigma_e)} \cdot RT \ln\frac{P_{O_2}^I}{P_{O_2}^{II}} - \frac{1}{2F^2}\frac{\sigma_e\sigma_{O^{2-}}}{\sigma_{O^{2-}} + \sigma_e}\frac{\partial \mu_O}{\partial x}\}$$

[VI-26]

This is a general formula describing the flux of ions through the electrolyte. To obtain a specific expression for the ionic flux, it is necessary to know the distribution of oxygen partial pressure in the electrolyte as well as the variation of electronic conductivity with the oxygen partial pressure. Then the oxygen flux can be calculated.

For most ionic conductors,

$$\sigma_e \ll \sigma_{O^{2-}}$$

. Therefore as a first-order approximation,

$$\sigma_e + \sigma_{O^{2-}} \approx \sigma_{O^{2-}} \qquad [VI-27]$$

Utilizing eq. [VI-27], eq.[VI-26] can be simplified as

$$J_{O^{2-}} = \frac{R_{ex}}{R_{ex} + R_{ion}} \{ \frac{RT}{4F^2 R_{ex} A} \ln \frac{P'_{O_2}}{P''_{O_2}} - \frac{1}{2F^2} \sigma_e \frac{\partial \mu_O}{\partial x} \} \qquad [VI-28]$$

where R_{ion} is the ionic resistance of the electrolyte, and is defined as

$$R_{ion} = \frac{d}{\sigma_{O^{2-}} A}. \qquad [VI-29]$$

As discussed in chapter II, the electronic conductivity in zirconia is related to the oxygen partial pressure [142,143,144] by

$$\sigma_e = \sigma_e^o P_{O_2}^{-\frac{1}{4}} \qquad [VI-30]$$

By substituting this expression for electronic conductivity in eq.[VI-28] and integrating it, the ionic current through the electrolyte, I_{ion}, can be written as:

$$I_{ion} = FAJ_{O^{2-}} = \frac{RT}{4F(R_{ex} + R_{ion})} \ln \frac{P'_{O_2}}{P''_{O_2}} + \frac{RTAR_{ex}}{(R_{ex} + R_{ion})Fd} \{ \sigma_e^o (P''_{O_2})^{-\frac{1}{4}} - \sigma_e^o (P'_{O_2})^{-\frac{1}{4}} \}$$

$$[VI-31]$$

This formula is the expression of ionic flux through electrolytes with external load and electronic conductivity under the constraints of eq.[VI-27] and [VI-30]. For different electrolytes, the relationship between the electronic conductivity and the oxygen partial pressure can be different, and based on that, appropriate expressions can be derived.

VI.C. Discussion of Results

VI.C.1 With external load and negligible electronic conductivity

When electronic conductivity is small either due to a small σ_e^o or high P_{O_2}, the second term in eq.[VI-31] becomes much smaller than the first term, and eq.[VI-31] can be simplified as

$$I_{ion} = \frac{RT}{4F(R_{ex} + R_{ion})} \ln \frac{P_{O_2}^I}{P_{O_2}^{II}} \qquad [\text{VI-32}]$$

This is consistent with the result from the equivalent circuit as shown in Fig. VI-1, where

$$I_{ion} = \frac{E_{th}}{R_{ex} + R_{ion}} \qquad [\text{VI-33}]$$

and

$$E_{th} = \frac{RT}{4F} \ln \frac{P_{O_2}^I}{P_{O_2}^{II}} \qquad [\text{VI-34}]$$

Based on the discussion on the electrical properties of yttria stabilized zirconia in chapter II, it can be shown that eq.[VI-32] is true when forming gas ($P_{O_2} \approx 10^{-14}$ atm) is used in this study.

VI.C.2 Without external load but with appreciable electronic conductivity

Under open circuit conditions, $R_{ex} = \infty$ and eq.[VI-26] gives

$$J_{O^{2-}} = -\frac{1}{2F^2} \frac{\sigma_e \sigma_{O^{2-}}}{\sigma_{O^{2-}} + \sigma_e} \frac{\partial \mu_O}{\partial x} \qquad [\text{VI-35}]$$

Utilizing eq.[VI-22] and [VI-30], eq.[VI-35] can be integrated as

$$J_{O^{2-}} = \frac{RT}{F^2 d} \{ \sigma_e^o (P_{O_2}^{II})^{-\frac{1}{4}} - \sigma_e^o (P_{O_2}^I)^{-\frac{1}{4}} \} \qquad [\text{VI-36}]$$

Eq.[VI-36] has been verified in [145].

It is worth mentioning that, though eq.[VI-36] can also be obtained by substituting $R_{ex} = \infty$ in eq. [VI-31], it is not restrained by the condition in eq.[VI-27] as eq. [VI-31] does.

VI.C.3. With external load and appreciable electronic conductivity

If it is assumed that $\overline{\sigma_e}$ is the average value of the electronic conductivity of the electrolyte and that $\overline{\sigma_e}$ does not change throughout the electrolyte, by defining

$$\overline{R_e} = \frac{d}{\overline{\sigma_e} A} \qquad [\text{VI-37}]$$

eq.[VI-26] can be simplified as

$$I_{ion} = \frac{R_{ex} + \overline{R_e}}{\overline{R_e} R_{ex} + R_{ex} R_{ion} + \overline{R_e} R_{ion}} \frac{RT}{4F} \ln \frac{P_{O_2}^I}{P_{O_2}^{II}} \qquad [\text{VI-38}]$$

Eq.[VI-38] has been presented in [146] and used in [147,148]. A similar equation expressing transference number is also reported in the literature[149].

Since eq.[VI-38] can be a convenient tool for analyzing the oxygen transport in electrolytes with external load and electronic conductivity, it is worthwhile to compare the difference between eq.[VI-38] and eq.[VI-31]. By equating eq.[VI-38] and eq.[VI-31], the equivalent $\overline{R_e}$ can be obtained as

$$\overline{R_e} = \frac{\dfrac{d \ln \dfrac{P_{O_2}^I}{P_{O_2}^{II}}}{4A\{\sigma_e^o (P_{O_2}^{II})^{-\frac{1}{4}} - \sigma_e^o (P_{O_2}^I)^{-\frac{1}{4}}\}} - R_{ion}}{1 + \dfrac{R_{ion}}{R_\alpha}} \qquad [VI-39]$$

and correspondingly $\overline{\sigma_e}$ can be calculated from eq.[VI-37]. The equivalent $\overline{R_e}$ as a function of oxygen partial pressure is plotted in Fig. VI-3, . In the calculation, the oxygen partial pressure at one side of the electrolyte is 10^{-17} atm, whereas that on the other side of the electrolyte changes. The values of other parameters have been chosen according to their typical values in the deoxidation experiments, i.e., $\sigma_e^o = 1.3 \times 10^{-7}$ S-atm$^{1/4}$/cm, d=0.2cm, A=10cm^2. It can be seen that $\overline{R_e}$ changes from 49Ω to 26Ω as the oxygen partial pressure on the cathode side changes from 10^{-7} to 10^{-12} atm. The value of R_e is calculated based on the oxygen partial pressures present on each side of the electrolyte, among which Re(low) corresponds to the low oxygen partial side ($P_{O_2}^{II} = 10^{-17}$ atm) and Re(high) to the high oxygen partial pressure side ($P_{O_2}^I$). The values of Re(low) and Re(high) as a function of oxygen partial pressure are plotted in Fig.VI-3. It can be seen that the equivalent $\overline{R_e}$ is very close to but still different from Re(low).

By taking $\overline{R_e}$ as the average of $\overline{R_e}$ at 10^{-7} and 10^{-12} atm, respectively, the flux calculated from eq. [VI-38] deviates from that of eq.[VI-31] by 5% to 8%, as shown in Fig. VI-4. Therefore as long as the change of oxygen pressure is not large, the equivalent circuit can be cautiously used.

It is worth noting that, when $R_{ex} \gg R_{ion}$, which is true in most applications, eq.[VI-39] can be simplified as

$$\overline{R_e} = \frac{d \ln \dfrac{P_{O_2}^I}{P_{O_2}^{II}}}{4A\{\sigma_e^o(P_{O_2}^{II})^{-\frac{1}{4}} - \sigma_e^o(P_{O_2}^I)^{-\frac{1}{4}}\}} - R_{ion} \qquad \text{[VI-40]}$$

and

$$\frac{1}{\overline{\sigma_e}} = \frac{\ln \dfrac{P_{O_2}^I}{P_{O_2}^{II}}}{4\{\sigma_e^o(P_{O_2}^{II})^{-\frac{1}{4}} - \sigma_e^o(P_{O_2}^I)^{-\frac{1}{4}}\}} - \frac{1}{\sigma_{ion}} \qquad \text{[VI-41]}$$

Therefore as long as the oxygen partial pressure on each side of the electrolyte does not change, eq.[VI-38] is as good as eq.[VI-31] if $\overline{R_e}$ is expressed by eq.[VI-39]. It is interesting to note that, since generally R_{ion} is very small compared with R_e, eqs.[VI-40] and [VI-41] can be further simplified to

$$\overline{\sigma_e} = \frac{4\{\sigma_e^o(P_{O_2}^{II})^{-\frac{1}{4}} - \sigma_e^o(P_{O_2}^I)^{-\frac{1}{4}}\}}{\ln \dfrac{P_{O_2}^I}{P_{O_2}^{II}}} \qquad \text{[VI-42]}$$

69
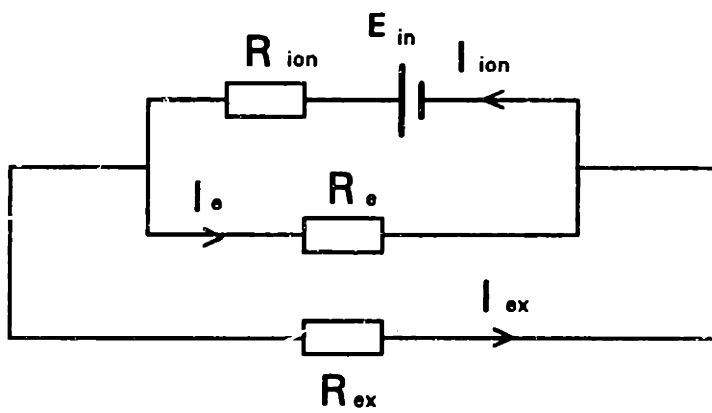
Figure VI-1   Equivalent Circuit of a Solid Electrolyte Cell
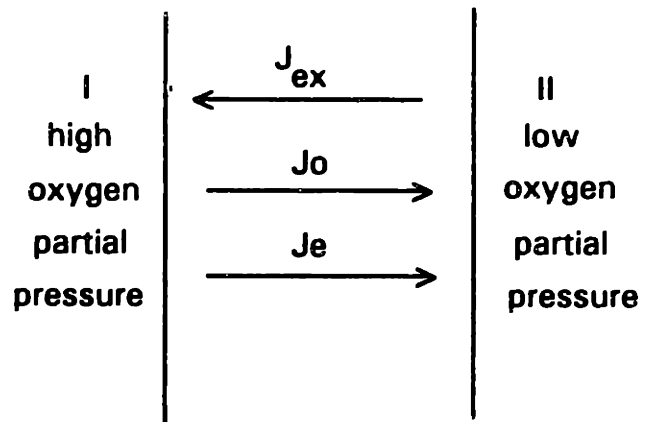
Figure VI-2   Schematic of Transport Process in Stabilized Zirconia Electrolyte
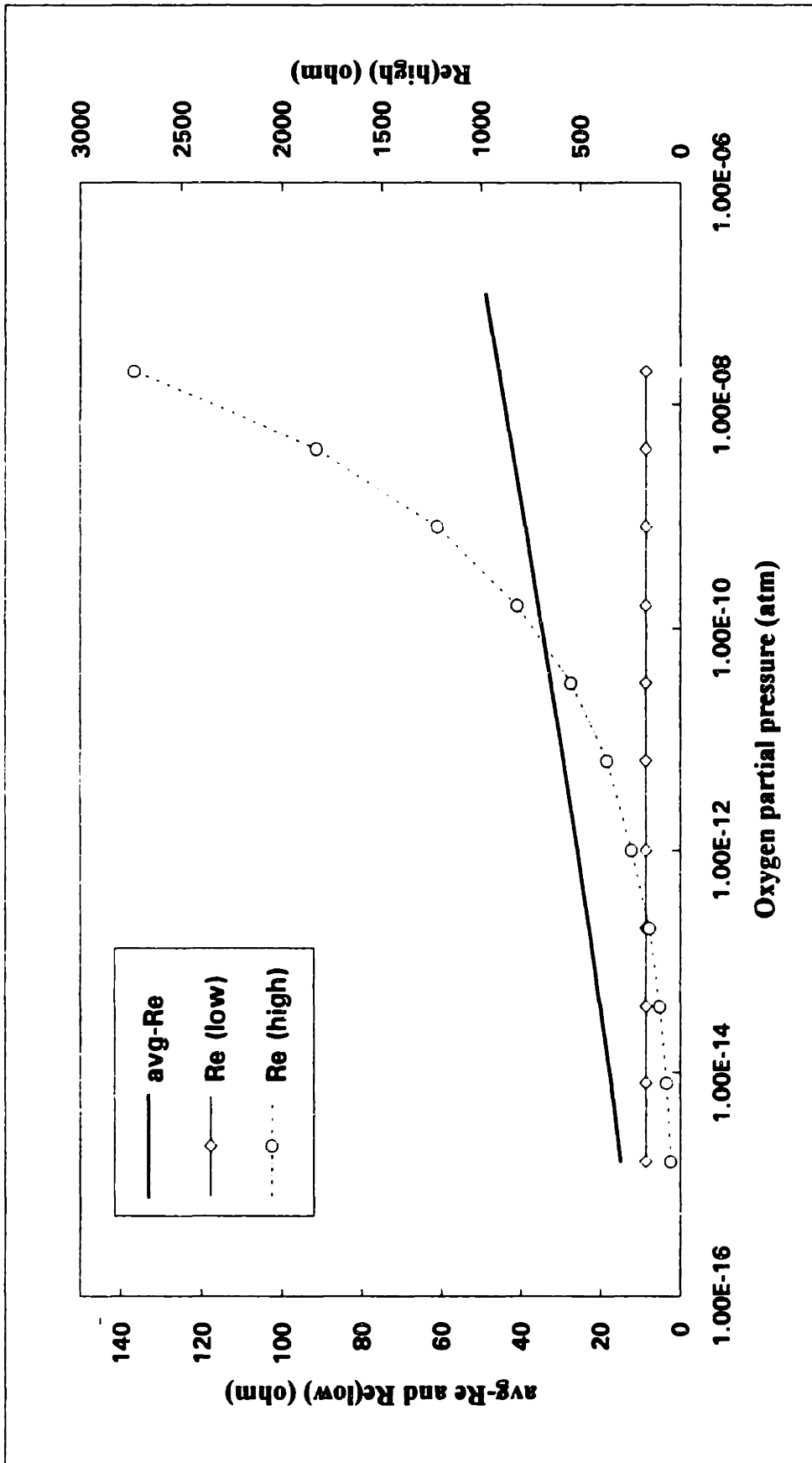
Figure VI-3 Variation of Equivalent Electronic Resistance with Oxygen Partial Pressure
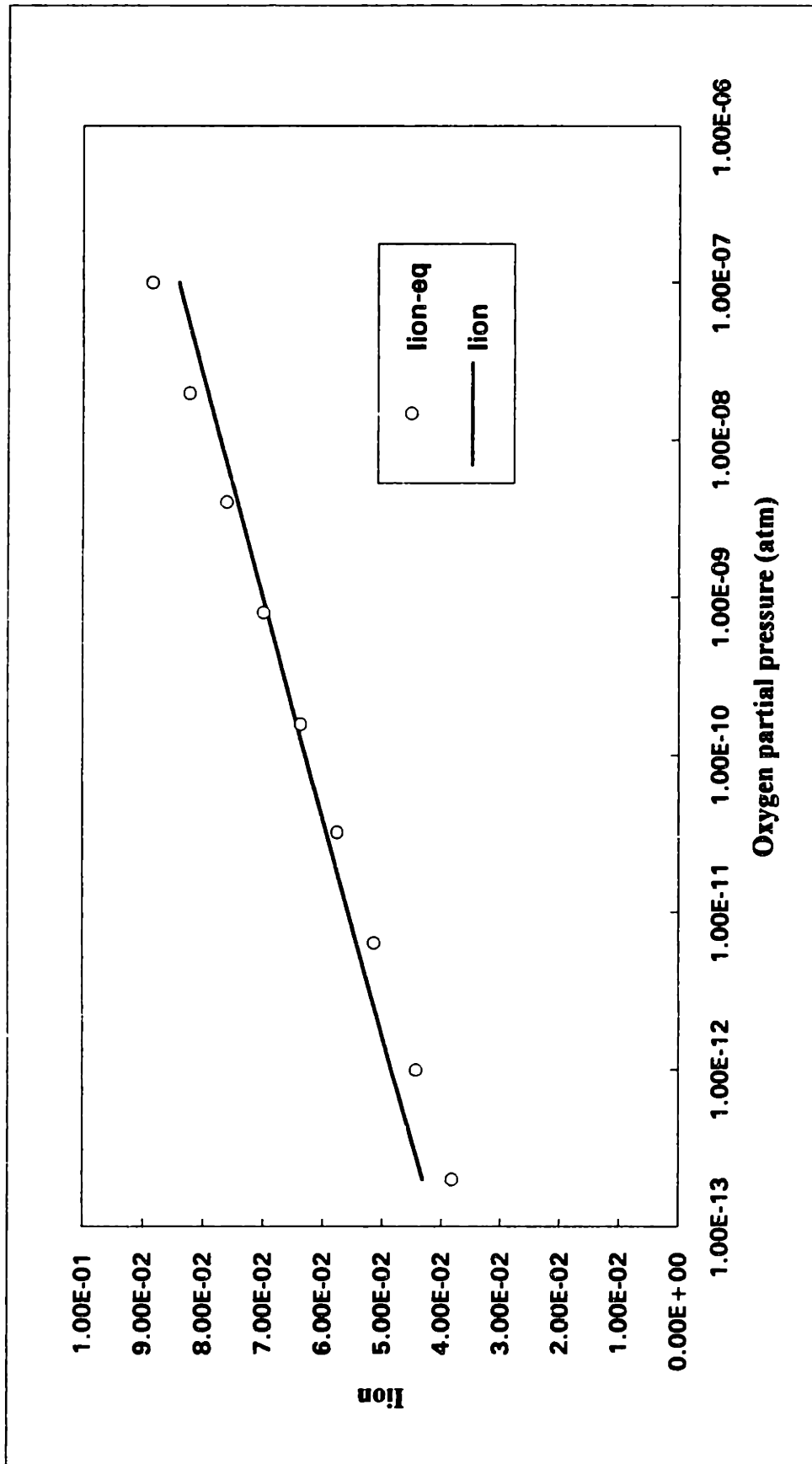
Figure VI-4 Comparison between Fluxes Calculated from Eq. [VI-31] and Equivalent Circuit

73

VII. RESULTS AND DISCUSSION

Based on the discussion in chapter III and V, experimental results are modeled and discussed in this chapter. The deoxidation process is first described by a general model. Then a simpler version of the model, where a planar configuration is adopted, is solved. Based on the solution for the simplified model, the mass transport coefficient of oxygen in the molten copper is determined and the deoxidation process is modeled. The general model is also solved numerically to provide a more detailed picture of the deoxidation process.

VII.A. Transport Analysis

As discussed in chapter V, the deoxidation process can be divided into five steps. Among them, only two steps are rate limiting, i.e., the transport of oxygen ions through the electrolyte and the transport of oxygen atoms in molten copper. The transport of oxygen ions through the electrolyte has been discussed in chapter VI and the flux of oxygen ions is described by eq.[VI-31]:

$$I_{ion} = \frac{RT}{4F(R_{ex} + R_{ion})} \ln \frac{P_{O_2}^{I}}{P_{O_2}^{II}} + \frac{RTAR_{ex}}{(R_{ex} + R_{ion})Fd} \{\sigma_e^o (P_{O_2}^{II})^{-\frac{1}{4}} - \sigma_e^o (P_{O_2}^{I})^{-\frac{1}{4}}\} \quad [VI\text{-}31]$$

Also, based on the discussion on the convective flow in chapter V, the oxygen transport in molten copper can be described by using Fick's law and the concept of boundary layer. In cylindrical coordinates, the Fick's second law can be written as

$$\frac{\partial C(r,t)}{\partial t} = D(\frac{\partial^2 C(r,t)}{\partial^2 r} + \frac{1}{r}\frac{\partial C(r,t)}{\partial r}) \quad [VII\text{-}1]$$

where $C(r,t)$(parts per million, ppm, by weight) is the concentration of oxygen in molten copper at radius r(cm) and time t(s), and $D(cm^2/s)$ is the diffusion coefficient of oxygen in molten copper. To solve this second order differential equation, one initial condition and two boundary conditions are needed.

With the assumption that the oxygen concentration in molten copper is homogeneous at the beginning of the deoxidation process, the initial condition for eq.[VII-1] can be written as:

$$i.c. \quad C(r,0) = C_o \quad r \geq a \qquad \text{[VII-2]}$$

where a(cm) is the outer diameter of the stabilized zirconia tube and C_O is the initial concentration of the melt.

Also, it can be assumed that, during the deoxidation, there is no mass accumulation at the interface between the electrolyte and the melt, and the first boundary condition can be written as

$$b.c. \quad DA\frac{\partial C(r,t)}{\partial r}\bigg|_{r=a} = \frac{M_o I_{ion} * 10^6}{2F\rho_{melt}} \qquad \text{[VII-3]}$$

where $A(cm^2)$ is the interfacial area between the stabilized zirconia tube and molten copper, ρ_{melt} (g/cm^3) is the density of the melt, and M_O (g/mol) is the molecular weight of oxygen atoms. This left side of eq.[VII-3] represents the flux of oxygen through the boundary layer while the right side the flux of oxygen ions through the electrolyte.

Based on the mass balance consideration, the second boundary condition can be written as:

$$b.c. \quad C(\delta,t) = C_o - \frac{\int_0^t \rho_{melt} DA(\frac{\partial C}{\partial r})\bigg|_{r=\delta+a} d\xi}{M_{bulk}} \qquad \text{[VII-4]}$$

where δ(cm) is the thickness of the boundary layer; M_{melt} is the mass of the bulk melt, i.e., the melt beyond the boundary layer.

With the initial and boundary conditions stated above, eq.[VII-1] only has a numerical solution. Though the numerical solution is more accurate, the physical meaning of the problem is usually lost in numbers. In the following part, the transport process of oxygen is first modeled in a simplified way. Then eq.[VII-1] is solved numerically to provide a more detailed picture of the deoxidation process and demonstrate that the simplified version is an approximate solution acceptable for practical analysis.

If the diffusion of oxygen in molten metals is described in a planar configuration, its flux can be described using Fick's first law and the concept of mass transfer coefficient α. Thus:

75

$$J = -D\frac{\partial C}{\partial x} = -\alpha \cdot \Delta C$$

where $\alpha = \dfrac{D}{\delta}$.

If ppm by weight is used as the unit of concentration,

$$I_{ion} = \frac{2\alpha AF(C_b - C_i)\rho_{melt}}{M_o * 10^6} \qquad \text{[VII-5]}$$

where C_b and C_i are the oxygen concentration expressed in parts per million (ppm) in the bulk of the melt and at the interface between the electrolyte and the melt, respectively.

From mass balance consideration,

$$C_b = C_o - \int_0^t \frac{I_{ion} * M_o * 10^6}{2FM_{melt}} d\xi \qquad \text{[VII-6]}$$

Deoxidation experiments have been conducted using different reducing gases, i.e., forming gas (N_2-5%H_2) and pure hydrogen. In the following part, these two situations are discussed separately.

VII.A.1. Forming gas (N_2-5%H_2)

When forming gas (N_2-5%H_2) is used as a reducing gas, the oxygen partial pressure is around 10^{-14} atm. As discussed in chapter VI, under this condition, the second term in eq.[VI-31] is much smaller than the first term, and eq.[VI-31] can be simplified to eq.[VI-32]

$$I_{ion} = \frac{RT}{4F(R_{ex} + R_{ion})} \ln \frac{P_{O_2}^I}{P_{O_2}^{II}} \qquad \text{[VI-32]}$$

Based on the discussion on the copper-oxygen system in chapter II, eq. [VI-32] can be rewritten as :

$$I_{ion} = \frac{RT \ln \dfrac{C_i(melt)}{C_r(red.gas)}}{2FR_{total}} \qquad \text{[VII-7]}$$

where

$$R_{total} = R_{ion} + R_{ex} \qquad \text{[VII-8]}$$

$$C_i = k_s (P_{O_2}^i)^{\frac{1}{2}}, \quad C_r = k_s (P_{O_2}^r)^{\frac{1}{2}} \qquad \text{[VII-9]}$$

Here k_S is the Sieverts' constant and can be calculated from the free energy change involved in the reaction[150]:

$$O_2(g) \rightarrow 2\underline{O} \ (melt)$$
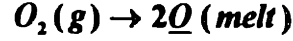
As discussed in chapter V, as a first order approximation, the activity coefficient can be considered to be unity. In eq.[VII-9] the term C_r is introduced to represent the oxygen concentration in the melt that would be in equilibrium with the reducing gas. Determination of C_r under open circuit condition is described in chapter V.

Eq. [VII-7] can be rewritten as:

$$C_i = C_r \exp(\frac{2FI_{ion}R_{total}}{RT}) \qquad \text{[VII-10]}$$

and eq. [VII-5] as

$$C_i + \frac{I_{ion} * M_o * 10^6}{2\alpha AF\rho_{melt}} = C_b \qquad \text{[VII-11]}$$

Substituting eqs.[VII-6] and [VII-10] in eq.[VII-11] gives

$$C_r \exp(\frac{2FI_{ion}R_{total}}{RT}) + \frac{I_{ion} * M_o * 10^6}{2\alpha AF\rho_{melt}} = C_o - \int_0^t \frac{I_{ion} * M_o * 10^6}{2FM_{melt}} d\xi \qquad \text{[VII-12]}$$

Under short circuit condition, C_r varies according to the following relationship (please refer to section VII.F.1.):

$$C_r = k_1 + k_2 I_{ion} \qquad \text{[VII-13]}$$

where

$$k_1 = \frac{k_s}{K_p P_{H_2}} * \frac{\bar{R}T_{rm}}{V} * n_0 \ (O.C.)$$

$$k_2 = \frac{30k_s}{K_p P_{H_2}F} * \frac{\bar{R}T_{rm}}{V}$$

K_p is the equilibrium constant for water dissociation; $\bar{R}$ is the gas constant in the unit of atm-liter/mol-K; V is the flowrate of the reducing gases; T_{rm} is the room temperature and n_0(O.C.) is the amount of oxygen atoms introduced by the reducing gas. Substituting the expression for C_r from eq.[VII-13] in eq.[VII-12] and differentiating eq.[VII-12] with respect to time, the differential of the ionic current with time can be expressed as:

$$\frac{dI_{ion}}{dt} = \frac{-\dfrac{I_{ion}*M_o*10^6}{2FM_{melt}}}{\dfrac{2(k_1+k_2I_{ion})FR_{total}}{RT}\exp(\dfrac{2FI_{ion}R_{total}}{RT})+\dfrac{M_o*10^6}{2\alpha AF\rho_{melt}}+k_2\exp(\dfrac{2FI_{ion}R_{total}}{RT})}$$

[VII-14]

This is a first order differential equation. If all parameters in eq.[VII-14] are known, eq.[VII-14] can be solved by choosing an initial value from the experimental short circuit current.

VII.A.2 Hydrogen

When hydrogen is used, the oxygen partial pressure in the reducing gas is around 10^{-17} atm. Under this condition, the flux of oxygen in stabilized zirconia needs to be expressed by eq.[VI-31] instead of eq.[VI-32]. Substituting eq.[VII-6] in eq.[VII-5] to eliminate C_b gives

$$I_{ion} = \frac{2\alpha AF\rho_{melt}}{M_o*10^6}(C_o - \int_o^t \frac{I_{ion}*M_o*10^6}{2FM_{melt}}d\xi) - \frac{2\alpha AF\rho_{melt}}{M_o*10^6}C_i \qquad [VII-15]$$

Differentiating eq. [VII-15] gives

$$\frac{dI_{ion}}{dt} = -\frac{\alpha A\rho_{melt}}{M_{melt}}I_{ion} - \frac{2\alpha AF\rho_{melt}}{M_o*10^6}\frac{dC_i}{dt} \qquad [VII-16]$$

Substituting eq.[VII-9] in eq.[VI-31] gives

78

$$I_{ion} = \frac{RT}{2F(R_{ex} + R_{ion})} \ln \frac{C_i}{C_r} + \frac{R_{ex}}{R_{ex} + R_{ion}} \frac{RTA}{Fd} \{\sigma_e^o (\frac{C_r}{k_s})^{-\frac{1}{2}} - \sigma_e^o (\frac{C_i}{k_s})^{-\frac{1}{2}}\} \quad [VII-17]$$

Substituting eq. [VII-13] in eq. [VII-17] to eliminate C_r and differentiating eq. [VII-17] give

$$\{1 + \frac{RT}{2F(R_{ex} + R_{ion})} * \frac{k_2}{k_1 + k_2 I_{ion}} + \frac{R_{ex}}{R_{ex} + R_{ion}} \frac{RT\sigma_e^o A k_s^{\frac{1}{2}}}{2Fd} \frac{k_2}{(k_1 + k_2 I_{ion})^{\frac{3}{2}}}\} \frac{dI_{ion}}{dt} =$$

$$\{\frac{RT}{2F(R_{ex} + R_{ion})} \frac{1}{C_i} + \frac{R_{ex}}{R_{ex} + R_{ion}} \frac{RT\sigma_e^o A k_s^{\frac{1}{2}}}{2Fd} \frac{1}{C_i^{\frac{3}{2}}}\} \frac{dC_i}{dt}$$

$$[VII-18]$$

Combining eqs. [VI-16] and [VI-23] gives

$$I_{ex} = \frac{RT}{4FR_{ex}} \ln \frac{P_{O_2}^I}{P_{O_2}^{II}} - \frac{I_{ion} R_{ion}}{R_{ex}} \quad [VII-19]$$

If the mass transfer coefficient and σ_e^o are known, eqs. [VII-16], [VII-18] and [VII-19] can be solved and the $I_{ex}(t)$ and $I_{ion}(t)$ curves can be modeled. Thus it is possible to predict $I_{ex}(t)$ curve and compare it with the experimental curve. Also, once $I_{ion}(t)$ is modeled, eq. [VII-6] can be used to predict the variation of oxygen concentration as a function of the deoxidation time.

VII.B. Mass Transport Coefficient

As indicated in eq.[VII-14], [VII-16] and [VII-18], in order to model the deoxidation process, the value of the mass transport coefficient of oxygen in molten copper is needed. In this part the measurement of the oxygen mass transport coefficient is discussed.

In the case when forming gas (N_2-5% H_2) is used as a reducing gas, combining eq.[VI-32] and eq.[VII-19] gives

$$I_{ex} = I_{ion} \quad [VII-20]$$

Moreover, when the ionic current is small, in the denominators of eq.[VII-14], the terms changing with the current become negligible, and eq.[VII-14] can be simplified as (Please refer to VII.F.2. for an error analysis.)

$$\frac{dI_{ion}}{dt} = -\frac{I_{ion}\alpha A \rho_{melt}}{M_{melt}}$$

and
$$\ln(I_{ion}) - \ln(I_{ion}^0) = -\frac{\alpha A \rho_{melt}}{M_{melt}}(t - t_o) \qquad [\text{VII-21}]$$

Substituting eq.[VII-20] in eq.[VI-21] gives

$$\ln(I_{ex}) - \ln(I_{ex}^0) = -\frac{\alpha A \rho_{melt}}{M_{melt}}(t - t_o) \qquad [\text{VII-22}]$$

Therefore by performing a linear regression of ln (I_{ex}) vs. time, the mass transport coefficient α can be obtained. Typical plots of ln (I_{ex}) vs. time for experiments with gas stirring using two tubes, gas stirring using one tube and induction stirring, are shown in Figs. VII-1, VII-2 and VII-3 for experiments L, Q and E, respectively. From the slope of ln (I_{ex}) vs. time plots and some of the experimental parameters listed in Table VII-1, the mass transfer coefficient of oxygen, α, in the melt is calculated. The linear regression analysis data for some other experiments can be found in Table VII-2. In the following part, several factors affecting the magnitude and the calculation of the mass transport coefficient, such as stirring intensity, experimental temperature, and the types of reducing gases, are discussed.

VII.B.1. Stirring Intensity

Stirring in molten copper is provided by both induction and gas bubbling, and the later is provided by either one or two tubes.

Two-tube bubbling - In most deoxidaton experiments conducted in the resistance heating furnace, stirring is provided by Ar bubbling through two tubes, positioned symmetrically around the device. Those experiments are conducted in crucibles with an inner diameter of 5.5cm. The mass of copper used is usually 600g with a melt depth of around 3.4cm. The flow rate of Ar is 50ml/min.

The plot of ln (I_{ex}) vs. time for a typical two-tube bubbling experiment is shown in Fig. VII-1. It is found that, at T=1406K, the average value of the oxygen mass transport coefficient α is on the order of 10^{-3} cm/s.

80

One-tube bubbling - Melts have also been stirred by argon bubbling through one tube. In those experiments, two kinds of crucibles have been used. One is the same as that used in the two-tube bubbling experiments. The other is a crucible with an inner diameter of 3.6cm. The mass of copper used in this case is 400g with a melt depth of around 7cm. A typical plot of ln (I_{ex}) vs. time is shown in Fig. VII-2. It is found that, under similar experimental conditions, i.e., the same experimental temperature and Ar flowrate, the mass transport coefficient α in the one-tube bubbling experiments is only half of that in the two-tube bubbling experiments. This implies that the distribution, intensity and bubble size of Ar in the melt influence the mass transfer coefficient of oxygen in the melt.

Induction stirring - No gas bubbling is provided in deoxidation experiments conducted in the induction furnace. The melt was inductively stirred. In those experiments, crucibles with an average inner diameter of 6.03cm have been used. The mass of copper used was around 700g with a melt depth of around 3.1cm. A plot of ln (I_{ex}) vs. time is shown in Fig. VII-3. It is worth noting that the mass transport coefficient in the induction experiments is one order of magnitude greater than that obtained in the gas bubbling experiments. It shows the difference in stirring intensities between gas bubbling and induction heating.

VII.B.2. Reducing Gases

In experiments discussed above, forming gas has been used, and therefore eq.[VII-22] could be used. When hydrogen is used as a reducing gas, the oxygen partial pressure is around 10^{-17} atm. Under this condition, the electronic current becomes appreciable and the ionic current I_{ion} is no longer equal to I_{ex}. However, it is interesting to note that a linear regression of ln(I_{ex}) vs. time still gives a behavior similar to that when forming gas was used. An example of this is shown in Fig. VII-4 which contains a plot of ln(I_{ex}) versus 't'. The values of the mass transport coefficients obtained from the experiments with forming gas and hydrogen are also very similar in magnitude (Table VII-1). This suggests that when the electronic current becomes appreciable, it is still possible to obtain the mass

transport coefficient from the linear regression of external current as a first order approximation. Error analysis has been conducted in VII.F.2. The calculated values for α are listed in the last column of Table VII-1.

VII.B.3. Temperature

The effect of temperature on mass transport coefficients has also been evaluated by conducting experiments at different temperatures. If the mass transport coefficient is expressed in the form $\alpha = \alpha^o \exp(-E_o / RT)$, it can be seen from Fig. VII-5 that, by plotting Lnα versus 1/T and performing linear regression analysis, the activation energy of the mass transport coefficient of oxygen in molten copper is found to be around 100kJ/mol. Previously reported data are also plotted in Fig. VII-5. As shown in Fig. VII-5, temperature has only a small influence on the mass transport process in copper, e.g., the mass transport coefficient of oxygen in copper melt increases by only two folds with one to two hundred degree increase in temperature.

Though mass transfer coefficient has been widely used in industry, there have been few studies on the oxygen mass transfer coefficient in molten metals. Typically empirical values have been used in industry. The mass transfer coefficients in our experiments with induction stirring are slightly smaller than the value reported by Oberg et al.[151] and larger than the value reported by Odel et al. [152]. The fluid flow in induction furnace has been modeled by various authors[153,154,155,156]. According to Tarapore[157], coil height, turn spacing, current, phasing and melt height have large effects on induction stirring, and on the other hand, frequency and coil diameter have little influence. Since those data are not complete in the literature, it is difficult to compare the previously reported data with that obtained in this study. However, it is worth mentioning that, for one-tube gas bubbling experiments, the thickness of the diffusion layer, which is calculated from D/α, is 1.3×10^{-1} cm. It is quite close to that reported by Iwase[158]. In Iwase's experiments, the mass transfer coefficient of oxygen was measured in molten steels stirred by argon with a flowrate of 50ml/min at 1873K. The physical properties of the molten

steel and molten copper, such as viscosity and density, are quite similar at their melting points. Also, Iwase's experimental conditions, such as the aspect ratio of the melt and the flowrate of argon, are quite similar to that of the one-tube bubbling experiments in this study. Therefore it is not surprising that the diffusion layer thickness measured in these two studies are similar.

VII.C. Modeling

The deoxidation process using solid electrolyte cells have been modeled as outlined above both when forming gas and hydrogen were used as reducing gases.

VII.C.1. Forming Gas

When forming gas is used, it has been shown that the differential of the ionic current with time can be expressed as eq.[VII-14]. Since eq.[VII-14] is a first order differential equation and $I_{ion} \equiv I_{ex}$, by noting the value of the short circuit current at any time t and utilizing the value of experimental parameters from Table I, Eq. [VII-14] can be solved and the short circuit current vs. time curve $I_{ex}(t)$ can be modeled.

In modeling, ρ_{melt}, M_o, K_p, k_s, and F are obtained from literature. From the experimental arrangement, A and M_{melt} are obtained. As discussed in chapter V, the flowrate of the forming gas V, the experimental temperature T, the water vapor partial pressure $P'_{H_2O}(O.C.)$, C_o and C_r, are measured during experiments.

R_{total} has been measured by two different methods: 1) the short circuit current (I_1) at the end of the experiment and the open circuit voltage (V_1) at the instant the circuit was broken were measured (using a data acquisition system), and the ratio V_1/I_1 was obtained to get R_{total}; 2) the open circuit voltage (V_2) before short circuiting and the current (I_2) at the instant when the circuit was short-circuited were measured, and the ratio of V_2/I_2 was obtained. R_{total} measured by method 1) is usually larger than that measured by method 2). This might be due to the following reasons: a) The short circuit current I_2 measured in 2) could have a contribution from the capacitance of electrodes. This will make the current being measured appear larger than the ohmic current and

therefore make R_{total} smaller; b) In method 1), at the instant the circuit is broken, the instantaneous relaxation of the electrode concentration polarization can make the device voltage reading appear larger than the real value. This can also lead to a larger R_{total}. It is found that the best curve fitting is obtained when R_{total} falls between the values measured by method 1) and method 2).

Both the experimental and the modeled curves for experiment L and D listed in Table VII-1, have been plotted in Fig. VII-6 and VII-7, respectively. The corresponding concentration vs. time curves obtained using eq.[VII-6] are compared with the experimental values and also plotted in the same figures. From these figures it appears that the short circuit current versus time curve can be divided into three zones. In Zone I the current decreases very rapidly and the time interval is very short (<1 min), Zone II is more leveled where the current decreases slowly and Zone III is characterized by an exponential decay. In the later part those observations are analyzed.

VII.C.2. Hydrogen

When hydrogen is used as the reducing gas, the ionic current vs. time, $I_{ion}(t)$, and the external current vs. time, $I_{ex}(t)$, can be obtained by solving eqs. [VII-16], [VII-18] and [VII-19]. More specifically, the following procedure has been adopted for modeling the deoxidation process:

1)Copper samples are taken before and after the deoxidation experiments. Samples are analyzed and the initial (C_{ini}) and final (C_{final}) oxygen concentration are determined.

2)Using $C_{ini}=C_b$ and other experimental parameters from Table I, $I_{ion}(0)$ and $C_i(0)$ are obtained by solving eqs. [VII-5] and [VII-17].

3) Eqs. [VII-16] and [VII-18] are first order differential equations with two variables. All parameters in these equations are known except for σ_e^o. By using the initial conditions obtained in step #2 and choosing arbitrary σ_e^o, $I_{ion}(t)$ can be obtained by an iterative technique. Then from eq.[VII-19], $I_{ex}(t)$ is also calculated.

4) By adjusting σ_e^o, the experimental external current curve can be fitted with modeled $I_{ex}(t)$ curve and the corresponding $I_{ion}(t)$ curve can be obtained to verify that the amount of the oxygen removed as calculated from eq. [VII-6] is consistent with the value measured by sampling.

Two typical modeled ionic and external current vs. time curves for hydrogen are shown in Fig. VII-8 and VII-9 for experiment A and B, respectively. The corresponding concentration curves obtained from eq.[VII-6] are also plotted. This method has been applied to model all the deoxidation data and the value of σ_e^o was found to be on the order of 3×10^{-7} S/cm, which is consistent with that reported in the literature[159,160].

It is worth mentioning that, similar to the deoxidation using forming gas, when hydrogen was used, the deoxidation current curves can also be divided into three zones with similar characteristics, i.e., zone I with a fast drop of the deoxidation current, zone II with a leveled decrease of the current and zone III with an exponential decay of the current.

VII.D. Digital simulation

VII.D.1. General Description

In this section, eq. [VII-1] is solved numerically by using finite difference. Detailed description of this method can be found in [161]. Here the methodology is briefly presented and the computer program used is listed in the appendix.

As shown in Fig. VII-10, the diffusion layer can be divided into cylindrical shell elements with a thickness h . Concentration within those elements is described by an array of C[i] and C'[i] at time t and t+δt, respectively. The flux into the element i is the sum of the oxygen fluxes from the i+1 and i-1 elements. Among them, C[0] and C'[0] represent interfacial oxygen concentrations at time t and t+δt, respectively. It may be noted that, C[i] and C'[i] represent the concentrations at $r_i = a + i*h$, where a is the outer diameter of the zirconia tube, h=δ/n, and n is the number of elements in the array. By applying a finite difference expression, eq.[VII-1] can be written as

$$\frac{C'[i]-C[i]}{\delta t} = D\{\frac{C[i+1]-2C[i]+C[i-1]}{h^2} + \frac{1}{r_i}\frac{C[i+1]-C[i-1]}{2h}\}$$

Accordingly, eq.[VII-1] can be solved numerically by solving a series of finite-difference equations such as

$$C'[i] = C[i] + \frac{D\delta t}{h^2}\{C[i+1]-2C[i]+C[i-1]+\frac{h}{2r_i}(C[i+1]-C[i-1])\}$$

where the oxygen concentration at the boundary of the array can be expressed as

$$C'[0] = C[0] - h\frac{\partial C(r,t)}{\partial t}\bigg|_{r=a} \quad \text{and}$$

$$\frac{\partial C(r,t)}{\partial t}\bigg|_{r=\delta+a} = \frac{C[n]-C[n-1]}{h}$$

In constructing finite elements, there are two methods: point method and box method. Here point method has been used. Detailed discussion about those two methods can be found in [162]. As recommended by Britz [163], the 5-point method to express the concentration gradient at the melt/electrolyte interface and the Runge-Kutta integration (RKI) are used to solve eq. [VII-1]. The principle of the 5-point method is to express the concentration gradient by polynomials:

$$C'[0] = (48C[1]-36C[2]+16C[3]-3C[4]-12h\frac{\partial C(r,t)}{\partial t}\bigg|_{r=a})/25$$

$$\frac{\partial C(r,t)}{\partial r}\bigg|_{r=\delta+a} = (25C[n]-48C[n-1]+36C[n-2]'-16C[n-3]+3C[n-4])/(12*h)$$

The RKI method is described in VII.F.4. The stability and convergence of the numerical solution are determined by the dimensionless parameter $\lambda=D\delta t/h^2$ [164]. It has been shown [165] that, when λ is larger than 0.5, simulations will no longer correspond to reality. In the simulations of this study, λ is chosen to be around 0.49.

VII.D.2. Curve Fitting

Similar to the modeling in section VII.C., the values for ρ_{melt}, M_o, F, a, A, M_{bulk}, C_o, C_r, and R_{total} are obtained from experiments. By selecting an appropriate value for λ in the digital simulation process eq.[VII-1] is solved and the concentration profile as a function of time is obtained. By using eq.[VII-7] the short circuit current versus time curves is calculated.

By choosing an appropriate $D=6.8 \times 10^{-9} m^2/s$[166] and adjusting the diffusion layer thickness (δ) the experimental short circuit current versus time curves can be obtained, as shown in Fig. VII-11 for experiments L. It is apparent that the simulated and the experimental short circuit current versus time curves agree well with each other in all three zones. It may be noted that, the mass transfer coefficient (D/δ) calculated from digital simulation agrees well with the value obtained using the previous model, which also proves the validity of the previous model.

VII.D.3. Interfacial Concentration

The kinetics of the deoxidation process is closely related to the magnitude of the interfacial oxygen concentration at the interface between the electrolyte and the molten copper. A higher interfacial concentration favors a larger oxygen flux through electrolytes, while the higher interfacial concentration could also lead to a smaller concentration gradient across the boundary layer which means a smaller diffusion flux. The experimental interfacial oxygen concentration can be estimated from the short circuit current using eq.[VII-10], whereas the modeled interfacial concentration can be calculated from the modeled deoxidation current obtained from eq.[VII-14] and the simulated interfacial concentration from the digital simulation. The modeled and simulated interfacial concentration for experiment L are shown along with the experimental interfacial concentration in Fig. VII-12 and Fig. VII-13, respectively. It can be seen that, compared with the modeled interfacial concentration, the simulated interfacial concentration has a better fit to the experimental interfacial concentration, especially during the initial stages of

the deoxidation process. This shows that the simulation provide a more accurate picture of the deoxidation process.

As mentioned in the preceding sections, the deoxidation current curves can be divided into three zones. Correspondingly the plot of the interfacial concentration obtained from digital simulation can be also divided into three zones. Zone I is characterized by a fast drop of interfacial oxygen concentration, which represents a concentration polarization at the cathode and corresponds to the fast drop in the deoxidation current. In zone II, the interfacial oxygen concentration decreases roughly at a constant rate, which corresponds to a leveled drop in the deoxidation current. When the interfacial oxygen concentration is close to zero, the deoxidation process enters zone III, the deoxidation current is characterized by an exponential decay.

VII.E. Process Analysis

VII.E.1. Process Overview

Based on the preceding discussion, the following observations have been made :

1. Zone I corresponds to a very short duration of time (<1 min) and the amount of oxygen removed in this zone is negligible. Hence, the overall deoxidation kinetics is not influenced by Zone I. It is interesting to note that the transition time of zone I in deoxidation experiments using hydrogen is usually a little bit longer than that using forming gas. Since this transition period is related to a diffusion process, given the same diffusion coefficient of oxygen and the same diffusion layer thickness, the transition time should be the same. The reason for this is not clear, and it might be related to the change of C_r between the open and short circuit modes.

2. Zone II is not controlled by the mass transfer coefficient of oxygen, but rather by the value of R_{total}. The value of R_{total} must be minimized in order to increase the short circuit current and enhance the deoxidation kinetics in this zone.

3. Zone III is controlled by the mass transfer coefficient of oxygen in the melt. In this zone, the short circuit current decreases more rapidly (as compared to Zone II) and

remains at a low level. Hence, in order to improve the over all deoxidation kinetics, the best thing to do is to maximize the duration and the current in Zone II.

VII.E.2. Mass Transfer Coefficient

As mentioned before, mass transfer coefficient does not increase much with the increase in temperature. Therefore, it is not wise to increase the temperature to improve the deoxidation kinetics because the benefit in terms of increased mass transport is only marginal as compared to the additional energy required and other difficulties associated with increasing process temperature, e.g., refractory ware, volatilization, etc.

VII.E.3. Flowrate and Types of Reducing Gases

Under open circuit condition, different reducing gases have different residual oxygen contents ($P_{O_2}(O.C.)$). Both the flowrate and the residual oxygen content of the reducing gas affect its oxygen partial pressure under short circuit condition ($P_{O_2}(S.C.)$), and correspondingly, also influence the deoxidation kinetics.

The influence of the type of the reducing gas can be assessed by comparing experiments conducted under similar experimental conditions but using different reducing gases. Figs. VII-14 shows the concentration vs. time curves for experiment B and E. Except for the difference in the residual oxygen partial pressures in the reducing gases ($P_{O_2}(O.C.)$ is 10^{-17} atm for experiment B and 10^{-14} atm for experiment E), all other conditions for experiments B and E are roughly the same. For oxygen concentration to decrease from 50 ppm to 20 ppm, it took 50 minutes for experiment E and 33 minutes for experiment B. It appears that the deoxidation kinetics improves significantly by decreasing the oxygen partial pressure in the reducing gases.

Similarly, to observe the influence of the flowrate of the reducing gases on the deoxidation kinetics, the concentration vs. time curves for experiment C and D are compared in Fig. VII-15. Forming gas has been used in both experiments, but the flowrate of the forming gas is 120ml/min for experiment C and 245ml/min for experiment D. The other experimental conditions for experiments C and D are roughly the same except that

the R_{ex} of experiment C is a little smaller than that of experiment D, as shown in Table VII-1. It is interesting to note that the slope of the concentration vs. time curve are roughly the same, which means that, in both experiments, the oxygen removal rates are similar.

The above observations can be explained by examining the model discussed in the previous section. One can conclude from eq.[VII-13] and Appendix VII.F.1. that the oxygen partial pressure in the reducing gases under short circuit condition $P_{O_2}(S.C.)$ is decreased by increasing the flowrate or lowering the open circuit oxygen partial pressure $P_{O_2}(O.C.)$ of the reducing gases. This decrease, in turn, improves the deoxidation kinetics. The initial oxygen partial pressure ($P_{O_2}(O.C.)$) in the reducing gas determines the amount of oxygen in reducing gases under open circuit condition, and influences C_r as reflected in the first term of eq.[VII-13]. Referring to Appendix VII.F.1., it is seen that the first term of eq.[VII-13] is not affected by the flowrate of the reducing gas. Rather, the influence of the flowrate of the reducing gas is reflected in the second term of eq.[VII-13]. This term shows how the oxygen partial pressure in the reducing gases is changed by the deoxidation current. The higher the flowrate, the smaller the effect of the deoxidation current on the oxygen partial pressure in the reducing gases.

Since the deoxidation currents in both experiment C and D are relatively small, the changes in the oxygen partial pressures of the reducing gases due to the deoxidation current are also small, and the increase of the flowrate will make this change even smaller. Therefore the effect of the flowrate increase can be hardly seen in these experiments, as shown in Fig. VII-15. Another reason for this observation is that the influence of the flowrate increase in experiment D is offset by its larger external resistance which tends to make the deoxidation kinetics slower.

Similarly, Fig. VII-14 can also be explained by eq.[VII-13]. Because of the relatively small deoxidation current, the change of the oxygen partial pressure in the reducing gas under short circuit condition, which is reflected in the second term of

eq.[VII-13], is small. Accordingly, the small contribution of the second term in eq.[VII-13] makes it easy for us to observe the influence of the first term on the deoxidation kinetics, as shown in Fig. VII-14. Also, it is worth mentioning that this improvement in kinetics is also partly due to the contribution of the electronic conductivity of the electrolyte.

The above discussion is based on the condition that the deoxidation current is small. However, if the deoxidation process is scaled up for industrial use, the deoxidation current is expected to be much higher, and eq.[VII-13] can once again be used to rationalize the effects of the residual oxygen content in the reducing gas and its flow rate. With a larger deoxidation current, the oxygen partial pressure in the reducing gas under short circuit condition is expected to greatly deviate from the value under open circuit condition. Under this condition, the influence of the second term of eq.[VII-13], which includes the flow rate of the reducing gas, is expected to increase. The implications of scale-up are discussed in chapter VIII.

In this study, it is observed that, under open circuit condition, as the flowrate of the reducing gas increases, the device voltage increases. When forming gas is used the effect of the reducing gas flowrate on the device voltage is negligible. When hydrogen is used, the device voltage reading increases by about 5mV with 100ml/min increase in flowrate. Considering the high experimental temperature (around 1400K), the equilibrium between water vapor, hydrogen and oxygen should be reached instantaneously. Therefore it is safe to assume that the reducing gas reaches an equilibrium as soon as it reaches the Ni-zirconia cermet, and the oxygen partial pressure in the reducing under short circuit condition should be independent of the flowrate of the reducing gas. The slight discrepancy observed in the case of hydrogen could be due to several reasons. One of them is the depolarization of the anode. As discussed in chapter IV, though the concentration polarization at anode is calculated to be very small, the higher flowrate is expected to make this polarization smaller. Another possible reason is that some of the

tubes used are silicone rubber tubes through which oxygen molecules can slowly diffuse. The higher flowrate tends to dilute this contamination, and this drags down the oxygen partial pressure and correspondingly increases the device voltage reading.

Another key factor that influences the deoxidation kinetics is the ratio between the interfacial area and the mass of the melt, A/M_{melt}, , especially during the stage when the deoxidation kinetics is controlled by mass transfer coefficient of oxygen in the melt. Therefore, the scale-up design of the electrolyte cell must seek to maximize the ratio 'A/M_{melt}' for a given mass of the melt.

VII.F. Appendix

VII.F.1. Oxygen Partial Pressure Under Short Circuit Condition

Oxygen partial pressure in reducing gas under short circuit condition--$Po_2^r(S.C.)$

Oxygen concentration in Cu melt in equilibrium with reducing gas under short circuit condition--$C_r(S.C.)$

Under short circuit conditions, the oxygen from molten copper that passes through the electrolyte into the reducing gas (hydrogen) completely reacts to form water vapor. The oxygen partial pressure in the reducing gas is then fixed by the H_2/H_2O equilibrium.

The number of moles of oxygen atoms present in V (liter) of the reducing gas flowing through the device per minute (measured at room temperature) under open circuit condition is

$$n_O(O.C.)' = \frac{P_{H_2O}^r(O.C.)*V}{\bar{R}T_{rm}} + \frac{2*P_{O_2}^r(O.C.)*V}{\bar{R}T_{rm}}$$

where T_{rm} is the room temperature and $\bar{R}$ is gas constant in the unit of atm-liter/mol-K. Since $P_{H_2O}^r(O.C.) >> P_{O_2}^r(O.C.)$ (typically, $P_{H_2O}^r(O.C.)$ is on the order of 0.01atm while $P_{O_2}^r(O.C.)$ is around 10^{-14} atm), the above equation can be written as

$$n_O(O.C.) = \frac{P_{H_2O}^r(O.C.)*V}{\bar{R}T_{rm}}$$

Also, the number of moles of oxygen atoms pumped into the reducing gas per minute is
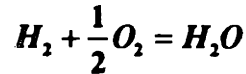
$$n_O(p) = \frac{60 I_{ion}}{2F}$$

Therefore under short circuit conditions, the water vapor pressure in the reducing gas is

$$P_{H_2O} = [n_O(O.C.) + \frac{60 I_{ion}}{2F}] * \frac{\tilde{R}T_{rm}}{V}$$

and the oxygen partial pressure in the reducing gas is

$$Po_2'(S.C.) = (\frac{P_{H_2O}}{K_p P_{H_2}})^2$$

where K_p is the equilibrium constant for the reaction

$$H_2 + \frac{1}{2}O_2 = H_2O$$

Therefore $C_r(S.C.) = \dfrac{k_r}{K_p P_{H_2}} * \dfrac{\tilde{R}T_{rm}}{V} * [n_O(O.C.) + \dfrac{30 I_{ion}}{F}]$.

VII.F.2. Error Analysis

As mentioned before, when the ionic current is small, the terms changing with current in eq.[VII-14] can be neglected, and eq.[VII-14] can be simplified to eq.[VII-21]. By calculating the ratio β between the terms changing with the ionic current and the whole denominator in eq.[VII-14], the error involved in the simplification of eq.[VII-14] can be estimated.

Since the terms changing with the ionic current in eq.[VII-14] decrease as the deoxidation current decreases, the smaller the current, the smaller the error. Therefore by calculating the value of β at the maximum current value which has been used in calculating the oxygen mass transfer coefficient, the maximum error involved in the simplification of eq.[VII-14] can be also estimated. It can be shown that the error thus calculated is less that 5%. At the average current value, the error involved is much less that 2%.

When hydrogen is used as a reducing gas, eq.[VII-21] has to be modified in order to accommodate the electronic conductivity. It is obvious that eq.[VII-16] is still applicable with hydrogen as the reducing gas. As the ionic current decreases and becomes small, the term containing dC_i/dt in eq.[VII-16] can be neglected because it decreases much faster than the term containing I_{ion} and eq.[VII-16] can be integrated and expressed

as shown in eq.[VII-21]. Based on a similar argument presented above, the maximum error involved in this simplification can be calculated to be around 3%.

To estimate the error involved in replacing eq.[VII-22] with eq.[VII-21], the following procedure has been followed:

1) By using eq.[VII-22], the mass transfer coefficient of oxygen α is calculated by linear regression;

2) By using α calculated in 1), the ionic current and external current vs. time are obtained as described in VII.C;

3) Based on the results of $I_{ex}(t)$ and $I_{ion}(t)$, the error involved in replacing eq.[VII-22] with eq.[VII-21] is calculated as follows. If it is defined as

$$I_{\alpha} = \lambda I_{ion}$$

it gives
$$\ln(I_{\alpha}) = \ln \lambda + \ln(I_{ion})$$

where λ changes as the deoxidation proceeds and is less than one since the external current is always smaller than the ionic current. With the knowledge of $I_{ex}(t)$ and $I_{ion}(t)$ from 1) and 2), the change of λ is calculated. It shows that the change of λ is not significant, e.g., for experiment B, λ changed from 0.84 to 0.65 when the external current changed from 87 mA to 31 mA. Correspondingly the error in calculating the mass transfer coefficient is around 10%. Taking to account the error incurred in obtaining eq.[VII-21], the maximum total error involved was around 13%. This is still acceptable for the measurement of the mass transport coefficient α.

VII.F.3. Sensitivity Test

During modeling, except for the ionic conductivity of the electrolytes, all parameters are either experimentally measured or obtained from the literature. As discussed in chapter II, the ionic conductivity is expected to be within 0.1S/cm - 0.5S/cm. From the equivalent circuit as shown in Fig. VI-1, it is apparent that an accurate value of the ionic conductivity of the stabilized zirconia will not be important if the external resistance is relatively large. This can also be demonstrated by Fig. VII-16, which is the

modeled curve for experiment B. It can be seen that by varying the ionic conductivity of the electrolyte from 0.1S/cm to 0.5S/cm, the variation of the modeled current is less than 2 %. Therefore the modeled curve is not sensitive to the ionic conductivity of the electrolytes.

VII.F.4. RKI techniques

The detailed description about Runge-Kutta Integration (RKI) method can be found in most textbooks on numerical analysis[167, 168]. The basic principle can be explained by Fig. VII-17, where a function u(t) is to be solved for t+δt, point B, starting from point A, given the first-order differential equation

$$\frac{du}{dt} = f(u)$$

What the standard explicit digital simulation method does is to move along the slope of u(t) at t, point A, to t+δt, point C. And then the calculation is continued at point D. This is called the first-order (Euler) method and can be expressed in the following notation:

$$\Delta_1 = \delta\! f(t)$$

$$u(t + \delta t) \approx u + \Delta_1$$

Then $f(u + \Delta_1)$ is the slope at the point D. What RKI method does is to go only half-way along the slope $f(u(t))$, to point E, and then the rest of the way with the new slope at D. This will end up at point F, which is much closer to point B, the true solution. This description can be expressed mathematically as

$$\Delta_2 = \delta\! f(u + \Delta_1)$$

$$u(t + \delta t) \approx u + \frac{\Delta_1 + \Delta_2}{2}$$

Analysis has shown that the error in this method is of $O(\delta t^2)$, as opposed to $O(\delta t)$ in the first order (Euler) method. This method can be further improved by a third- or even fourth order sequence.
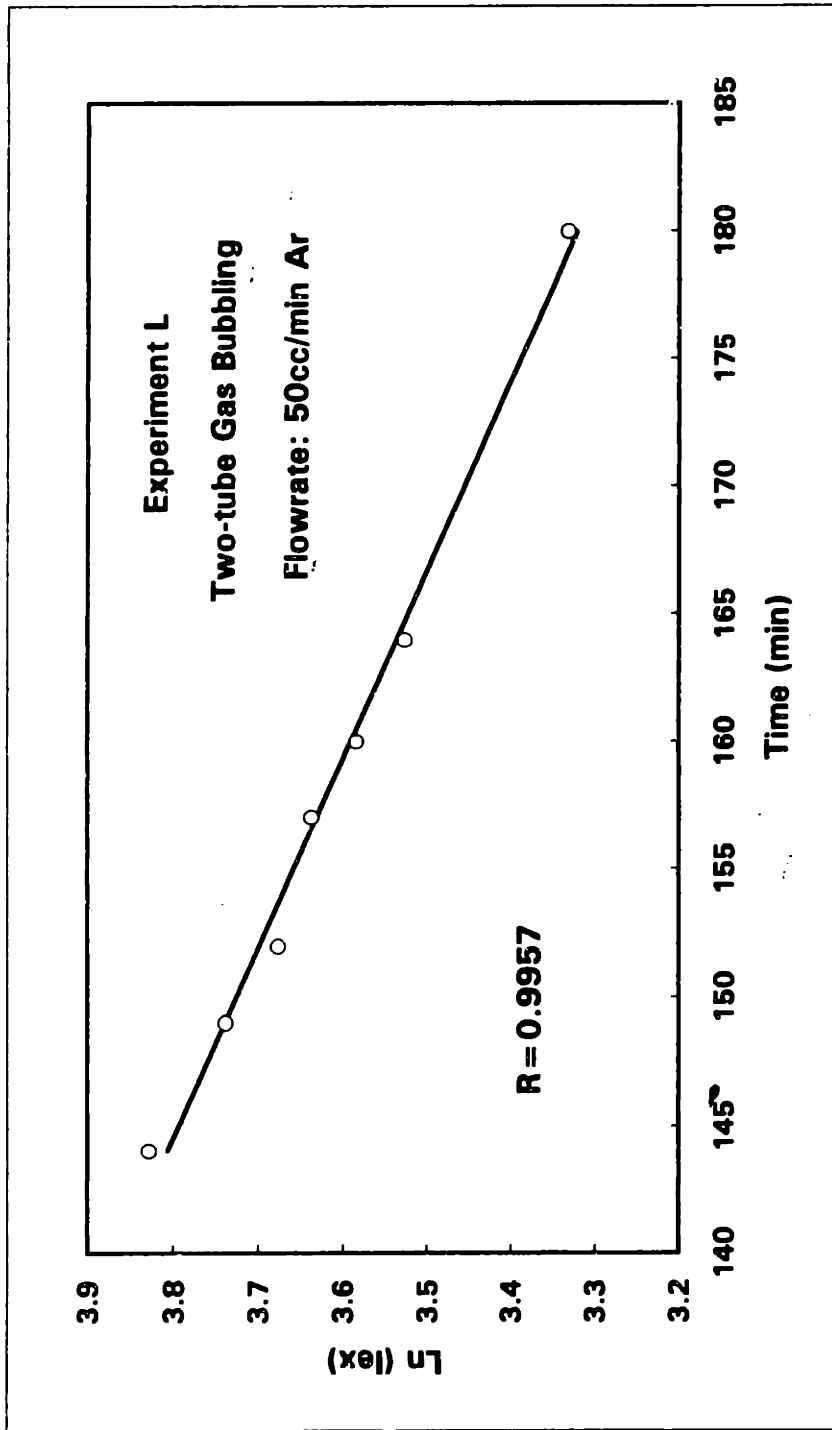
Figure VII-1   Iex   vs.   Time   for a Typical Two-tube Gas Bubbling Experiment
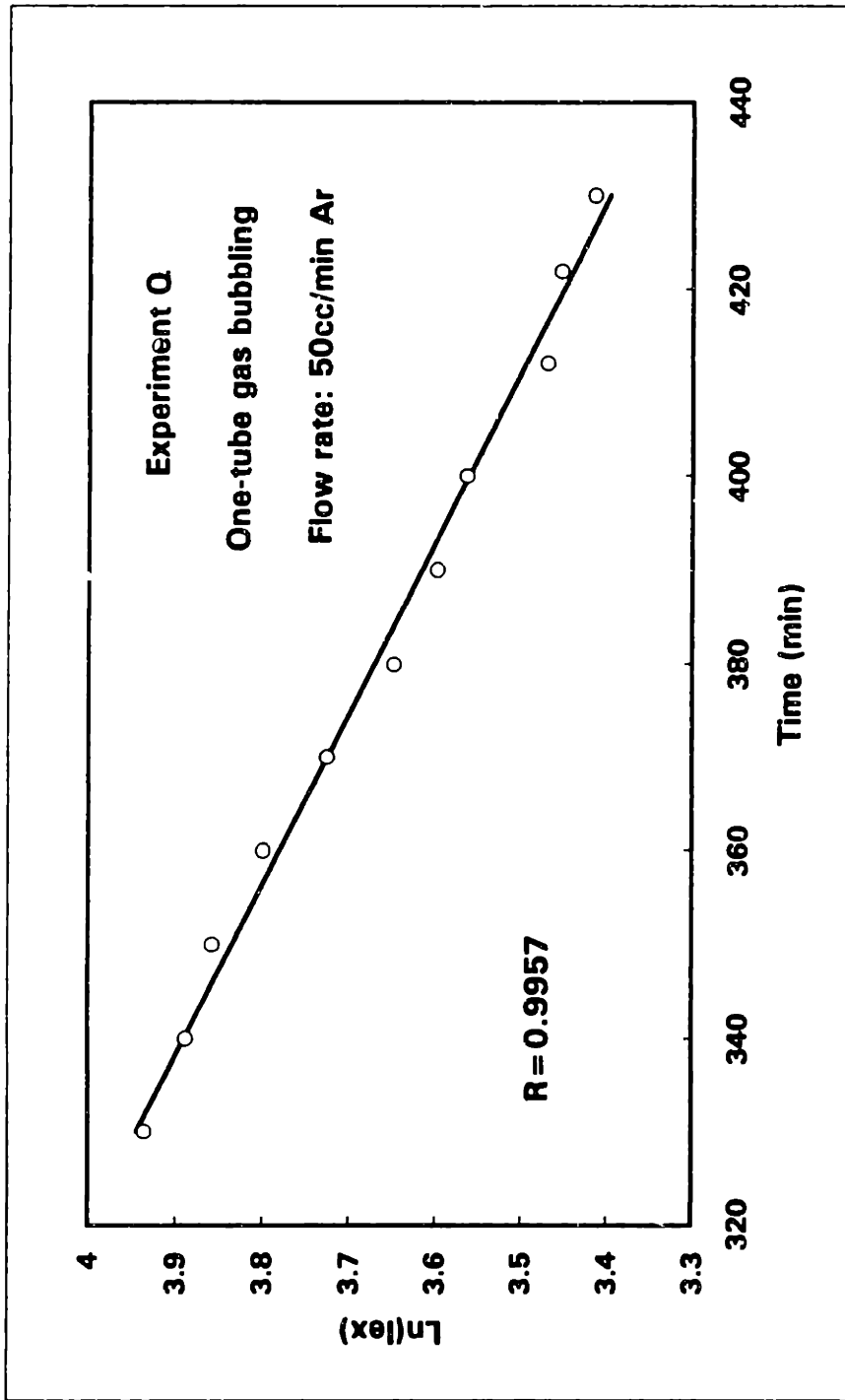
Figure VII-2   lex   vs.   Time   for a Typical One-tube Gas Bubbling Experiment
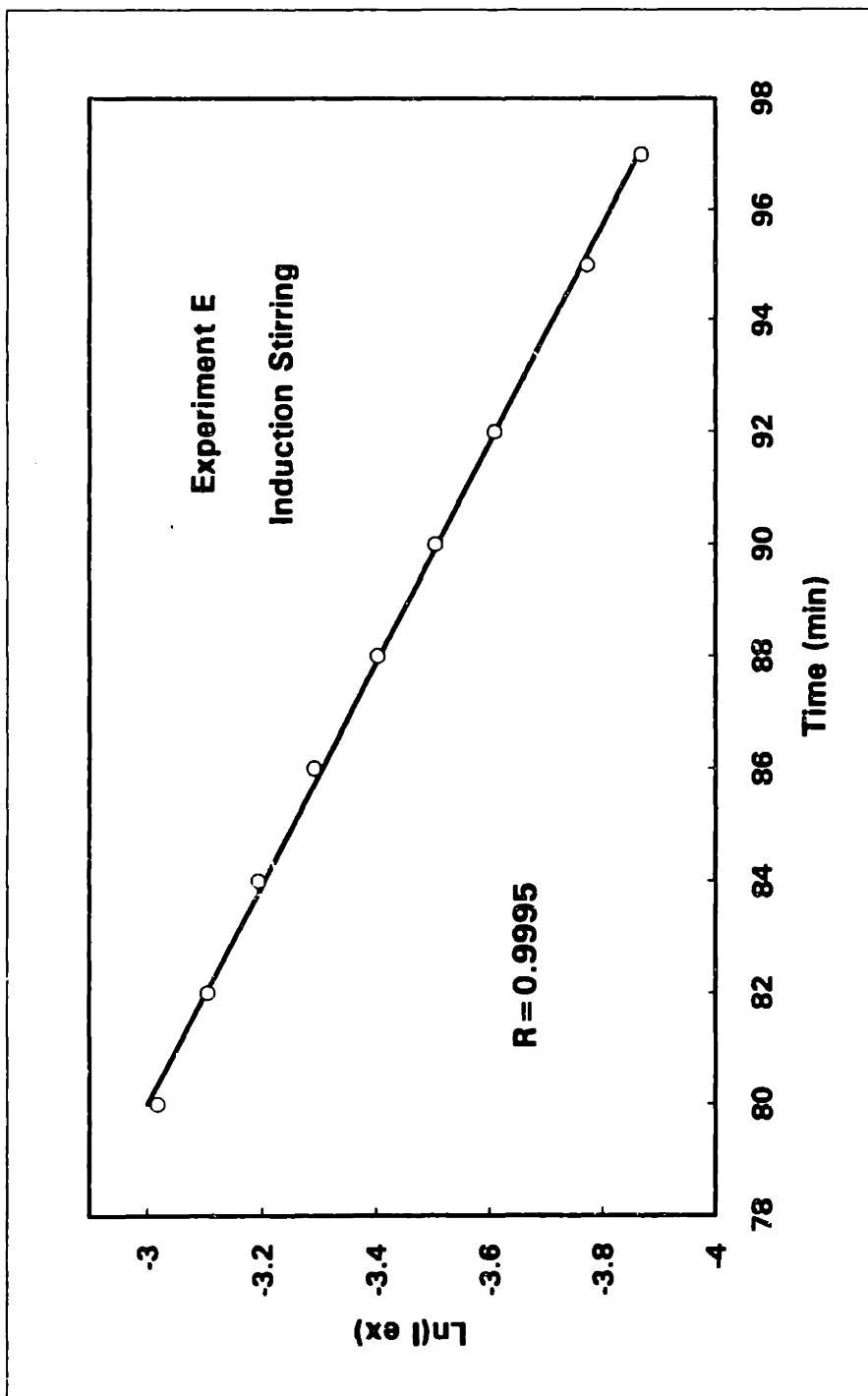
Figure VII-3   Iex   vs.   Time   for a Typical Induction Stirring Experiment
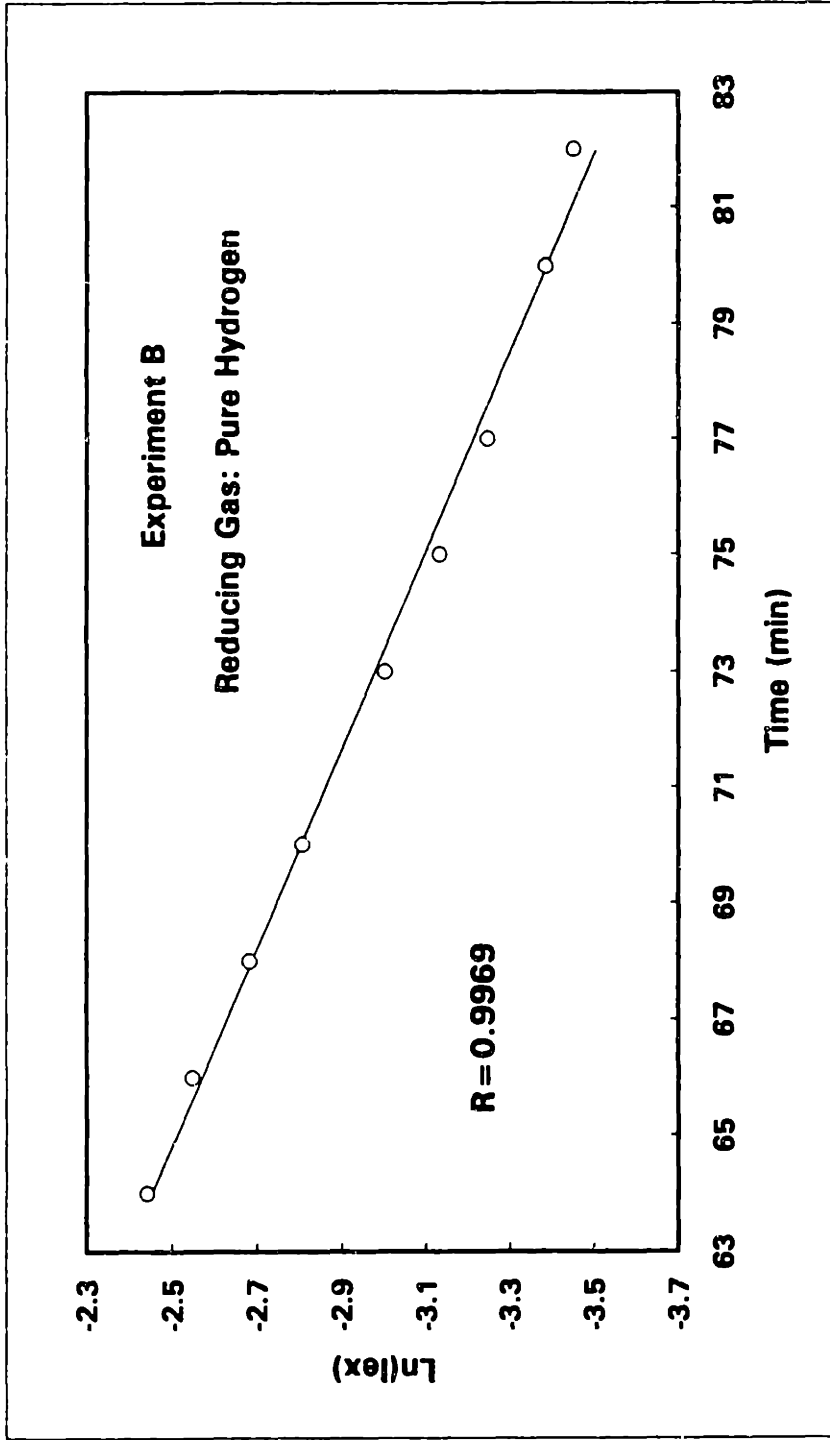
Figure VII-4 lex vs. Time for a Deoxidation Experiment Using Hydrogen
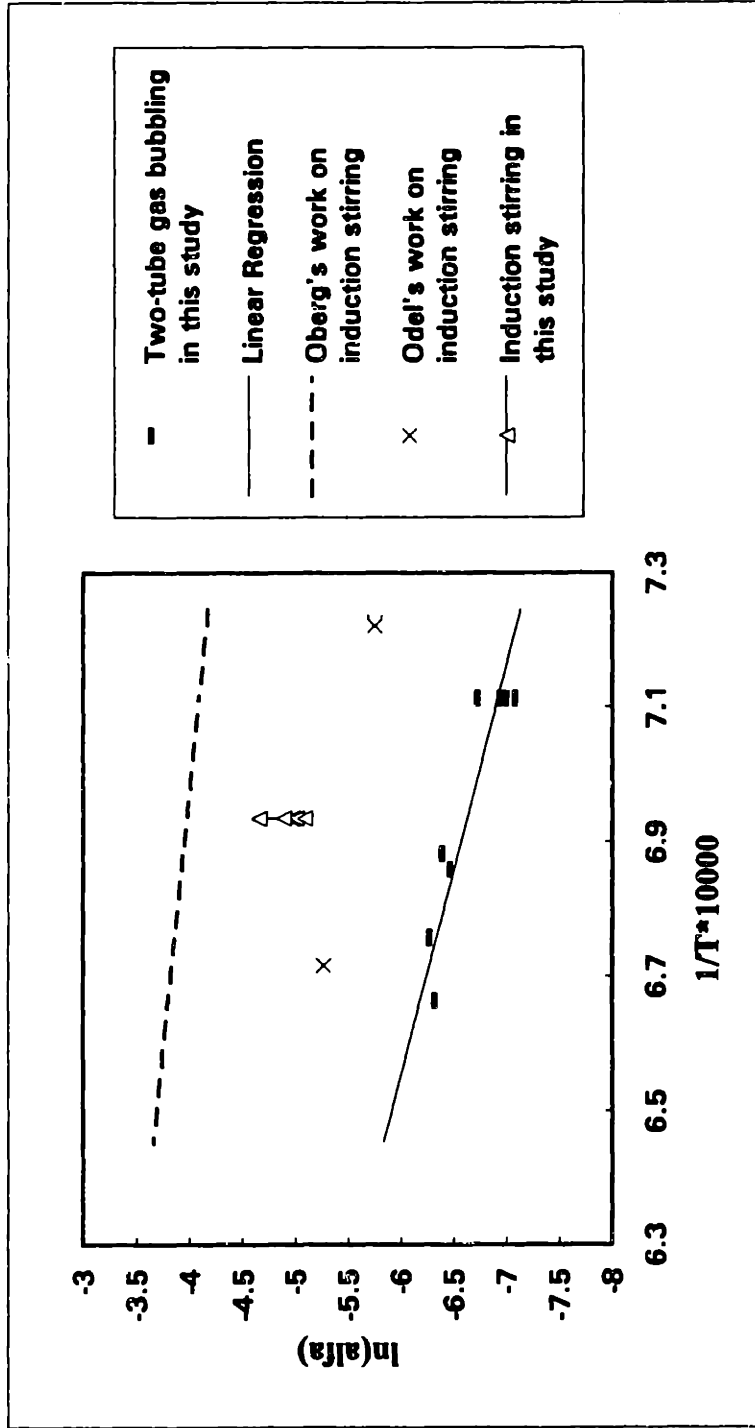
Figure VII-5   Dependence of Oxygen Mass Transfer Coefficient in Molten Copper on Temperature and Stirring Intensity
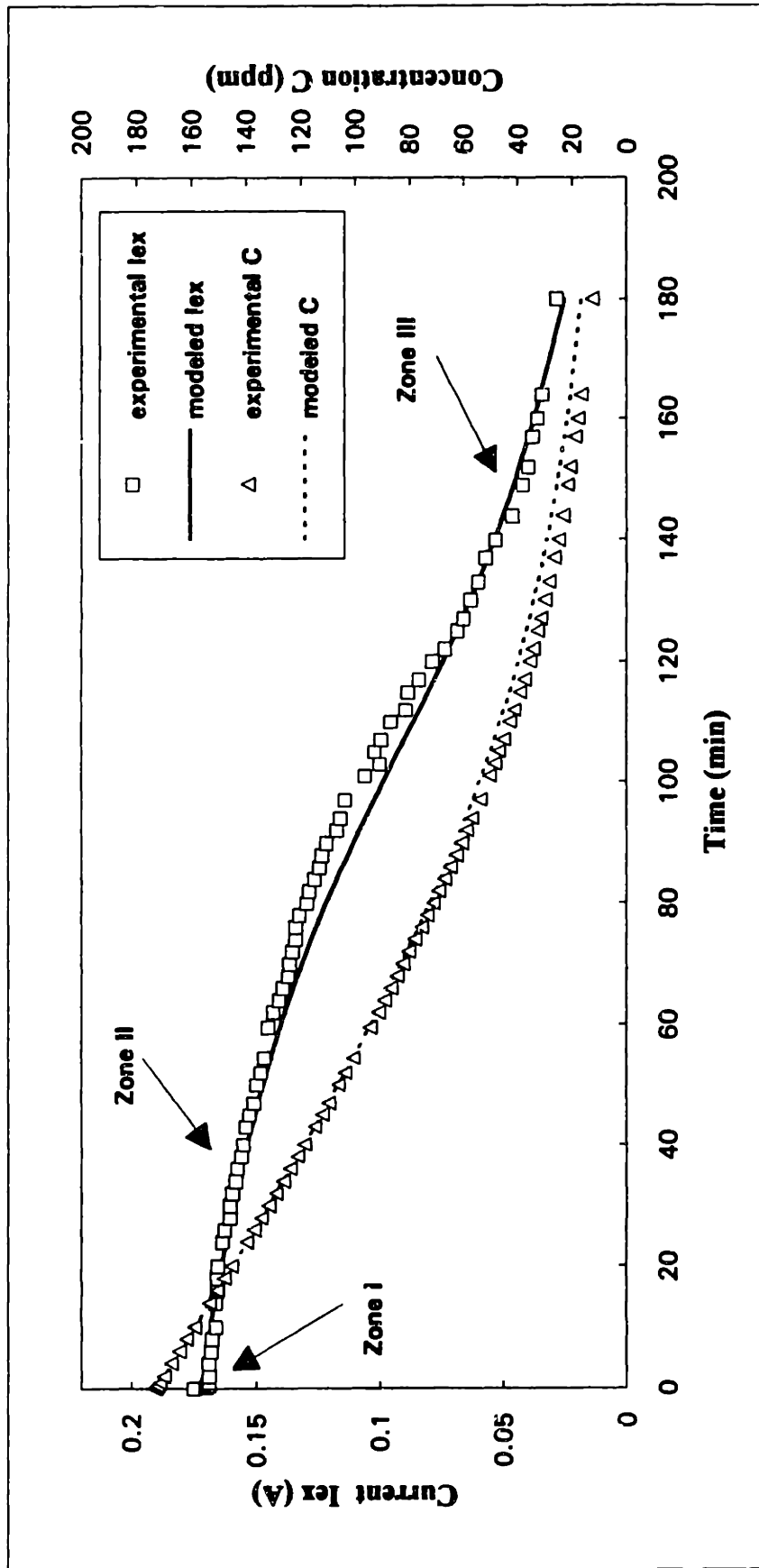
Figure VII-6 Modeled, Experimental Current and Concentration vs. Time for Experiment L
(Iex - external current; C - Concentration)
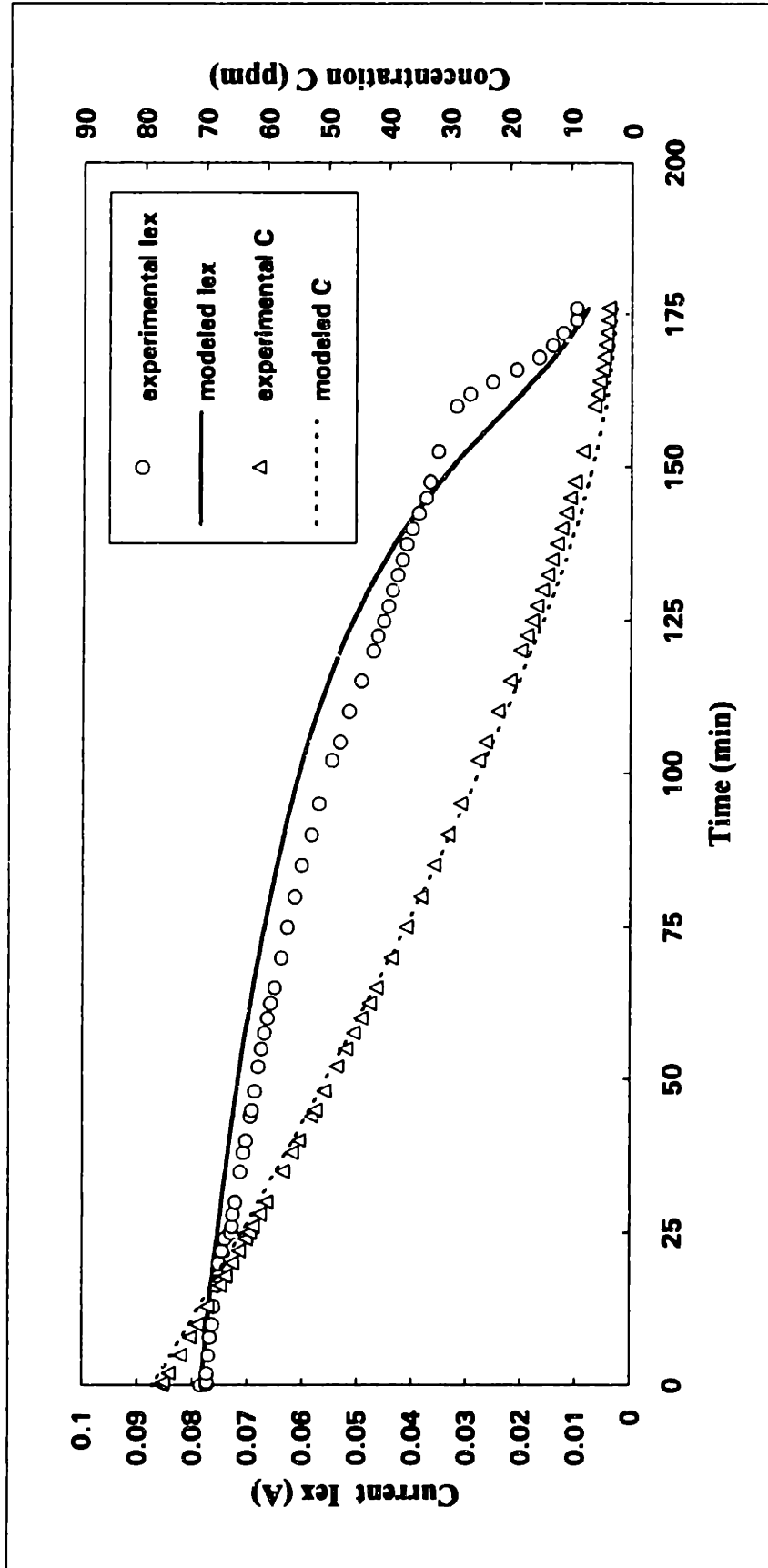
Figure VII-7 Modeled, Experimental Current and Concentration vs. Time for Experiment D
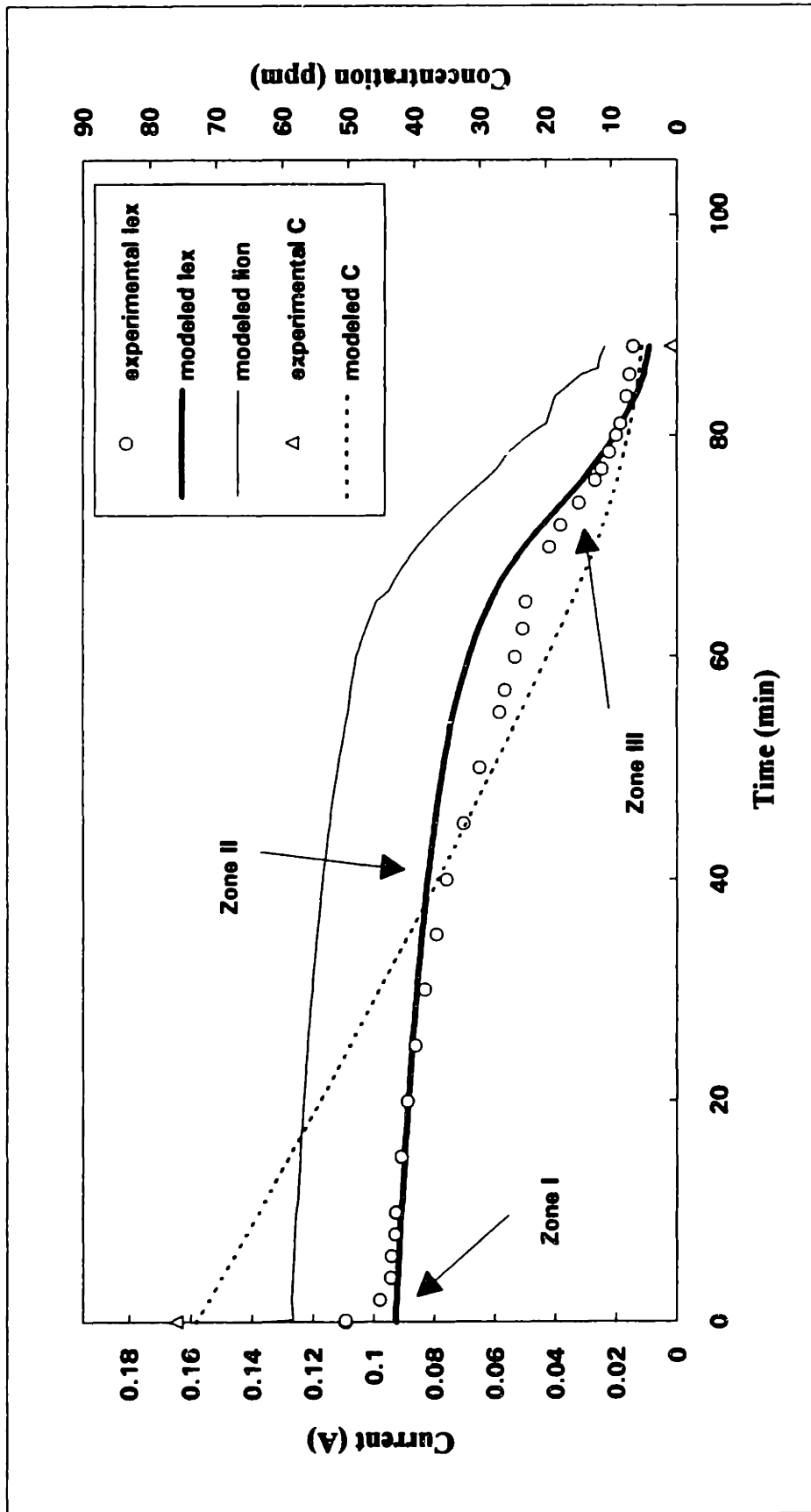
Figure VII-8 Modeled, Experimental Current and Concentration vs. Time for Experiment A (Iion - ionic current; Iex - external current, C - Concentration)
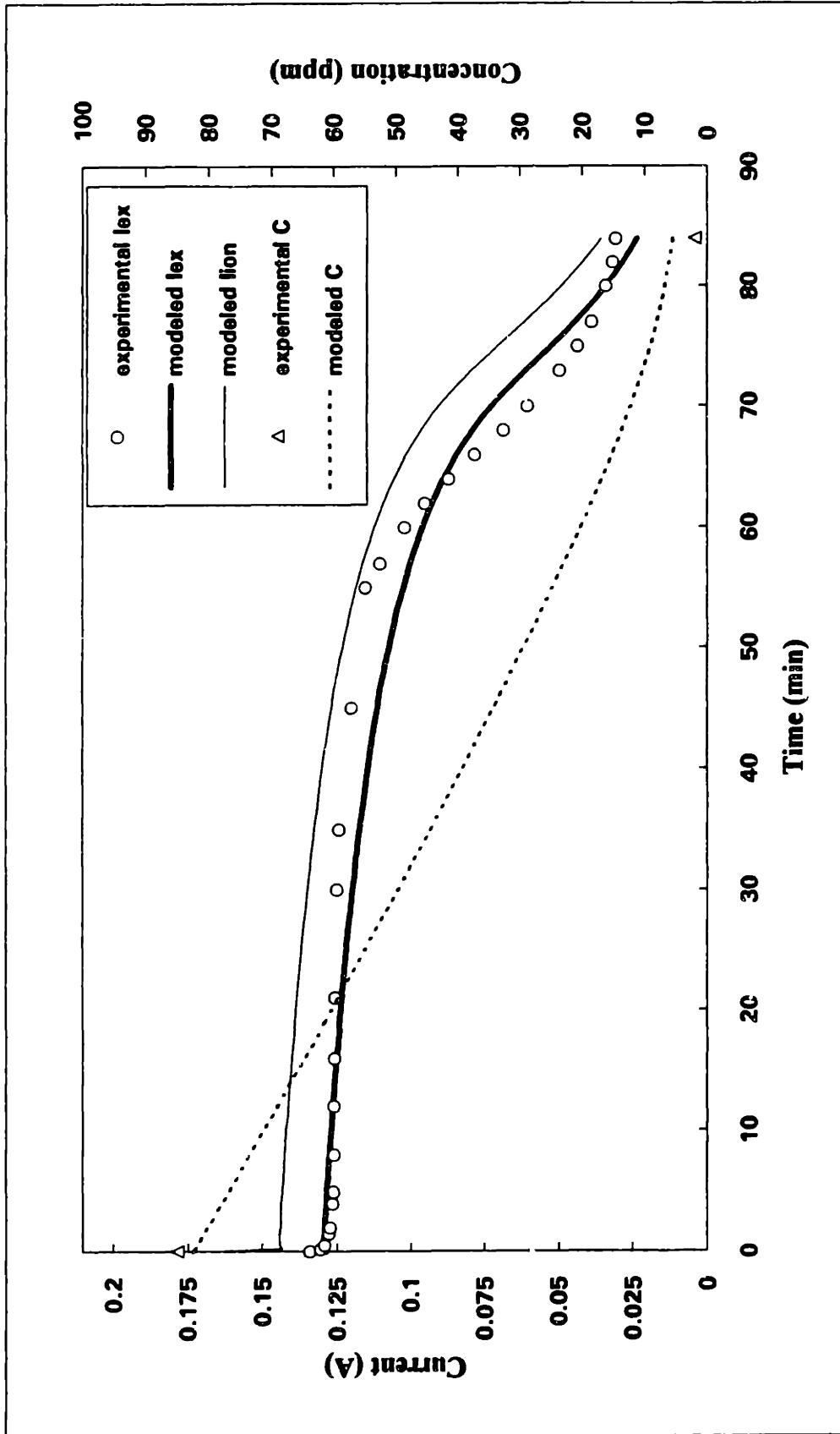
Figure VII-9 Modeled, Experimental Current and Concentration vs. Time for Experiment B

104

diffusion layer   C[i-1]   C[i]   C[i + 1]

outer wall of a zirconia tube

boundary between the diffusion layer
and the bulk of the melt
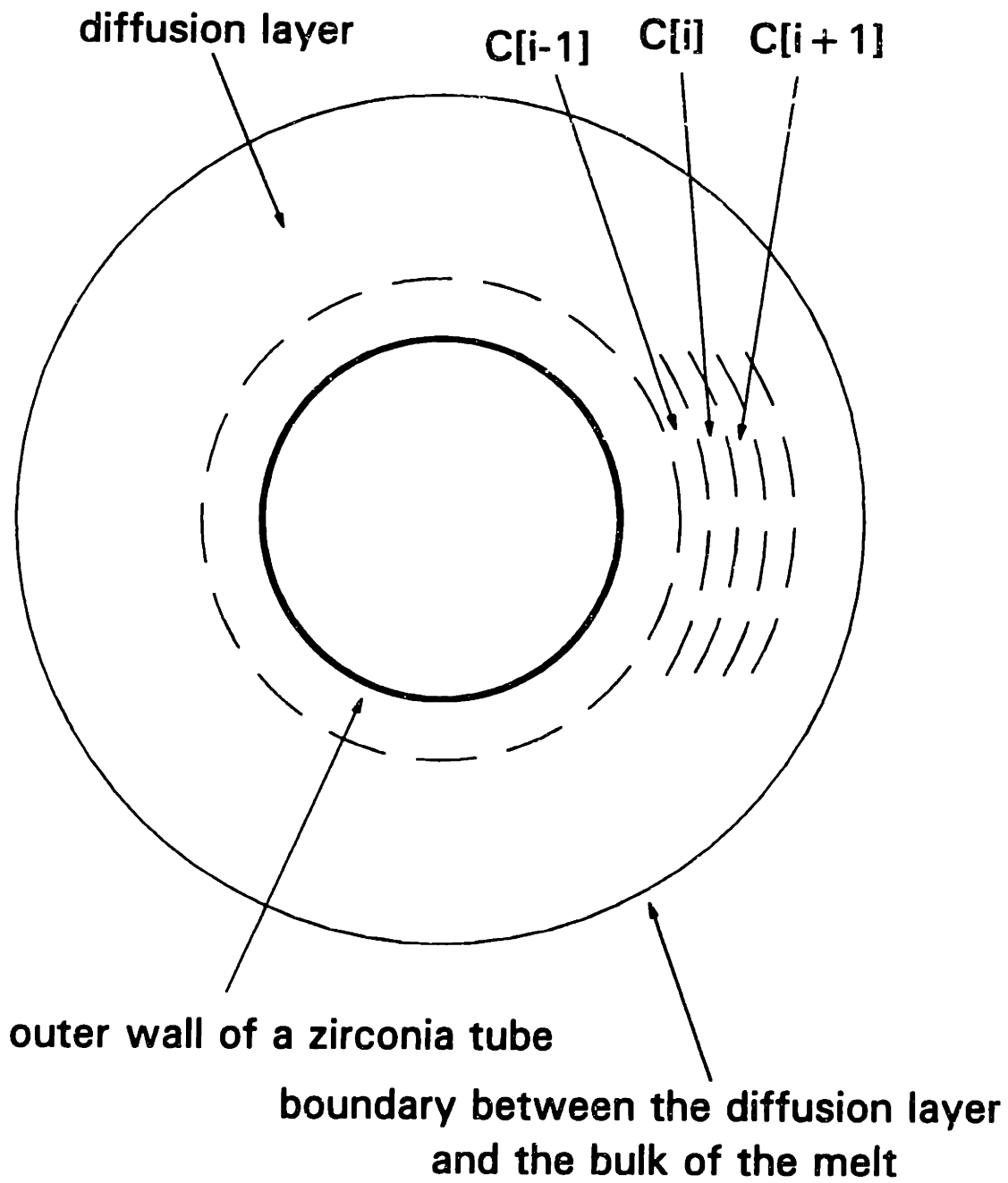
Figure VII-10   Finite Elements in Diffusion Layer
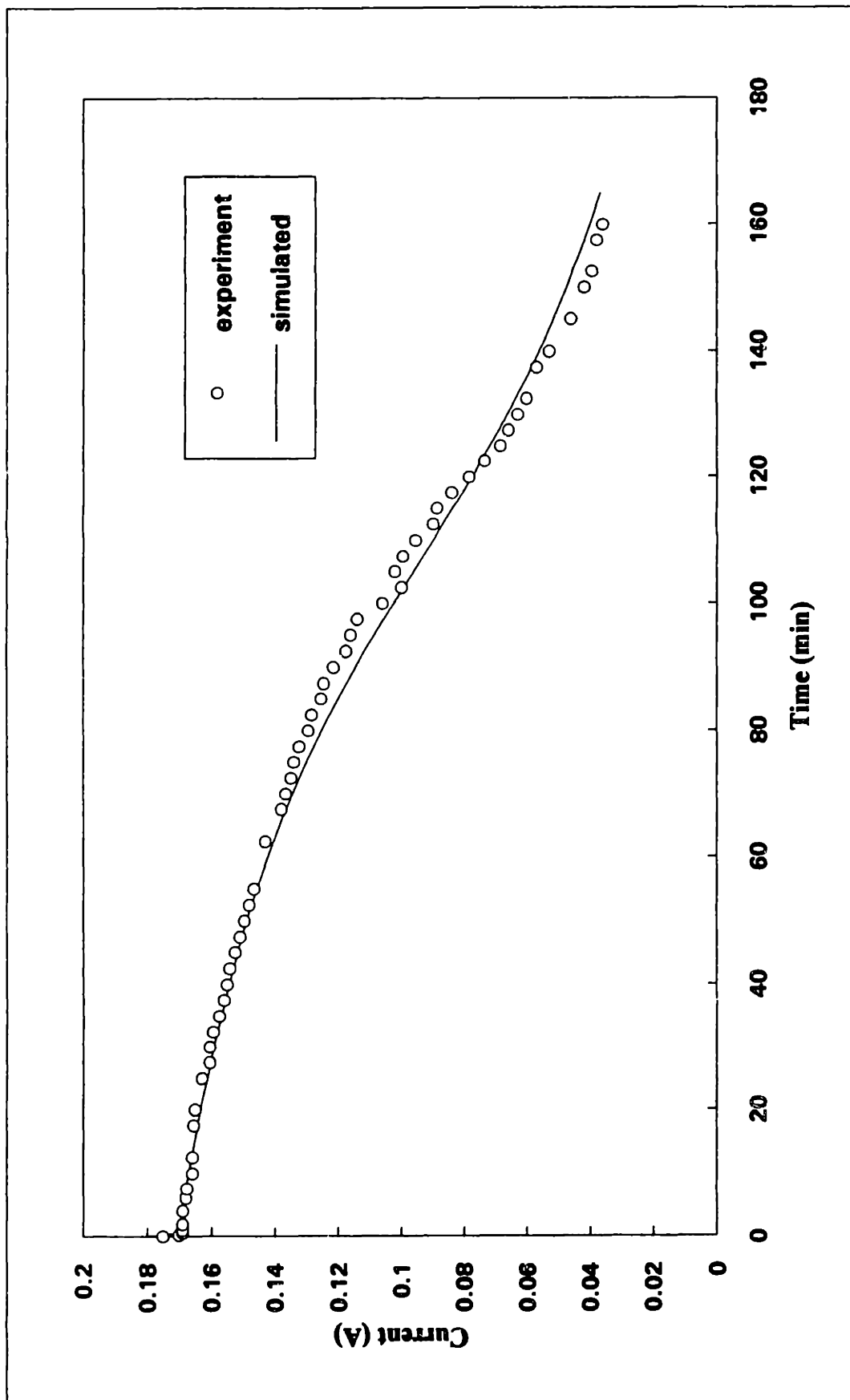
Figure VII-11 Experimental, Simulated Interfacial Concentration and Deoxidation Current vs. Time for Experiment L
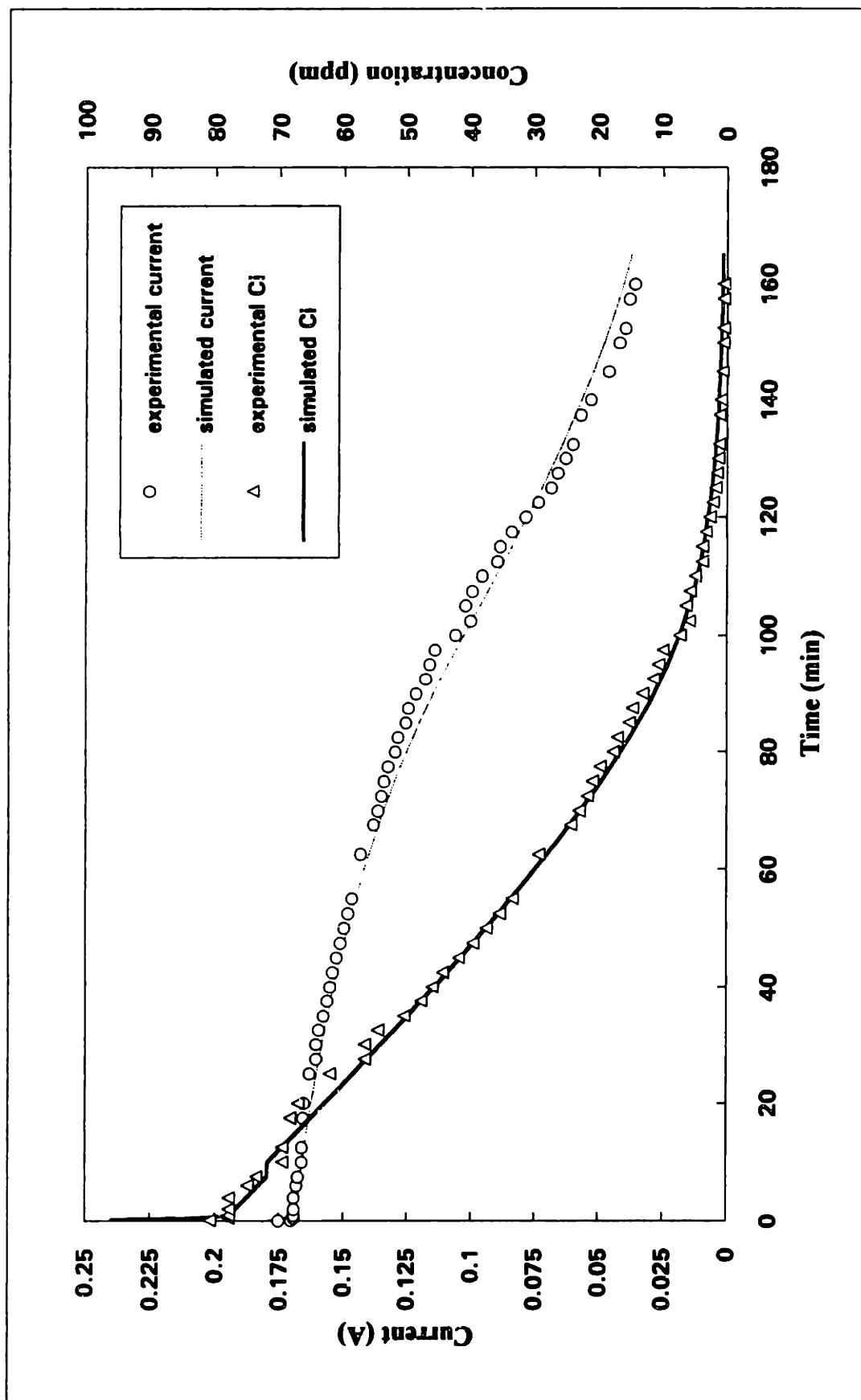
Figure VII-12 Experimental, Modeled Interfacial Concentration and Deoxidation Current vs. Time for Experiment L
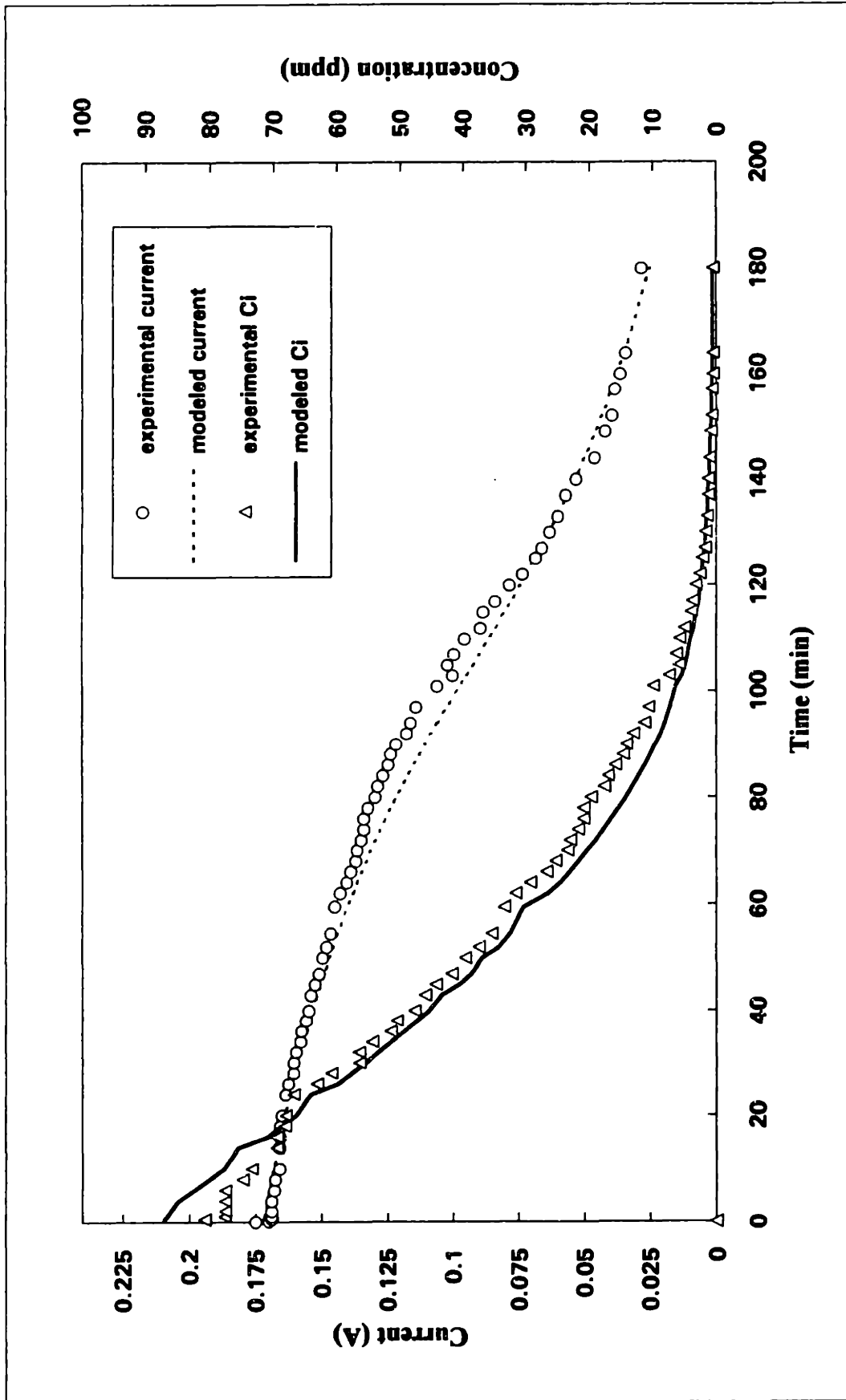
Figure VII-13 Experimental, Modeled Interfacial Concentration and Deoxidation Current vs. Time for Experiment L
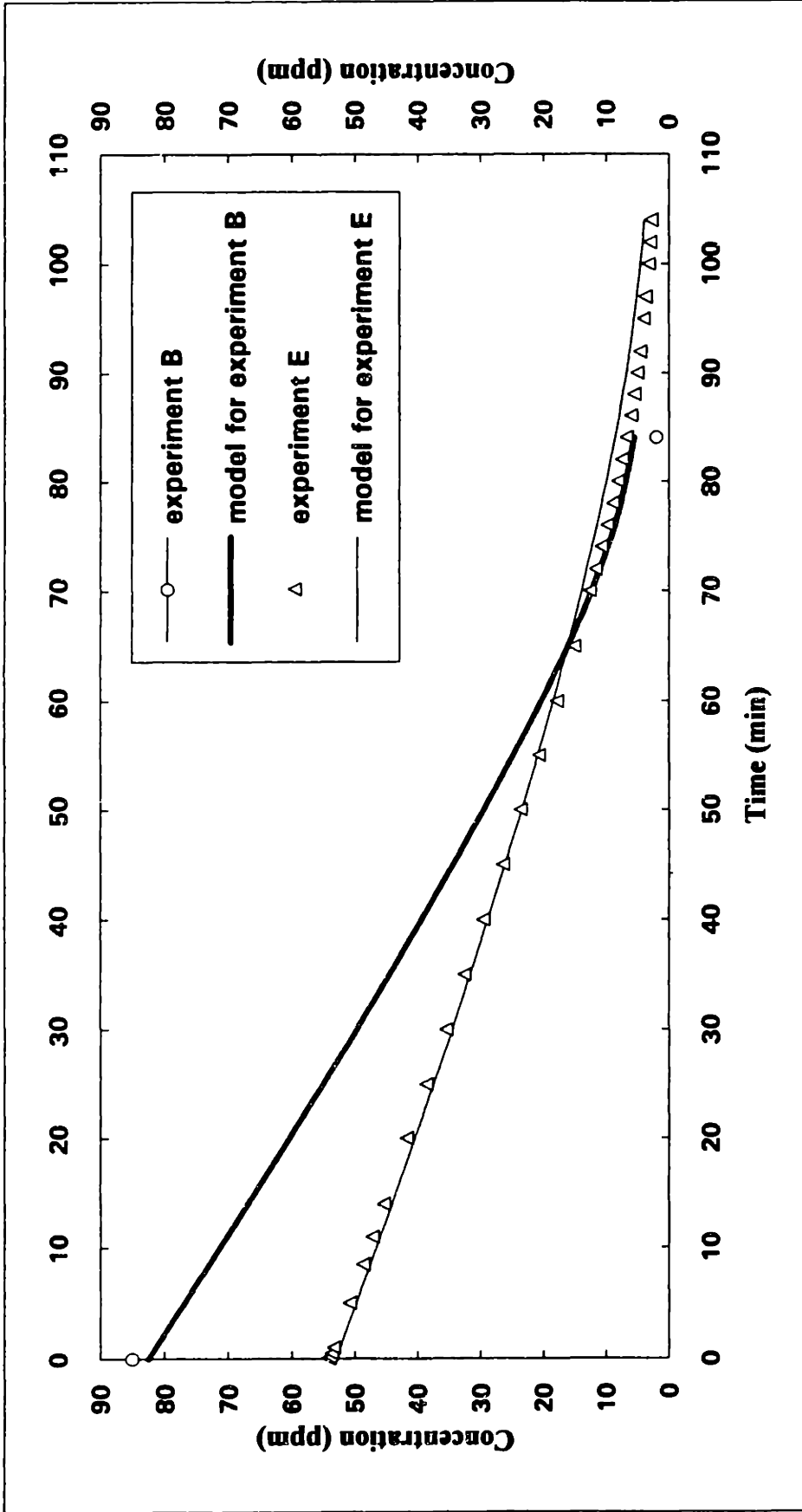
Figure VII-14 Comparison between Deoxidation Experiments Using Different Reducing gases

109
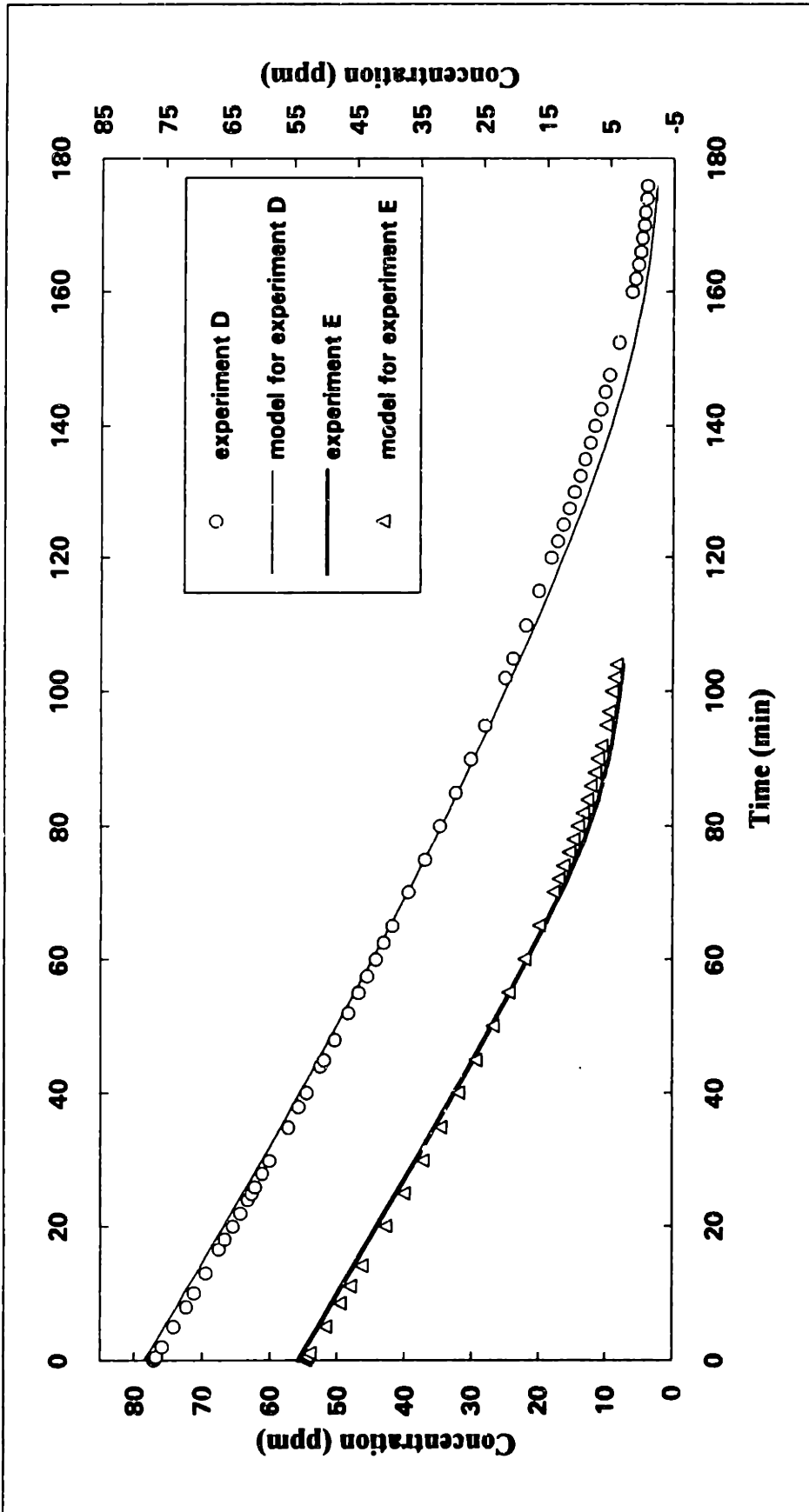
Figure VII-15 Comparison between Deoxidation Experiments with Different Flowrates of Reducing Gases
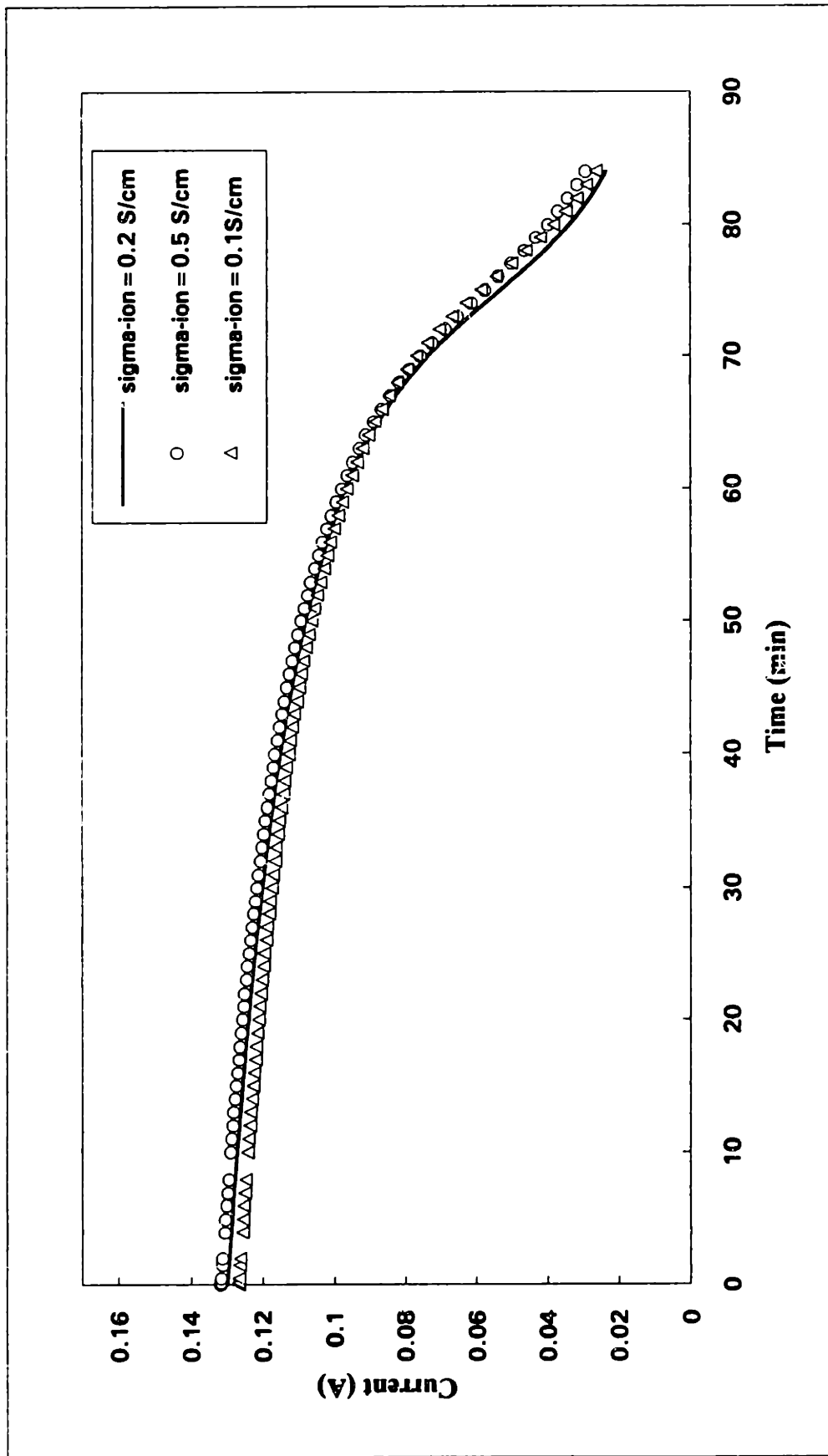
Fig. VII-16 Sensitivity test for the ionic conductivity of the electrolyte
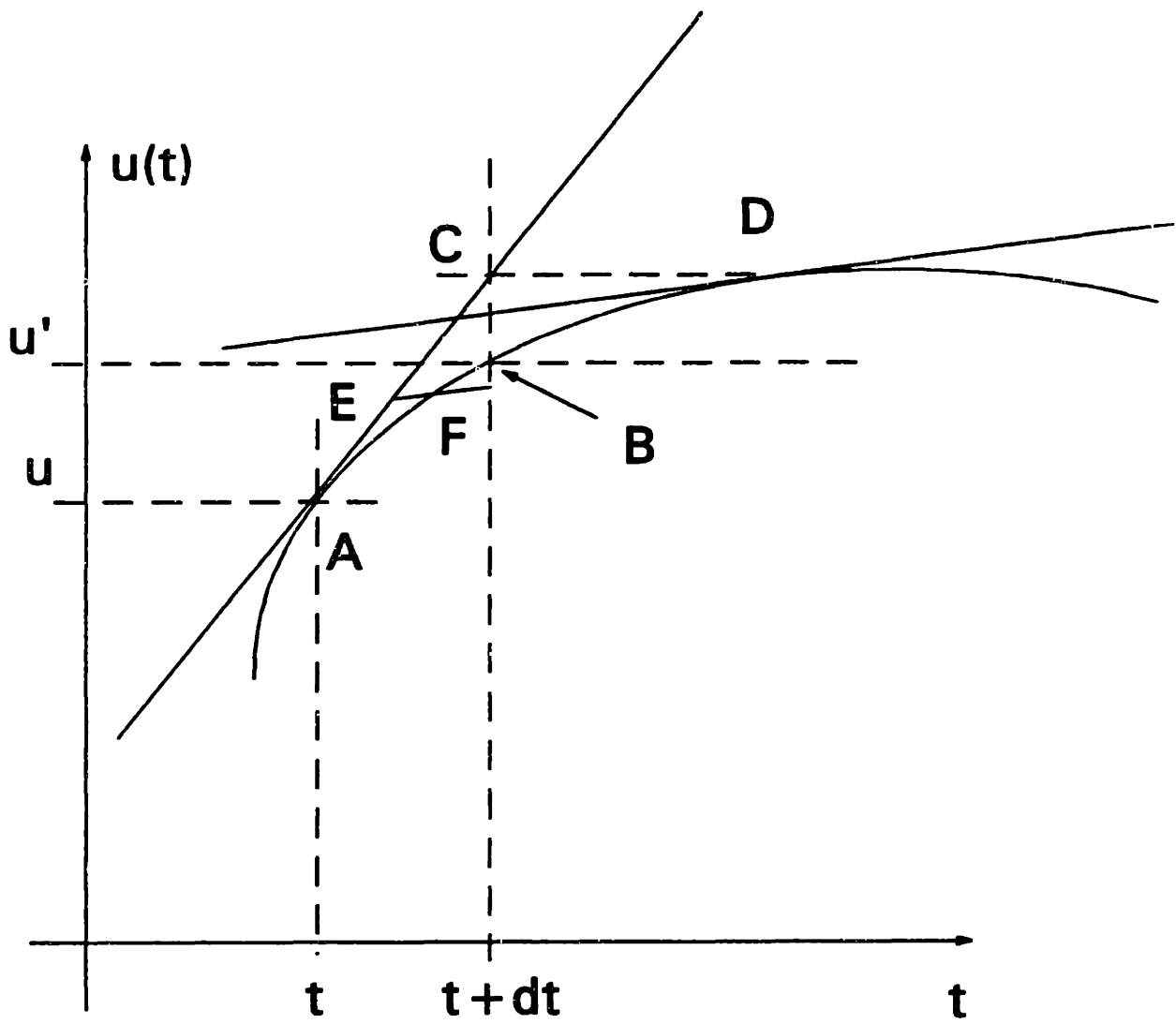
Fig. VII-17 Schematic explanation of Runge-Kutta Integration (RKI)

Table VII-1 Some Deoxidation Experimental Parameters and Calculated Mass Transfer Coefficients

expt.	weight of Cu melt (kg)	type of reducing gas	initial oxygen (ppm)	electrode/ electrolyte interfacial area (cm^2)	Temperature (K)	flow rate (cc/min)	R_{total} (Ω)	stirring method /bubbling tubes	mass transfer coefficient α (cm/s)
A	0.667	H_2	76	12.1	1442	245	5.5	Induction stirring	7.01×10^{-3}
B	0.638	H_2	85	11.6	1442	245	4.0	Induction stirring	6.70×10^{-3}
C	0.7	$5\%H_2$–N_2	290	12.7	1442	120	4.0	Induction stirring	7.53×10^{-3}
D	0.66	$5\%H_2$–N_2	77	12.0	1442	245	4.63	Induction stirring	9.54×10^{-3}
E	0.638	$5\%H_2$–N_2	54	10.8	1442	245	3.84	Induction stirring	6.2×10^{-3}

F	0.6	$5\%H_2\text{--}N_2$	63	13.9	1501	120	3.0	bubbling (two tubes)	1.80×10^{-3}
G	0.6	$5\%H_2\text{--}N_2$	68	13.9	1458	120	2.5	bubbling (two tubes)	1.56×10^{-3}
H	0.6	$5\%H_2\text{--}N_2$	43	13.9	1453	120	6.7	bubbling (two tubes)	1.86×10^{-3}
I	0.6	$5\%H_2\text{--}N_2$	61	13.9	1480	120	6.9	bubbling (two tubes)	1.89×10^{-3}
J	0.6	H_2	540	13.9	1406	120	3.1	Bubbling (two tubes)	8.38×10^{-4}
K	0.6	H_2	225	13.9	1406	120	2.5	Bubbling (two tubes)	9.73×10^{-4}
L	0.6	$5\%H_2\text{--}N_2$	173	13.9	1406	120	2.6	Bubbling (two tubes)	1.2×10^{-3}
M	0.6	H_2	251	13.9	1406	120	2.7	Bubbling (two tubes)	9.1×10^{-4}

N	0.581	H_2	274	13.7	1429	120	3.0	Bubbling (one tube)	4.6×10^{-4}
O	0.6	H_2	213	13.7	1406	120	2.9	Bubbling (one tube)	5.0×10^{-4}
P	0.4	H_2	63	24.6	1406	120	6.0	Bubbling (one tube)	4.1×10^{-4}
Q	0.556	$5\%H_2$--N_2	244	12.7	1423	120	5.8	Bubbling (one tube)	5.0×10^{-4}

Constant Experimental Parameters for Bubbling Stirring:

Flow rate of reducing gas--120ml/min.   Flow rate of Ar--50ml/min.

Bubbling tube ID=0.62×10^{-2}m $\rho_{melt} = 7.98 \times 10^3$ kg/m^3

Constant Experimental Parameters for Induction Stirring:

Flow rate of Ar--120ml/min.

115

Table VII-2 Current Range and Time Period of Linear Regression

Experiment	Current range (mA)	Time period (min)	R	Experiment	Current range (mA)	Time period (min)	R
A	49.8-14.4	65-88	0.9869	J	74.0-24.0	370-495	0.9828
B	87.1-30.8	64-84	0.9969	K	106.0-26.0	107-180	0.9846
C	56.8-22.0	418-434	0.9854	L	66.0-28.0	127-180	0.9957
D	29.5-10.0	162-176	0.9923	M	74.0-28.0	110-330	0.9729
E	48.9-16.8	80-104	0.9995	N	74.0-9.5	92-130	0.9753
F	39.0-25.0	56-77	0.9925	O	63.0-53.0	105-115	0.9015
G	62.0-38.0	47.5-75	0.9818	P	45.6-39.5	14-28	0.9591
H	27.1-16	80-110	0.9908	Q	51.2-39.5	330-28	0.9957
I	13.4-11.3	124-132	0.9858				

VIII. DISCUSSION OF SCALE-UP

The development of an industrial process based on this laboratory study would involve addressing issues related to scale-up. As stated by Ibl[169], during scale-up, a process is more or less profoundly modified and accordingly the factors that need to be considered for this deoxidation scale-up are:

1) mass transfer

2) heat transfer

3) current distribution

4) impurity effect

It can be seen from eq.[VII-14] that the deoxidation kinetics is proportional to the interfacial area(A)/mass(M_{melt}) ratio. Generally, scaling up tends to decrease this ratio. For example, let us consider an electrolytic cell in the form of a cube of side a and containing equally spaced plate electrodes. The mass is proportional to its volume, i.e., to a^3, whereas the interfacial area is proportional to the area of the walls a^2. Therefore, if one increases the cell size a, the A/M_{melt} tends to shrink. The same situation is expected to exist for heat transfer, because the heat flux is proportional to the area of the surroundings, whereas the amount of heat is proportional to the mass of the melt.

As the molten metal is deoxidized, the voltage of the solid electrolyte cells down stream will be much smaller than upstream. This imbalance of voltage distribution will also cause an imbalance in current distribution. Also, for a laminar flow, the diffusion thickness increases with increasing distance from the leading edge. Accordingly the mass transfer coefficient and the diffusion limiting current will also vary along the interface.

The effect of impurities on the solid electrolyte cells may also be a concern. In industrial operations, molten copper will be no longer pure copper as used in the laboratory experiments. When oxygen concentration is calculated, the activity coefficient of oxygen will be no longer unity. Instead it should be calculated by taking into account the influence of other elements as discussed in chapter II. Besides, corrosion of the device

caused by impurities might also be a problem. Thermal shock is another factor which will affect the life of the electrolyte cells.

The above issues need to be addressed during scale-up of this deoxidation process. The following part will focus on designing a scale-up structure of solid electrolyte cells for improving the deoxidation kinetics.

In order to apply the refining technology to an industrial process, the kinetics must be improved to the extent possible using the deoxidation model in this study. Three key factors to consider during designing of the process and the solid electrolyte cell are:

a) The melt must have sufficient stirring intensity to give a reasonably high mass transfer coefficient of oxygen. A realistic value of the mass transfer coefficient in an industrial scale well stirred melt would be on the order of 10^{-4} m/s.

b) The resistance involved in short circuiting, R_{ex}, must be minimized. This can be effectively done by increasing the area of the electronic short circuit contact. Realistically, R_{ex} can be decreased such that it is of the same order as R_{ion}. This way R_{total} will also be of the same order.

c) If the process and design criteria mentioned in steps a) and b) are met, then our model predicts that the deoxidation process will be controlled by the mass transfer of oxygen in the melt. In other words the transport of oxygen through the electrolyte will be much faster that the transport through the melt to the melt/electrolyte interface. In this situation the deoxidation kinetics can be enhanced by designing an electrolyte structure which has a high A/M_{melt} ratio for a given mass of the melt.

Based on the criteria mentioned in steps a), b) and c), a prototype structure of a section of the solid electrolyte cell that was designed to conduct pilot plant deoxidation trials involving copper at "Reading Tube Corporation" [170] is shown in Fig. VIII-1. It consists of a series of stabilized zirconia plates with stabilized zirconia plugs such that only the alternate openings between the plates are closed by the plugs. Reducing gases would flow through the annular solid electrolyte structure encapsulated by the plug. A porous

Ni-ZrO$_2$ cermet electrode would be deposited along the walls of the solid electrolyte plates that will be exposed to the reducing gas. For deoxidizing a melt, the structure would be immersed in the melt and the melt will rise in between the open ended zirconia plates. The short circuit contact will be established as shown Fig. VIII-1. The contact materials would be either carbon, electronic refractory or an inert metal.

The structure shown in Fig. VIII-1 can be considered to consist of several solid electrolyte cells with copper melt present in the space between the cells. In order to compare the performance of this structure with the less sophisticated lab cell, each of the cells can be considered to be exposed to around 0.5 kg of copper melt (similar to what has been used in this study). This would mean that the length of each cell unit has to be around 0.15m. In such a cell, R_{ex} and R_{ion} would be on the order of 10^{-2} ohms and the ratio of A/M around 0.06 m^2/kg. If hydrogen is passed through each cell at a flow rate of 0.3 l/min and the copper melt is maintained at 1473K, the deoxidation kinetics predicted by the model presented in this study is shown in Fig. VIII-2. This indicates that the kinetics of such cell structures are quite favorable for industrial application and a scale up would involve increasing the length and/or the number of these cells. The real applicability however would depend on the cost and the life of these cells. Both of them are of course dependent on one another.

As discussed in chapter VII, in the lab scale experiments, the influence of the initial oxygen partial pressure on the deoxidation kinetics is noticeable while that of the flowrate of reducing gases can hardly be seen. For a scale-up structure, the situation will be different. The calculation shows that, due to a larger deoxidation current, the oxygen partial pressure will greatly deviate from its initial value. Therefore the influence of the initial oxygen partial pressure is much smaller than that shown in Fig. VII-14. On the other hand, the influence of the reducing gas flowrate will be larger than that shown in Fig. VII-15. Based on the model discussed in chapter VII and the structure shown in Fig. VIII-1, the oxygen concentration vs. time is shown in Fig. VIII-2. It can be seen that by increasing

the flowrate of the reducing gas from 0.3 l/min to 1 l/min, the deoxidation time can be decreased by around 10-20 percent. In the above calculation, the reducing gas is assumed to be hydrogen. The calculation also shows that, for different initial oxygen partial pressure, the deoxidation kinetics does not change much. Those are very useful results since in commercial use, it will be much easier to have an atmosphere that is not highly reducing. Also, it means that, after the reducing gas flowrate reaches a certain level, it does not pay to further increase the gas flowrate. Based on economic considerations, for copper deoxidation a temperature of 1473K and hydrogen flowrate of 0.3 l/min are considered suitable for scale-up purpose.
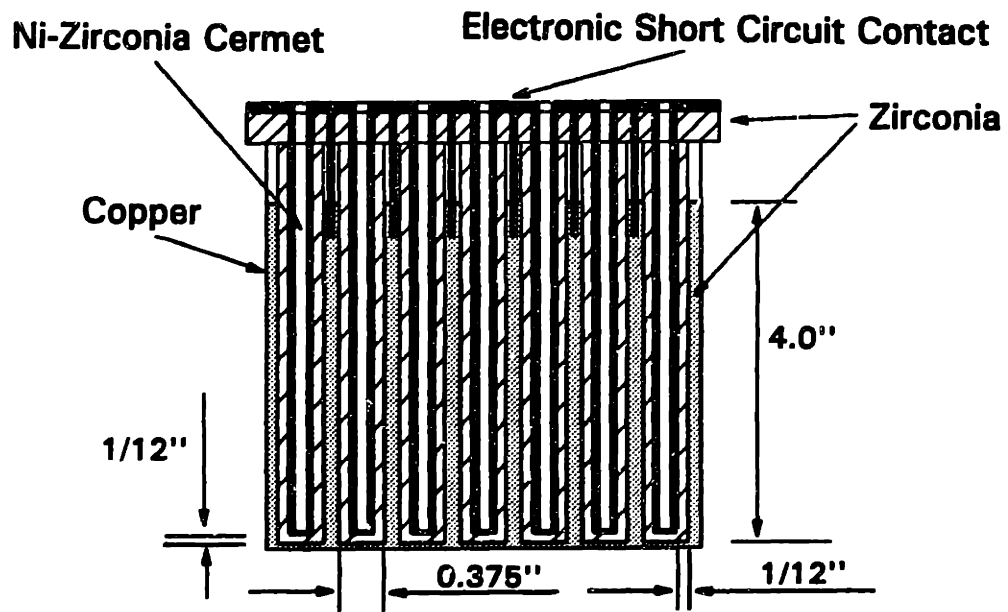
Figure VIII-1   Schematic of the Scale-up Structure
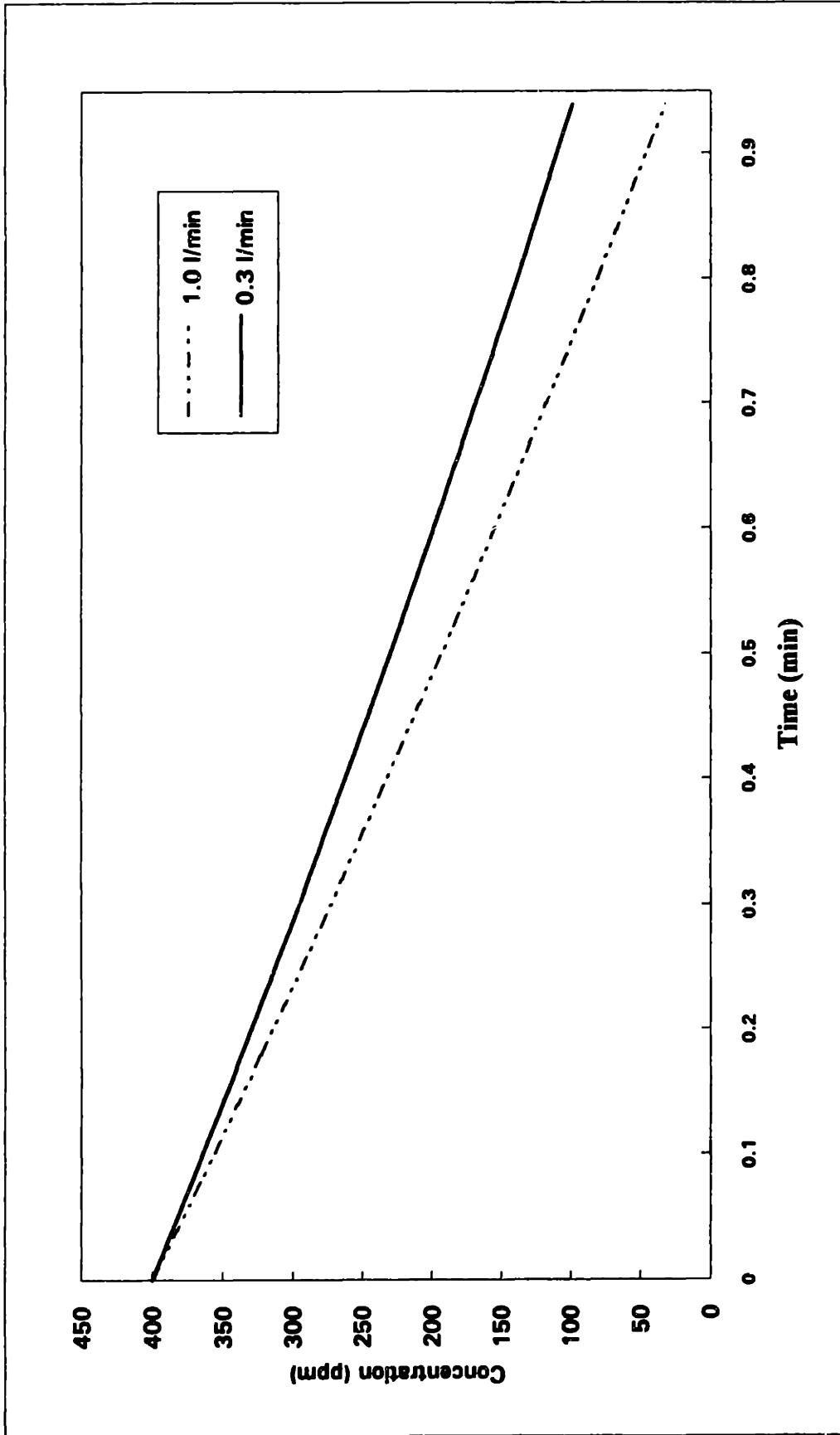
Figure VIII-2 Predicted Concentration vs. Time Curve for the Scale-up Stucture

IX. SUMMARY AND CONCLUSION

The galvanic deoxidation of molten copper employing inexpensive electrode materials was demonstrated to be feasible in this study. In a typical deoxidation experiment, a yttria stabilized zirconia tube, on the inner wall of which a layer of porous Ni-zirconia cermet electrode was deposited, was dipped into the molten copper, and a reducing gas was flushed into the interior of the zirconia tube. The molten copper was deoxidized by short circuiting the anode, Ni-zirconia cermet electrode, and the cathode, the molten copper.

A new fabrication technique to deposit Ni-zirconia cermet electrode was developed in this study. This technique involves nickel slurry coating, first sintering, zirconia suspension infiltration, and second sintering. The porosity of the cermet was accurately measured using an Archimedean technique which is different from the conventional methods. The electrodes were shown to have high porosity, low sheet resistance and long term stability.

By taking into account both external load and electronic conductivity, a general formula was derived to describe the transport of oxygen ions in the stabilized zirconia. The oxygen flux calculated from the formula was compared with that from an equivalent circuit. Based on the formula, the validity of the equivalent circuit was evaluated. It was found that, by assigning an appropriate value to the equivalent electronic resistance in the equivalent circuit, it is acceptable to use the equivalent circuit to describe the transport phenomena in the stabilized zirconia with an error of around 5%. The equivalent electronic resistance is a function of the oxygen partial pressure gradient to which the electrolyte is exposed.

The kinetics of the galvanic deoxidation was studied systematically. By examining each step involved, the rate-limiting steps of the deoxidation process were identified to be the mass transfer of oxygen in the molten copper and the transport of oxygen ions through

the electrolyte. A general model was proposed to describe the deoxidation process. The model was solved first in a simplified way and then numerically.

Based on the solution of the simplified model, a new technique to calculate the mass transfer coefficient of oxygen in the molten copper from the deoxidation current was proposed. The mass transfer coefficient of oxygen in the molten copper was measured as a function of stirring intensity and temperature. It was found that the mass transfer coefficient of oxygen in the molten copper under induction stirring was one order of magnitude higher than stirring with argon at 50ml/min, and temperature has a marginal effect on the mass transfer coefficient of oxygen.

The deoxidation was modeled as a function of temperature, short circuit resistance, flow rate of the reducing gases, electronic and ionic conductivity of the electrolyte, and mass transfer coefficient of oxygen in the molten copper. The external current, the ionic current, and the interfacial oxygen concentration between the electrolyte and the molten copper were modeled. It was found that the deoxidation process could be divided into three zone: in zone I both the deoxidation current and the interfacial oxygen concentration drops very fast; in zone II the decrease of the current is leveled and the interfacial concentration drops at a constant rate; zone III is characterized by a very small interfacial oxygen concentration and an exponential decay of the deoxidation current.

The influence of the initial oxygen partial pressure in the reducing gas and the flow rate of the reducing gas on the deoxidation kinetics was evaluated. It was found that, when the deoxidation current was small, the effect of the former is more noticeable than that of the later.

Based on the model used in this study, a scale-up structure was proposed and its deoxidation capability was evaluated. It was found that the kinetics of the proposed cell structure is quite favorable for an industrial application.

124

APPENDICES

A.I. Computer Program

The program on the following page is written in C language (Microsoft C700) to simulate deoxidation processes.

The main part of the program contains seven subroutines which fulfill five functions:

1) the initialization of the parameters - subroutine "initialize"

2) the calculation of the concentration change in boundary layer - subroutine "media_step" and subroutine "layer". The introduction of subroutine "media_step" is due to the use of Runge Kutta Integration method.

3) the calculation of the boundary value for the simulation - subroutine "bulk" for the calculation of oxygen concentration in the bulk of melt and subroutine "boundary" for the calculation of oxygen concentration at the interface between electrolytes and metals

4) the calculation of the gas composition - subroutine "reference"

5) the swapping of data after the calculation for the time "t" and before the calculation for time "t+Δt" - subroutine "swap"

The data calculated from the simulation is stored to the file which is read by a spreadsheet software.

```c
# include<stdio.h>
# include<math.h>
#include <process.h>
                                        /*constants for program*/
# define no_step_int  23               /*number of elements*/
# define no_step_float 22.0            /* n step with (n+1) element*/
# define interval    0.05

# define radius 0.641                  /* OD 0.505 inch */
# define ini_c 1.73e+2                 /* experimental parameter */
# define temp 1406.0
# define time_total 48000.0           /* experimental time 9000s  */

# define flow_rate    0.12
# define No_oc        4.42e-5          /*initial content of oxygen atoms*/
# define R_total      2.35
# define mass_total   600.0
# define T_rm         298              /*room temperature*/
# define D_melt       7.98
# define Area        13.9
# define D_oxygen    6.8e-5            /*diffusitivity ofoxygen*/
# define thick_layer  5.8e-2           /*thickness of diffusion layer*/

# define Faraday      96485.0                   /*experimental constants*/
# define R_gas        8.314
# define Pi           3.1416
# define Molar_mass_O        16.0

    double C1[no_step_int], C2[no_step_int],delta[no_step_int], C_gas;
    double current, accum, accum_total, length_step, mass_unit, mass_bulk;

FILE *stream, *stream1, *stream2, *stream3;

main()
{
  long int i;
  int      j;

  double times;

  void initialize (void);
  void media_step (void);
  void bulk (void);
  void reference(void);
```

```c
void boundary (void);
void layer (void);
void swap (void);

initialize();
length_step=thick_layer/no_step_float;
times=time_total/interval;
mass_bulk=mass_total-Pi*((radius+thick_layer)*(radius+thick_layer)
        -radius*radius)*D_melt*(Area/2.0/Pi/radius);
/* height=Area/2/Pi/radius */

printf("%f  time\n", times);
 stream=fopen("y2","wt");
 stream1=fopen("y3","wt");


    for (i=1; i<=times; i++)
{
    media_step();

    boundary();        /*calculate the concentration
                        in boundary layer*/

bulk();
reference();
layer();
swap();

if (i==300 || i==24000 || i==470000)
    {
        for (j=0; j<=no_step_int-1; j++)
            {
                fprintf(stream1,"%f\n", C1[j]);
                }
        };


    if (i<=9000)
        { if (i%200==0)
        {
            fprintf(stream,"%f\n", current );

        printf("t= %fs    %f    %f    %f    %f      %f\n", interval*i, current,
                accum_total,C2[0], C2[no_step_int-1],delta[0]);
```

127

```c
            }
        }
        else
          {
            if (i%3000==0)
          {
            fprintf(stream,"%f\n", current );

            printf("t= %fs    %f    %f    %f   %f   %f\n", interval*i, current,
                        accum_total, C2[0], C2[no_step_int-1],delta[0]);

        }
    }
  }
  }
  fclose(stream);
  fclose(stream1);
}


    void initialize(void)
      {
        int i;
        accum=0.0;
        accum_total=0.0;
        C_gas=0.011;
        printf("%d\n", no_step_int);
        for (i=0; i<=no_step_int-1;i++)
            C1[i]=ini_c;
        printf("%f\n", C1[no_step_int-1]);
        return;
        }


    void media_step(void)
    {
        int j;

        for (j=1;j<=no_step_int-2;j++)
    {
        delta[j]=D_oxygen*interval*(C1[j+1]-2.0*C1[j]+C1[j-1]+length_step
            /2.0/(radius+j*length_step)*(C1[j+1]-C1[j-1]))
          /(length_step*length_step);
/*        printf("delta %f", delta[j]);        */
    }
        delta[0]=delta[1];
```

```c
            delta[no_step_int-1]=delta[no_step_int-2];
            return;
    }



    void boundary(void)
    {
    double media;
    current=R_gas*temp*log((C1[0]+delta[0])/C_gas)/(R_total*2.0*Farady);
    /*    printf("%f\n", current);    */
    media=current*Molar_mass_O*1.0e+6/(2.0*Farady*D_oxygen*Area*D_melt);
    /*  printf("%f\n", media);            */
            accum_total=accum_total+current*Molar_mass_O*1.0e+6*interval/
                    (2.0*Farady*mass_total);
            C2[0]=(48.0*(C1[1]+delta[1])-36.0*(C1[2]+delta[2])+16.0*(C1[3]+delta[3])
    -3.0*(C1[4]+delta[4])-12.0*media*length_step)/25.0;
    /*  5-point method    */

/*    printf("oo %f\n", C2[0]);                */
    /*    C1[0]=C2[0];        */
            return;
    }


    void reference(void)
    {
        double  Ks, Kp;

        Kp=exp(-(-246438+54.39*temp)/R_gas/temp);
        Ks=exp(-(-43200+10.6*temp)*4.184/R_gas/temp);
        C_gas=Ks/Kp*R_gas*T_rm/flow_rate*No_oc
                        +2*Ks/Kp*R_gas*T_rm/flow_rate*60/4/Farady*current;

    }



    void layer(void)
    {
        int j;
        double media1, media2, delta2;

        for (j=1; j<=no_step_int-2;j++)

        {
```

```c
                medial=j*length_step;
/*              printf("j %f", medial);          */


                media2=-2.0*(C1[j]+delta[j])+(C1[j-1]+delta[j-1])
                        +length_step/2.0/(radius+j*length_step)*
                ((delta[j+1]+C1[j+1])-(delta[j-1]+C1[j-1]));



        delta2=D_oxygen*interval*(((C1[j+1]+delta[j+1])+media2)/
                (length_step*length_step);
/*              printf(" delta2 %f", delta2);    */
                C2[j]=C1[j]+(delta2+delta[j])/2.0;
                }


                                /*      printf("layer  %f  %f  bulk  %f  %f\n",C2[0],
                C2[j],C2[no_step_int-2],C2[no_step_int-1]);    */
        return;
}


        void bulk(void)
        {

accum=accum+D_oxygen*Area/radius*(radius+thick_layer)*(25.0*(C1[no_step_int-
1]+delta[no_step_int-1])
                        -48.0*(C1[no_step_int-2]+delta[no_step_int-2])
                        +36.0*(C1[no_step_int-3]+delta[no_step_int-3])
                        -16.0*(C1[no_step_int-4]+delta[no_step_int-4])
                        +3.0*(C1[no_step_int-5]+delta[no_step_int-5]))/12.0
                                /length_step;



        C2[no_step_int-1]=ini_c-interval*D_melt*accum/mass_bulk;
/* printf("%f %f %f\n", C2[no_step_int-1], accum, C2[no_step_int-2]);  */


            return;
        }



        void swap(void)
        {
                int i;
                double p;
```

```
/*      float *r,*q;

     r=C1;
     q=C2;
     C1=q;
     C2=r;                */

     for (i=0;i<=no_step_int-1; i++)
       {
         C1[i]=C2[i];
/*  printf("t= %fs    %f    %f    %f    %f\n", current,
                accum_total, C2[0], C2[no_step_int-1]);        */

     /*    printf("%f", C1[i]);                              */
       }
       return;
     }

/*                                   */
```

A.II. Composition of Materials Used

A.II.A. Typical Composition of Copper Shots*

Element	Cu	Sn	P	Fe	Ni	Ag	Pb
wt%	balance	<0.001	<0.001	<0.0035	<0.0015	<0.0005	<0.0006
Element	Zn	Sb	As	Mn			
wt%	<0.003	<0.0003	<0.0001	<0.002			

*Composition analysis is provided by Johson Matthey.

A.II.B. Composition of Argon (AIRCO, Grade 5.0)*

Total Impurity	N_2	O_2	H_2O	Hydrocarbon
<10ppm	<4ppm	<1ppm	<1ppm	<1ppm

*Composition analysis is provided by AIRCO.

A.II.C. Composition of Quartz Crucibles*

Compound	SiO_2	FeO	Al_2O_3	CaO	MgO	Na_2O	Fe_2O_3	TiO_2
wt%	96.5	0.5	0.2	0.1	0.1	0.1	0.03	0.03

*Composition analysis is provided by Corning, Inc.

A.II.D. Composition of Zirconia Powder*

Compound	Y_2O_3	SiO_2	Al_2O_3	Fe_2O_3	Na_2O
wt%	13.16	<0.002	<0.005	<0.002	0.069

*Composition analysis is provided by TOSOH.

A.II.E. Composition of Ni Powder*

Compound	Ni	NiO	Ni_3C
wt%	97.9	0.3	1.6

*Composition analysis is provided by NOVAMET.

A.III. TYPICAL WORKSHEET FOR OXYGEN PARTIAL PRESSURE CALCULATION

A typical worksheet for the calculation of $Po_2'(O.C.)$ is shown on the next page.

The notations used in the worksheet are:

ETC(mV):   voltage reading of the thermocouple in the oxygen sensor

TC(^{o}C):   temperature of the oxygen sensor in Celcius degree, taking into account the correction of room temperature (25°C)

TKOS(K):   temperature of the oxygen sensor in Kelvin degree

EOS(V):   voltage reading of the oxygen sensor

deltaGOS(J): ΔG for the reaction at TKOS

$$H_2(g) + \frac{1}{2}O_2(g) = H_2O(g) \qquad \text{[A-III-1]}$$
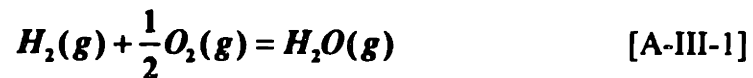
ΔG=-246,438+54.39*TKOS (J)

PO2OS(atm):   oxygen partial pressure calculated from Nernst equation

KpOS: equilibrium constant for the reaction [A-III-1]

PH2(atm):   hydrogen partial pressure in the reducing gas at TKOS

PH2O(atm):   water vapor partial pressure in the reducing gas at TKOS

TKEP(K):   temperature at which deoxidation experiments were conducted

deltaGEP(J): ΔG for the reaction [A-III-1] at experimental temperature

KpEP: equilibrium constant for the reaction [A-III-1] at TKEP

PO2EP(atm):   oxygen partial pressure in the forming gas at TKEP

C(ppm):   oxygen concentration from chemical analysis

Edevice(V):   the voltage reading of the device when melts were sampled

Cr-s(ppm):   oxygen concentration in equilibrium with the reducing gas calculated from Nernst equation

$$C = C_{r-s} \exp(\frac{2E_{device}F}{RT}) \qquad \text{[A-III-2]}$$

Ks(this study): Sieverts' constant calculated based on the data obtained in this study

$$C_{r-s} = K_S * \{PO2EP\}^{\frac{1}{2}} \qquad \text{[A-III-3]}$$

deltaGKs[135

135

171](J): ΔG for the reaction

$$\frac{1}{2}O_2(g) \rightarrow \underline{O}\,(melt)$$ [A-III-4]

ΔG=-90,374+22.175*TKEP (J) [1]

Ks: equilibrium constant for the reaction [A-III-4]

Table A-III-1   A Typical Worksheet for Calculation of Oxygen Partial Pressure in Reducing Gases

ETC(mV)
8.35 $\Rightarrow$ TC(C)
905   $\Rightarrow$ EOS(V)
0.9913 $\Rightarrow$ PO2OS(atm)
2.27624E-18

TKOS(K)
1178 $\Rightarrow$ KpOS
1.22E+08 $\Rightarrow$ PH2O(atm)
0.009211564

deltaGOS(J)
-182366.58

PH2(atm)
0.05

TKEP(K)
1442 $\Rightarrow$ KpEP
1.22E+06 $\Rightarrow$ PO2EP(atm)
2.28327E-14

deltaGEP(J)
-168007.62

Sample	C(ppm)	Edevice(V)	Cr-s(ppm)
	332	0.458	0.208717312
	263	0.4435	0.208802738
	12	0.235	0.273180282

$\Rightarrow$ Ks (this study)
138.1274696

Sieverts's law
deltaGKs[1](J)
-58397.7616 $\Rightarrow$ Ks
130.4553862

BIBLIOGRAGHY

1. K. Kiukkola and C. Wagner, J. Electrochem. Soc., **104**, p.379 (1957)
2. D. Yuan and F.A. Kröger, J. Electrochem. Soc., **116**, p.594 (1969)
3. E.C. Subbarao and H.S. Maiti, in "Advances in Ceramics-Science and Technology of Zirconia, 24B", p.731, ed. S. Somiya, N. Yamamoto and H. Yanagida, the American Ceramic Society, Inc., Columbus, OH(1988)
4. W.A.Fischer and D. Janke, Scripta Metall., 6, p.923 (1972)
5. K.E.Oberg, L.M.Friedman, W.M.Boorstein and R.A.Rapp, Metall. Trans., **4B**, p.75 (1973)
6. K.Kiukkola and C. Wagner, J. Electrochem. Soc., **104**, p. 379 (1957)
7. B.Korousic and B. Marincek, Helv.Chim. Acta, **51**, p. 907 (1968)
8. W.A.Fischer and D. Janke, Scripta Metall., **6**, p. 923 (1972)
9. K.E.Oberg, L.M.Friedman, W.M.Boorstein and R.A.Rapp, Metall. Trans., **4B**, p. 75 (1973)
10. R. R. Odel and R. A. Rapp, Metall. Trans., **8B**, p. 581 (1977)
11. M.Iwase, M.Tanida, A.Mclean and T.Mori, Metall. Trans., **12B**, p. 517 (1981)
12. K.E.Oberg, L.M.Friedman, W.M.Boorstein and R.A.Rapp, Metall. Trans., **4B**, p. 75 (1973)
13. M.Iwase, M.Tanida, A.Mclean and T.Mori, Metall. Trans., **12B**, p. 517 (1981)
14. H.L. Tuller and P.K. Moon, Materials Science and Engineering, **B1**, p. 171 (1988)
15. E.C.Subbarao, in "Advances in Ceramics, vol. 3, Science and Technology of Zirconia," Ed. A.H. Heuer and L.W. Hobbs, p. 1, The American Ceramic Society, Inc., Columbus, OH (1981)
16. O. Ruff and F. Ebert, Z. Anorg. Allg. Chem., **180**[1], p. 19 (1929)
17. G.M. Wolten, J. Am. Ceram. Soc., **46**[9], p. 418 (1963)
18. E.C. Subbarao, H.S.Maiti, and K.K. Sricastava, Phys. Status Solidi A, **21**, p. 9 (1974)
19. V.S. Stubican and J.R.Hellmann, in "Advances in Ceramics, vol. 3, Science and Technology of Zirconia," Ed. A.H. Heuer and L.W. Hobbs, p. 25, The American Ceramic Society, Inc., Columbus, OH (1981)
20. D. K. Smith and S.F. Cline, J. Am. Ceram. Soc., **45**[5], p. 249 (1962)
21. A. H. Heuer, M. Ruhle, in "Advances in Ceramics, vol. 12, Science and Technology of Zirconia II," Ed. A.H. Heuer and L.W. Hobbs, p. 25, The American Ceramic Society, Inc., Columbus, OH (1984)
22. S.F. Pal'guev, V.K. Gill'derman and A.D.Neuimin, J. Electrochem. Soc., **122**, p. 745 (1975)
23. P.H.Scaife, D.A.J.Swinkels, and S.R.Richards, High Temp. Sci., **8**, p. 31(1976)
24. Fouletier, P.Fabry and M.Kleitz, J. Electrochem. Soc., **123**, p. 204 (1976)
25. M.Kleitz, E.Fernandez, J.Fouletier and P.Fabry, in "Advances in Ceramics-Science and Technology of Zirconia, 3", ed. A.H.Heuer and L.W.Hobbs, p.349, the American Ceramic Society, Inc., Columbus, OH(1981)
26. F.K. Moghadam and D.A. Stevenson, J. Am. Ceram. Soc., **65**[4], p. 213 (1982)
27. M. Iwase, E.Ichise, M.Takeuchi and T.Yamasaki, Trans. JIM, **25**[1], p. 43 (1984)
28. W. Weppner, Solid State Ionics, **52**, p. 15 (1992)

29. Advances in Ceramics, vol.3, Science and Technology of Zirconia, ed. A.H. Heuer and L.W. Hobbs, American Ceramic Society, Columbus, OH (1981)

30. J.W. Patterson, E.C. Borgen, and R.A. Rapp, J. Electrochem. Soc., 114, p. 752 (1967)

31. A.W. Smith, F.W. Mwszaros, and C.D. Amata, J. Am. Ceram. Soc., 49[5], p. 240 (1966).

32. J.W. Patterson, E.C. Bogren, and R.A. Rapp, J. Electrochem. Soc., 114, p. 752 (1967)

33. F. Pal'guev, V.K. Gil'derman, and A.D. Neuimin, J. Electrochem. Soc., 122, p. 745 (1975).

34. P.H.Scaife, D.A.J.Swinkels, and S.R.Richards, High Temp. Sci., 8, 31(1976)

35. M.Kleitz, E.Fernandez, J.Fouletier and P.Fabry, in "Advances in Ceramics-Science and Technology of Zirconia, 3", ed. A.H.Heuer and L.W.Hobbs, p.349, the American Ceramic Society, Inc., Columbus, OH(1981)

36. W. Weppner, Solid State Ionics, 52, p.15 (1992)

37. S.P.S. Badwal, Solid State Ionics, 52, p.23 (1992)

38. N.Q. Minh, "Ceramic Fuel Cells," J. Am. Ceram. Soc., 76[3], p. 563 (1993)

39. K. Sano and H. Sakao, J. Inst. Metals, 51, p. 257, (1955)

40. W. Pluschkell and H.J. Engell, Z. Metallk, 56, p. 450(1965)

41. G.R.Belton and E.V.Tankins, Trans. TMS-AIME, 223, p. 1892(1965)

42. T.C.Wilder,Trans. TMS-AIME, 36, p. 1035(1966)

43. W.A.Fischer and W.Ackermann, Arch.Eisenhüttenw., 37, p. 43(1966)

44. J. Gerlach, J.Osterwald and W. Stichei: Z.Metallk., 59, p. 576(1968)

45. M.A.El-Naggar and N.A.D.Parlee, Metall. Trans., 1, p. 2975(1970)

46. K.E.Oberg, L.M.Friedman, W.M.Boorstein and R.A.Rapp, Metall. Trans., 4, p.61(1973)

47. C. Wagner, Thermodynamics of Alloys, p. 51, Addison-Wwsley, Reading, MA (1962)

48. J. Chipman, J. Iron Steel Inst., London, 180, p. 97 (1955)

49. C.H.P. Lupis and J.F. Elliott, Acta Met., 14, p. 529 (1966)

50. C.H.P. Lupis and J.F. Elliott, Acta Met., 14, p. 1019 (1966)

51. C.H.P. Lupis and J.F. Elliott, J. Iron Steel Inst., London, 203, p. 739 (1965)

52. C.H.P. Lupis and J.F. Elliott, Acta Met., 15, p. 265 (1966)

53. C.H.P. Lupis, Liquid Metals, Chemistry and Physics, Ed. S.Beer, p. 1, Marcel Dekker, NY(1972)

54. G.K. Sigworh and J.F. Elliott, Can. Met. Quart., 13[3], p. 455 (1974)

55. R.R. Odel and R.A. Rapp, in "Metal-slag-gas Reactions and Processes", ed. Z.A.Foroulis and W.W. Smeltzer, p.851, the Electrochemical Society, Inc., Princeton, NJ(1975)

56. P.M. Shurygin and V.I. Kryuk, Russian Metallurgy Mining, 3, p.53 (1963)

57. J. Osterwald and J. Schwarzlose, Z. Phys. Chem., 62, p.119 (1968)

58. H. Rickert and A. El Miligy, Z. Metallk., 59, p. 635 (1968)

59. M.M.A. El-Naggar and N.A.S. Parlee, High Temp. Sci., 3, p.138 (1971)

60. K.E.Oberg, L.M.Friedman, W.M.Boorstein and R.A.Rapp, Metall. Trans., 4, p.61(1973)

61. A.O. Isenberg and G.E. Zymboly, "High Performance Cermet Electrodes", U.S. Patent No. 4,582,766. Issued 15 April 1986.

62. A.O. Isenberg, "Methods of Making an Electrode", U.S. Patent No.4,597,170. Issued 1 July 1986.

63. A.O. Isenberg, "Sulfur Tolerant Composite Cermet Electrodes for Solid Oxide Electrochemical Cells", U.S. Patent No.4,702,971. Issued 27 October 1986.

64. R. E. Jensen, "Method of Electrode Fabrication for Solid Oxide Electrochemical Cells", U. S. Patent No. 4,971,830, Issued Nov. 20, (1990).

65. P. H. Middleton, M. E. Seiersten and B. C. H. Steele, in Proceedings of the First International Symposium on Solid Oxide Fuel Cells, (Hollywood, Florida, October 16-18, 1989), Edited by Subhash C. Singhal, The Electrochemical Society, Inc., Princeton, NJ, (1989), p.90.

66. D.W. Dees, and T.D. Claar, T.E. Easler, D.C. Fee and F.C. Mrazek, J. Eletrochem. Soc., 134, p.2141 (1987)

67. T.Kawada, N.Sakai, H.Yokokawa, M.Dokiya, M.Mori and T.Iwata, J. Eletrochem. Soc., 137, p.3042 (1990)

68. P. H. Middleton, M. E. Seiersten and B. C. H. Steele, in Proceedings of the First International Symposium on Solid Oxide Fuel Cells, (Hollywood, Florida, October 16-18, 1989), Edited by Subhash C. Singhal, The Electrochemical Society, Inc., Princeton, NJ, (1989), p.90.

69. P. H. Middleton, M. E. Seiersten and B. C. H. Steele, in Proceedings of the First International Symposium on Solid Oxide Fuel Cells, (Hollywood, Florida, October 16-18, 1989), Edited by Subhash C. Singhal, The Electrochemical Society, Inc., Princeton, NJ, (1989), p.90.

70. D.W. Dees, and T.D. Claar, T.E. Easler, D.C. Fee and F.C. Mrazek, J. Eletrochem. Soc., 134, p.2141 (1987)

71. D.W. Dees, and T.D. Claar, T.E. Easler, D.C. Fee and F.C. Mrazek, J. Eletrochem. Soc., 134, p.2141 (1987)

72. R. E. Jensen, "Method of Electrode Fabrication for Solid Oxide Electrochemical Cells", U. S. Patent No. 4,971,830, Issued Nov. 20, (1990).

73. E.J.L. Schoulerand M. Kleitz, J. Electrochem. Soc., 134, p. 1045 (1987)

74. T. Ogawa, T. Ioroi, Y. Uchimoto, Z. Ogumi, and Z. Takehara, Proceedings of the Third International Symposium on Solid Oxide Fuel Cells, Ed. S.C. Singhal and H. Iwahara, p. 479, The Electrochemical Society, Inc., Princeton, NJ (1993)

75. S. Murakami, Y. Akiyama, N. Ishida, T. Yasuo, T. Saito and N. Furukawa, Proceedings of the Second International Symposium on Solid Oxide Fuel Cells, Ed. F. Grosz, P. Zegers, S.C. Singhal and O. Yamamoto, p. 561, The Electrochemical Society, Inc., Princeton, NJ (1991)

76. W. Fischer, Z. natursfors. 22a, p. 1575 (1967)

77. J. Dupuy, "Thermal Diffusion in Ionic Crystals,", in "Physics of Electrolytes," Ed. J. Hladik, p. 699, Academic Press, NY (1972)

78. M.W. Chase and C.A. davies, JANAF Thermodynamical Tables (1985)

79. M.W. Chase and C.A. davies, JANAF Thermodynamical Tables (1985)

80. K. Sano and H. Sakao, J. Inst. Metals, **51**, p. 257, (1955)

81. W. Pluschkell and H.J. Engell, Z. Metallk, **56**, p. 450(1965)

82. G.R.Belton and E.V.Tankins, Trans. TMS-AIME, **223**, p. 1892(1965)

83. T.C.Wilder,Trans. TMS-AIME, **36**, p. 1035(1966)

84. W.A.Fischer and W.Ackermann, Arch.Eisenhüttenw., **37**, p. 43(1966)

85. J. Gerlach, J.Osterwald and W. Stichei: Z.Metallk., **59**, p. 576(1968)

86. M.A.El-Naggar and N.A.D.Parlee, Metall. Trans., **1**, p. 2975(1970)

87. K.E.Oberg, L.M.Friedman, W.M.Boorstein and R.A.Rapp, Metall. Trans., **4**, p.61(1973)

88. K.E.Oberg, L.M.Friedman, W.M.Boorstein and R.A.Rapp, Metall. Trans., **4**, p.61(1973)

89. N. Ibl and O. Dossenbach, in "Comprehensive Treatise of Electrochemistry - vol. 6," p. 133, Plenum Press, NY (1983)

90. C.H. Herty, Jr., Transactions of AIME, **73**, p. 1107 (1926)

91. C.Wagner, The Physical Chemistry of Steelmaking, Ed. J.F.Elliott, p.237 Technology Press, MIT and John Wiley, NY (1958)

92. J. Mizusaki, H. Tagawa, and T. Saito, J. Elechem. Soc., vol. 141[8], p. 2129 (1994)

93. T. Kenjo, Y. Yamakoshi, and K. Wada, J. Electrochem. Soc., **140**[8], p. 2151 (1993)

94. J. Mizusaki and H. Tagawa, J. Electrochem. Soc., **141**[6], p.1674 (1994)

95. M. Mogensen and T. Lindergaard, in Proceedings of the Third International Symposium on Solid Oxide Fuel Cells, Ed. S.C. Singhal and H. Iwahara, p. 484, The Electrochemical Society, Inc., Princeton, NJ (1993)

96. A.J. Bard and L.R.Faulkner, "Electrochemical Methods - Fundamentals and Applications," John Wiley & Sons, NY (1980)

97. J. Guindet, C. Toux and A. Hammou, Proceedings of the Third International Symposium on Solid Oxide Fuel Cells, Ed. S.C. Singhal and H. Iwahara, p. 484, The Electrochemical Society, Inc., Princeton, NJ (1993)

98. T. Setoguchi, K. Okamoto, K. Eguchi, and H. Arai, J. Electrochem. Soc., **139**[10], 1992

99. K.G. Denbigh, The Thermodynamicss of the Steady state, Methuen & Co. Ltd., London (1951)

100. S.R. De Groot, Thermodynamics of Irreversible processes, North-Holland Publishing Company, Amsterdam (1951)

101. R. Haase, Thermodynamik der irreversiblen Prozesse, D. Steinkipff, Darmstadt (1963)

102. S.Chapman and T.G.Cowling, "The mathematical Theory of Nonuniform Gases," 3rd ed., Cambridge Univ. Press, London (1970)

103. J.O. Hirschfelder, C.F.Curtiss, and R.B.Bird, "Molecular Theory of Gases and Liquids," Wiley, NY (1954)

104. E.T.Turkdogan, "Physical Chemistry of High Temperature Technology," p.201, Academic Press, NY (1980)

105. M.Knuden, Ann. Phys., **28**, p. 75 (1909)

106. E.T.Turkdogan, "Physical Chemistry of High Temperature Technology," p.201, Academic Press, NY (1980)

107. J. E. Bauerle, J. Phys. Chem. Solids, **30**, p. 2657 (1969)

108. D.Y. Wang and A.S. Nowick, J. Electrochem. Soc., **126**, p. 1166 (1979)

109. M.J. Verkerk and A.J. Burggraaf, J. Electrochem. Soc., 130, p. 78 (1983)

110. A.J.A. Winnubst, A.H.A. Scharenborg and A.J. Burggraaf, Solid State Ionics, **14**, p. 319 (1984)

111. T. Kenjo, Y. Horiuchi and S. Osawa, J. Electrochem. Soc., **137**, p. 2423 (1990)

112. N.L. Robertson and J.N. Michaels, J. Electrochem. Soc., **138**, p. 1494 (1991)

113. K.V. Vetter, Electrochemical Kinetics, p. 79, Academics Press, NY (1967)

114. N.J. Maskalick, Proceedings of the First International Symposium on Solid Oxide Fuel Cells, ed. S.C. Singhal, p.279, the Electrochemical Society, Inc., Hollywood, Florida (1993).

115. G. K. Sigworth and J.F. Elliot, Meta. Trans., **4**, p.105 (1973)

116. C. Wagner, Z. Phys. Chem., B, **21**, p.25 (1933)

117. D.L. Douglass and C. Wagner, J. Electrochem. Soc., **116**[7], p. 671 (1969)

118. R.J. Charles, J. Electrochem. Soc., **116**[11], p. 1514 (1969)

119. A.T. Fromhold Jr., J. Phys. Chem. Solids, **33**, p95 (1972)

120. F.A. Kroger, The Chemistry of Imperfect Crystals, vol. 3, "Application of Imperfection Chemistry; Solid State Reactions and Electrochemistry," Elsevier Publishing Company, Inc., NY (1974)

121. T. Takahashi, in "Physics of Electrolytes," vol. 2, ed. J. Hladik, p. 989, Academic Press, NY (1972)

122. D.S. Tannhauser, J. Electrochem. Soc., **125**[8], p.1277(1978).

123. A. V. Virkar, J. Electrochem. Soc., **138**[5], p.1481, (1991)

124. M. Iwase, M. Tanida, A. Mclean and T. Mori, Metall. Trans., **12B**, p. 517 (1981).

125. Z. Hasham, K.C. Chou, and U.B. Pal, J. Electrochem. Soc., **142**[2](1995).

126. W. Jost, Diffusion und chemische Reakitionen in festen Stoffen, p.149, Dresden (1937)

127. T.P. Hoar and L.E. Price, Trans. Faraday Soc., **34**, p. 867 (1938)

128. H. Schmalzried, in "Science and Technology of Zirconia-Advances in Ceramics, I", Ed. A. H. Heuer and L.W. Hobbs, p.254, The American Ceramic Society (1981).

129. D.S. Tannhauser, J. Electrochem. Soc., **125**[8], p.1277(1978).

130. K.G. Denbigh, The Thermodynamics of the Steady State, Methuen & Co. Ltd., London (1951)

131. S.R. De Groot, Thermodynamics of Irreversible processes, North-Holland Publishing Company, Amsterdam (1951)

132. F.A. Kroger, The Chemistry of Imperfect Crystals, vol. 3, "Application of Imperfection Chemistry; Solid State Reactions and Electrochemistry," Elsevier Publishing Company, Inc., NY (1974)

133. W.D. Kingery, H.K. Bowen, and D.R. Uhlmann, "Introduction to Ceramics," p.220, 2nd ed., John Wiley & Sons, NY (1976)

134. K.G. Denbigh, The Thermodynamicss of the Steady state, Methuen & Co. Ltd., London (1951)

135. S.R. De Groot, Thermodynamics of Irreversible processes, North-Holland Publishing Company, Amsterdam (1951)

136. C. Wagner, Z. Phys. Chem., B, **21**, p.25 (1933)

137. H. -I, Yoo and M. Martin, Ceram. Trans., **24**, p. 103 (1991)

138. J. Lee and H. -I. Yoo, J. Electrochem. Soc., **141**[10], p. 2789 (1994)

139. C. Wagner, in Progress in Solid-State Chemistry, vol. 10, part I, p. 3 (1975)

140. C.Wagner, in Proc. 7th Meeting of the International commission of Electrochemical Thermodynamics and Kinetics, p. 361, (butterworths Scientific Publ., London (1957)

141. F.A. Kroger, The Chemistry of Imperfect Crystals, vol. 3, "Application of Imperfection Chemistry; Solid State Reactions and Electrochemistry," Elsevier Publishing Company, Inc., NY (1974)

142. A.W. Smith, F.W. Mwszaros, and C.D. Amata, J. Am. Ceram. Soc., **49**[5], p240 (1966).

143. J.W. Patterson, E.C. Bogren, and R.A. Rapp, J. Electrochem. Soc., **114**, p752 (1967)

144. F. Pal'guev, V.K. Gil'derman, and A.D. Neuimin, J. Electrochem. Soc., **122**, p745 (1975).

145. J. Fouletier, P. Fabry, and M. Kleitz, J. Electrochem. Soc., **123**, p204 (1976)

146. H. Schmalzried, in "Science and Tech-nology of Zirconia - Advances in Ceramics, I", Ed. A. H. Heuer and L.W. Hobbs, p.254, The American Ceramic Society (1981)

147. Z. Hasham, K.C. Chou, and U.B. Pal, J. Electrochem. Soc., **142**[2](1995)

148. A.V.Virkar, J.Electrochem. Soc., **138**[5], p. 1481 (1991)

149. T. Takahashi, in "Physics of Electrolytes," vol. 2, ed. J. Hladik, p. 989, Academic Press, NY (1972)

150. K.E.Oberg, L.M.Friedman, W.M.Boorstein and R.A.Rapp, Metall. Trans., **4**, p.61(1973)

151. K.C.Chou, S.Yuan, U.B.Pal, Proceedings of the Third International Symposium on Solid Oxide Fuel Cells, ed. S.C.Singhal, H.Iwahara, p.431, the Electrochemical Society, Inc., Hawaii, Honolulu(1993)

152. R.R.Odel and R.A.Rapp, in "Metal-slag-gas Reactions and Processes", ed. Z.A.Foroulis and W.W. Smeltzer, p.851, the Electrochemical Society, Inc., Princeton, NJ(1975)

153. E.S. Machlin, Trans. TMS-AIME, **218**, p.314 (1960)

154. J. Szekely and K. Nakanishi, Met. Trans., **6B**, p. 245 (1975)

155. E.D. Tarapore and J.W. Evans, Met. Trans., **7B**, p. 343 (1976)

156. E.D. Tarapore, J.W. Evans, and J. Langfeldt, Met. Trans., **8B**, p 179 (1977)

157. E.D. Tarapore, J.W. Evans, and J. Langfeldt, Met. Trans., **8B**, p 179 (1977)

158. M.Iwase, M.Tanida, A.Mclean and T.Mori, Metall. Trans., **12B**, p. 517 (1981)

159. M. Kleitz, E. Fernandez, J. Fouletier and P. Fabry, in "Advances in Ceramics-Science and Technology of Zirconia, 3", ed. A.H. Heuer and L.W. Hobbs, p.349, the American Ceramic Society, Inc., Columbus, OH(1981).

160. P.H. Scaife, D.A.F. Swinkels, and S.R. Richards, High Temperature Science, **8**, p.31 (1976)

161. D.Britz, Digital Simulation in Electrochemistry, 2nd ed., Springer-Verlag Berlin Heidelberg (1988)

162. D.Britz, Digital Simulation in Electrochemistry, 2nd ed., Springer-Verlag Berlin Heidelberg (1988)

163. D.Britz, Digital Simulation in Electrochemistry, 2nd ed., Springer-Verlag Berlin Heidelberg (1988)

164. D.Britz, Digital Simulation in Electrochemistry, 2nd ed., Springer-Verlag Berlin Heidelberg (1988)

165. M. Fowler, Quart. of Appl. Math., Vol. 3, p. 4 (1945)

166. K.E.Oberg, L.M.Friedman, W.M.Boorstein and R.A.Rapp, Metall. Trans., **4**, p.61(1973)

167. C.F. Gerald, Applied Numerical Analysis, Addison-Wesley, Masse. (1978)

168. M.K. Jain, Numerical Solution of Differential Equations, 2nd ed., Wiley Eastern Ltd. (1984)

169. N. Ibl and O. Dossenbach, in "Comprehensive Treatise of Electrochemistry, 6," ed. E. Yeager, J. O'M. Bockris, B.E. Conway, and S. Sarangapani, p.133, Plenum Press, NY (1983)

170. Reading Tube Corporation, Reading, PA 19612, is currently evaluating the corrosion resistance and thermal shock resistance of the stabilized zirconia provided by Norton Co., MA. It has been demonstrated by Reading Tube Corporation that the stabilized zirconia can survive in the flowing molten copper for more than five hundred hours without observable erosion or corrosion.

171. K.E.Oberg, L.M.Friedman, W.M.Boorstein and R.A.Rapp, Metall. Trans., **4**, p.61(1973)

BIOGRAPHICAL NOTE

The author was born on June 16, 1969 in Changsha, P.R.China. He attended elementary school in that city and graduated from the First High School of Changsha in June 1986.

The author graduated from Zhejiang University in June 1990 with the degree of Bachelor of Science in Materials Science. He worked for two years in Hunan Architectural Materials Center, Changsha, P.R.China. He came to Massachusetts Institute of Technology as a research scientist in July 1992 and enrolled as graduate student in the fall of the same year.

The author is a member of the Society of Sigma Xi, TMS, ASM, ACS and ECS.